



저작자표시-비영리-변경금지 2.0 대한민국

이용자는 아래의 조건을 따르는 경우에 한하여 자유롭게

- 이 저작물을 복제, 배포, 전송, 전시, 공연 및 방송할 수 있습니다.

다음과 같은 조건을 따라야 합니다:



저작자표시. 귀하는 원저작자를 표시하여야 합니다.



비영리. 귀하는 이 저작물을 영리 목적으로 이용할 수 없습니다.



변경금지. 귀하는 이 저작물을 개작, 변형 또는 가공할 수 없습니다.

- 귀하는, 이 저작물의 재이용이나 배포의 경우, 이 저작물에 적용된 이용허락조건을 명확하게 나타내어야 합니다.
- 저작권자로부터 별도의 허가를 받으면 이러한 조건들은 적용되지 않습니다.

저작권법에 따른 이용자의 권리는 위의 내용에 의하여 영향을 받지 않습니다.

이것은 [이용허락규약\(Legal Code\)](#)을 이해하기 쉽게 요약한 것입니다.

[Disclaimer](#)

공학박사 학위논문

Hierarchical Membrane-Electrode Assembly and Metal-Free Cathode Catalysts for Polymer Electrolyte Membrane Fuel Cells

고분자 전해질 연료전지를 위한 다층구조
막-전극 접합체와 비금속 공기극 촉매 연구

2015 년 2 월

서울대학교 대학원

화학생물공학부

김 옥 희

Hierarchical Membrane-Electrode Assembly and Metal-Free Cathode Catalysts for Polymer Electrolyte Membrane Fuel Cells

고분자 전해질 연료전지를 위한 다층구조
막-전극 접합체와 비금속 공기극 촉매 연구

지도교수 성 영 은

이 논문을 공학박사 학위논문으로 제출함
2015년 2월

서울대학교 대학원
화학생물공학부
김 옥 희

김옥희의 공학박사 학위논문을 인준함
2015년 2월

위 원 장 _____ (인)

부위원장 _____ (인)

위 원 _____ (인)

위 원 _____ (인)

위 원 _____ (인)

Abstract

Hierarchical Membrane-Electrode Assembly and Metal-Free Cathode Catalysts for Polymer Electrolyte Membrane Fuel Cells

Ok-Hee Kim

School of Chemical and Biological Engineering

The graduate school

Seoul National University

Fuel cells have come to occupy an important position in power sources of the next generation. They have risen as potential alternatives to alleviate our dependence on fossil fuels because of their high efficiency and low/no pollutant emissions. Among the various kinds of fuel cells, polymer electrolyte membrane fuel cells (PEMFCs) are the most encouraging for commercial applications due to their high efficiency, low operation temperature, and rapid start-up. Also PEMFC have been considered as the

most effective solution of stealthy power sources for underwater vehicles. However, PEMFCs have not been completely commercialized yet; owing to their high cost-components and low durability. In particular, the use of expensive/rare Pt metal as a catalyst becomes a matter of concern. Therefore it would be of great interest to investigate a more effective electrode structure for the higher performance through a careful design of membrane-electrode assembly (MEA), which is the heart of the PEMFC. Also, lots of significant efforts have been devoted to replacing Pt-based catalysts with inexpensive, more abundant nonprecious metal catalysts.

The main theme of this thesis is the realization of high performance MEA in PEMFC: 1) by adopting a new catalyst layer structure, such as a three-dimensional ordered macroporous assembly, and 2) by applying novel metal-free catalyst to both acidic and alkaline polymer membrane electrolyte fuel cell. As mentioned above, a sophisticated design of the electrode in MEA must be needed and this subject in the previous work has not been sufficiently investigated; more detailed study was necessary. Yet most studies for the new catalyst layer design have been confined to the half-cell data and only demonstrated the potential for practical use, however the half-cell is not a practical fuel cell device. Therefore in this thesis new approach for the electrode in MEA has presented and verified a realistic practical use in single-cell, MEA.

Chapter 1 briefly describes the fundamental of fuel cell such as a principle,

history, type and challenge. That includes a brief report about the application of PEMFC to silent power source for underwater platforms, like submarine.

In chapter 2, this section introduces a large-area, hierarchical macroporous Pt electrode for use in practical devices such as MEA in PEMFCs, and this electrode has shown 85% higher performance than that of a conventional catalyst slurry ink based electrode with a similar Pt loading. These three-dimensional ordered macroporous materials could be attractive materials in electrochemical device because of the benefits from the periodic structure. Owing to their open and interconnected pore architecture, these electrodes maintained a good effective porosity, effective catalyst utilization and mass transfer, and satisfactory water management, while the concentration loss was minimized. This chapter provides useful information on development of attractive materials for electrochemical device, not restricted to the fuel cell electrode.

In chapter 3, this part introduces a facile and gram-scale synthesis of graphitic carbon nitride hybrid as a metal-free hybrid catalyst for both acidic (proton as conducting reactants) and alkaline (hydroxide ion as conducting reactants) fuel cells, and this metal-free cathode electrode has exhibited an outstanding performance, i.e., 69% and 80% of commercial Pt/C performance in actual fuel cell devices using MEA with acidic and alkaline polymer electrolytes, respectively. Although numerous reports have been published on nonprecious metal catalysts for the oxygen reduction reaction of fuel cell

cathode, few studies have demonstrated a realistic practical use of these catalysts in fuel cells, and furthermore, the reported performances are inferior to the performance obtained in this chapter. The fabrication method and remarkable performance of the single cell in this chapter are progresses toward realistic applications of metal-free materials in commercialized fuel cells.

Keywords: Polymer electrolyte membrane fuel cell (PEMFC) · membrane electrode assembly (MEA) · hierarchical structure · metal-free catalyst

Student Number: 2011-30793

Contents

| | |
|---|-------------|
| Abstract | i |
| Contents..... | v |
| List of Tables | viii |
| List of Figures | ix |
| | |
| Chapter 1. General Introduction | 1 |
| 1.1 Fundamental of Fuel Cells | 1 |
| 1.1.1 Principle..... | 1 |
| 1.1.2 History | 3 |
| 1.1.3 Types of Fuel Cells | 5 |
| 1.2.4 Challenges of PEMFC | 8 |
| 1.2 Polymer Electrolyte Membrane Fuel Cells..... | 11 |
| 1.2.1 Cell Components | 21 |
| 1.2.2 Electrode Reactions | 16 |
| 1.2.3 Challenges of PEMFC | 18 |
| 1.3 PEMFC as silent power source for underwater platforms | 21 |
| 1.3.1 Fuel cell as air-independent propulsion (AIP) power system ... | 21 |
| 1.3.2 Realization of PEMFC technology to submarines | 24 |

| | | |
|--|----------------------------|-----------|
| 1.4 | References..... | 31 |
| | | |
| Chapter 2. Ordered Macroporous Pt Electrode and Enhanced Mass Transfer in Fuel Cells Using Inverse Opal Structure | | |
| | | 40 |
| 2.1 | Abstract..... | 40 |
| 2.2 | Introduction..... | 42 |
| 2.3 | Experimental Section..... | 48 |
| 2.4 | Result and Discussion..... | 54 |
| 2.5 | Conclusions..... | 85 |
| 2.6 | References..... | 86 |
| | | |
| Chapter 3. Realistic Applications of Metal-Free Hybrid Materials as Fuel Cells Electrodes: both Acidic and Alkaline Polymer Electrolytes..... | | |
| | | 95 |
| 3.1 | Abstract..... | 95 |
| 3.2 | Introduction..... | 97 |
| 3.3 | Experimental Section..... | 101 |
| 3.4 | Result and Discussion..... | 110 |
| 3.5 | Conclusions..... | 137 |
| 3.6 | References..... | 138 |

| | |
|----------------------------------|------------|
| Korean Abstract | 144 |
| List of Publications..... | 148 |

List of Tables

Chapter 1

| | |
|---|---|
| Table 1.1 Fuel cell types and feature. | 6 |
|---|---|

Chapter 2

| | |
|--|----|
| Table 2.1 Pt oxidation states from electrode surface XPS peak analysis .. | 67 |
| Table 2.2 Structures and electrochemical properties of IO electrodes | 81 |

Chapter 3

| | |
|--|-----|
| Table 3.1 Nitrogen properties, binding energy, atomic ratio and N content of g-CN materials. | 130 |
| Table 3.2 Performance characteristics of g-CN-CNF-700-based PEMFCs and AEMFCs..... | 136 |

List of Figures

Chapter 1

| | |
|---|----|
| Figure 1.1 Fuel cell history time line..... | 4 |
| Figure 1.2 Various applications of fuel cell..... | 7 |
| Figure 1.3 Schematic of PEMFC..... | 9 |
| Figure 1.4 The components and structure of PEMFC single cell MEA.... | 12 |
| Figure 1.5 Transport of gases, protons, and electrons in a PEMFC MEA. | 15 |
| Figure 1.6 Type 212 submarine with fuel cell propulsion..... | 28 |
| Figure 1.7 Reactant storage for submarines | 29 |

Chapter 2

| | |
|---|----|
| Figure 2.1 Conceptual diagrams of two MEAs. | 45 |
| Figure 2.2 Schematic diagram of the fabrication process. | 55 |
| Figure 2.3 AFM and corresponding FE-SEM images of a PS crystal template on GDLs..... | 56 |
| Figure 2.4 FE-SEM images images of various electrodes..... | 59 |
| Figure 2.5 FE-SEM images of IO electrode..... | 61 |
| Figure 2.6 XRD patterns of electrodes. | 64 |
| Figure 2.7 XPS spectra of Pt 4f. | 65 |
| Figure 2.8 The ratio of Pt Pt oxidation properties of electrodes..... | 66 |

| | |
|---|----|
| Figure 2.9 Photograph of practical PEMFC single cell..... | 69 |
| Figure 2.10 Polarization curves of IO electrode-based MEAs..... | 71 |
| Figure 2.11 Polarization curves under oxygen | 72 |
| Figure 2.12 Cyclic voltammograms of electrodes..... | 76 |

Chapter 3

| | |
|---|-----|
| Figure 3.1 Conceptual diagrams of the g-CN-CNF-based MEA and the single cell..... | 100 |
| Figure 3.2 Condensation reactions of melamine and cyanuric chloride to produce extended networks of g-CN..... | 104 |
| Figure 3.3 Structure and image of g-CN and g-CN-CNF. | 111 |
| Figure 3.4 FE-SEM images of g-CN-CNF and commercial Pt/C-based MEA in PEMFCs..... | 113 |
| Figure 3.5 FE-SEM images of g-CN-CNF and commercial Pt/C-based MEA in AEMFCs. | 114 |
| Figure 3.6 Physical characterization of g-CN. | 116 |
| Figure 3.7 FT-IR spectrum and XRD pattern of g-CN materials | 118 |
| Figure 3.8 TGA weight loss curve of g-CN and g-CN-CNF..... | 119 |
| Figure 3.9 Cyclic voltammetry of g-CN materials..... | 121 |
| Figure 3.10 Electrochemical characterization of g-CN-CNF..... | 122 |
| Figure 3.11 Koutecky–Levich plots of g-CN-CNF-700..... | 124 |
| Figure 3.12 Long-term stability test of g-CN-CNF-700..... | 127 |

| | |
|---|-----|
| Figure 3.13 XPS spectra of N 1s of g-CN-CNF materials | 129 |
| Figure 3.14 Polarization curves of g-CN-CNF-700-based MEAs | 133 |
| Figure 3.15 <i>In-situ</i> EIS of g-CN-CNF-700 and commercial Pt/C-based MEAs..... | 135 |

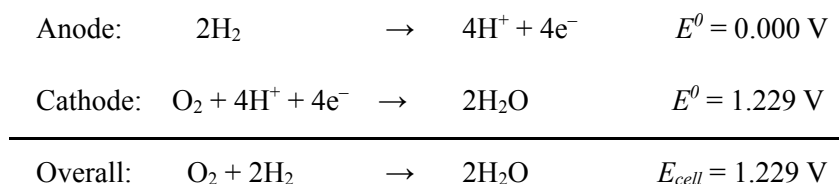
Chapter 1

General Introduction

1.1 Fundamental of Fuel Cells

1.1.1 Principle

Due to the rising concerns on the exhaustion of petroleum based energy resources and climate change; fuel cell technologies have received much attention in recent years owing to their high efficiencies and low/non emissions. Fuel cells are electrochemical devices that directly convert chemical energy stored in fuels such as hydrogen to electrical energy. Its efficiency can reach as high as 60% in electrical energy conversion and overall 80% in co-generation of electrical and thermal energies with >90% reduction in major pollutants.¹ Hydrogen gas is the most common fuel for fuel cell although hydrocarbons such as methanol, ethanol and natural gas are usable. In the case of hydrogen fuel cell, the reactions those occur in fuel cell are as the followings:



E^0 is standard electrode potential vs. normal hydrogen electrode (NHE). E^0 can be obtained thermodynamically from difference of Gibbs free energy. As a result, theoretical cell voltage of hydrogen fuel cell is 1.229 V. However in

actual hydrogen fuel cell, the cell voltage is lower (~ 1.0 V) than theoretical value, because of sluggish cathode reaction kinetics and fuel crossover from anode to cathode. Moreover cell voltage is decreased when current is increased to generate high power, and energy conversion efficiency is also decreased. Nevertheless, silent characteristics due to lack of moving parts and low/non emission of harmful byproducts make fuel cell an attractive device.

However, at the same time, fuel cells have some limitations such as high cost, low durability, and low infra for hydrogen economy. Fuel availability and storage are also problems. Although fuel cells work best when hydrogen is used as a fuel, owing to the low volumetric energy density and a storage difficulty of hydrogen, alternative liquid fuels (e. g. methanol, ethanol, formic acid, and gasoline) are tried to use directly or with reformer.²

1.1.2 History

Humphry Davy proved the concept of a fuel cell with the structure of $C/H_2O/HNO_3/O_2/C$ in 1801.³ And Christian Friedrich Schonbein discovered the principle of the fuel cell in 1839.⁴ A Welsh judge and physical scientist, Sir William Robert Grove, conducted a series of experiments that electric current could be produced by the electrochemical reaction of hydrogen and oxygen on a Pt electrode, and named such cell as “gas voltaic battery” in

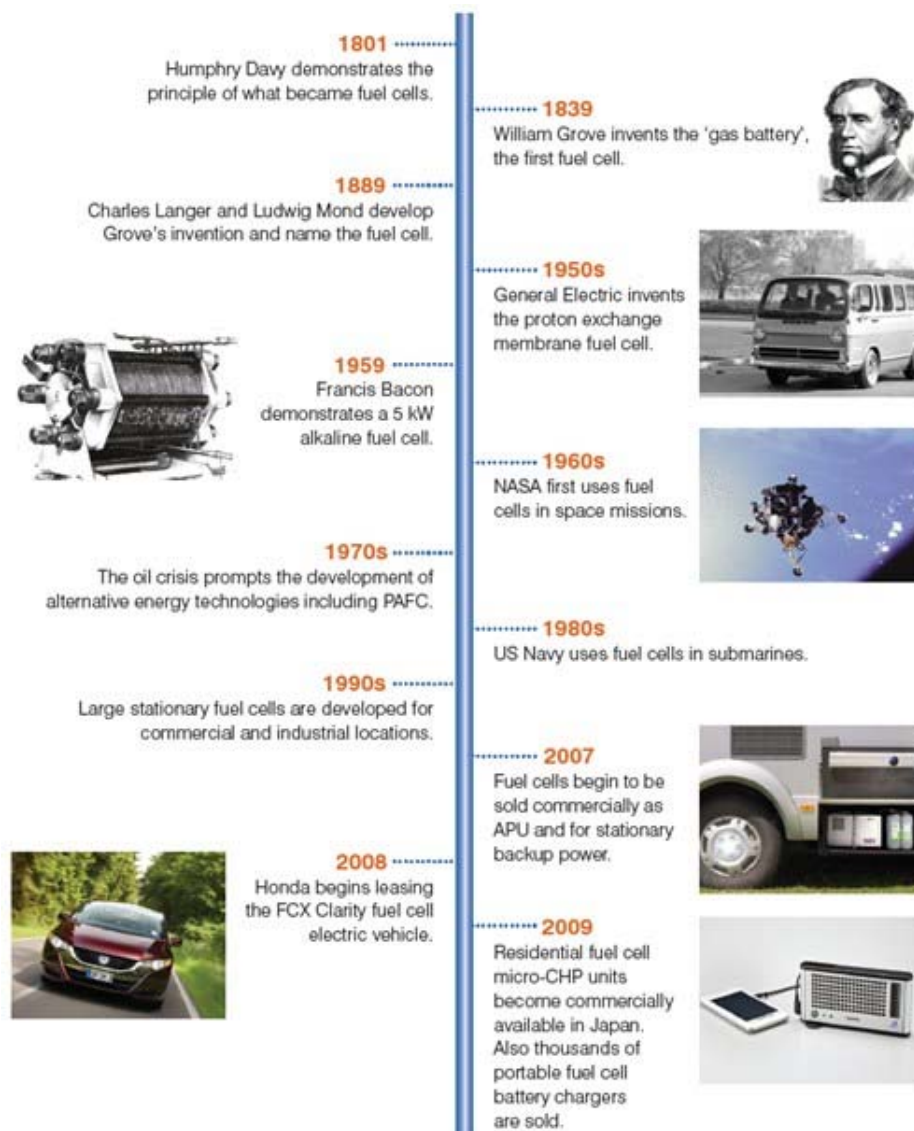


Figure 1.1 Fuel cell history timeline.³

1839.⁵ The term ‘fuel cell’ was first used by Ludwig Mond and Charles Langer in 1889. Francis Bacon developed the first successful application of alkaline fuel cell (AFC) in 1932, and demonstrated it in 1959 with 5 kW-fuel cell system for powering welding machinery. Willard Thomas Grubb and Leonard Niedrach at General Electric invented the first polymer electrolyte membrane fuel cell (PEMFC), and they cooperated with NASA. This PEMFC was used as a power source of the Gemini space program in 1960s, and Gemini VII.⁶ In the Apollo space program, AFCs were used as an electric power source when the astronauts landed on the moon. Nowadays, numerous efforts are conducting to enable the widespread commercialization of fuel cells in diverse sectors.⁷ Fuel cell history timeline is shown in Fig. 1.1.³

1.1.3 Types of Fuel Cells

There are many kinds of fuel cells, and generally their names are related electrolyte or fuel of them. Usually five categories of fuel cells have received major efforts of research and these fuel cell types are listed in Table 1.1. Working temperatures are determined by the electrolyte temperature for carrying the ion effectively. Applications of these fuel cells are related to the working temperature and fuel types.

Table 1.1 Fuel cell types and features

| Fuel Cell Type | Common Electrolyte | Operating Temperature | Typical Stack Size | Efficiency | Applications | Advantages | Disadvantages |
|------------------------------------|--|---|-------------------------|--|--|--|--|
| Polymer Electrolyte Membrane (PEM) | Perfluoro sulfonic acid | 50-100°C 122-212°F typically 80°C | < 1kW– 100kW | 60% transportation 35% stationary | <ul style="list-style-type: none"> • Backup power • Portable power • Distributed generation • Transportation • Specialty vehicles | <ul style="list-style-type: none"> • Solid electrolyte reduces corrosion & electrolyte management problems • Low temperature • Quick start-up | <ul style="list-style-type: none"> • Expensive catalysts • Sensitive to fuel impurities • Low temperature waste heat |
| Alkaline (AFC) | Aqueous solution of potassium hydroxide soaked in a matrix | 90-100°C 194-212°F | 10–100 kW | 60% | <ul style="list-style-type: none"> • Military • Space | <ul style="list-style-type: none"> • Cathode reaction faster in alkaline electrolyte, leads to high performance • Low cost components | <ul style="list-style-type: none"> • Sensitive to CO₂ in fuel and air • Electrolyte management |
| Phosphoric Acid (PAFC) | Phosphoric acid soaked in a matrix | 150-200°C 302-392°F | 400 kW 100 kW module | 40% | <ul style="list-style-type: none"> • Distributed generation | <ul style="list-style-type: none"> • Higher temperature enables CHP • Increased tolerance to fuel impurities | <ul style="list-style-type: none"> • Pt catalyst • Long start up time • Low current and power |
| Molten Carbonate (MCFC) | Solution of lithium, sodium, and/or potassium carbonates, soaked in a matrix | 600-700°C 1112-1292°F | 300 kW 3 MW module | 45–50% | <ul style="list-style-type: none"> • Electric utility • Distributed generation | <ul style="list-style-type: none"> • High efficiency • Fuel flexibility • Can use a variety of catalysts • Suitable for CHP | <ul style="list-style-type: none"> • High temperature corrosion and breakdown of cell components • Long start up time • Low power density |
| Solid Oxide (SOFC) | Yttria stabilized zirconia | 700-1000°C 1202-1832°F | 1 kW–2 MW | 60% | <ul style="list-style-type: none"> • Auxiliary power • Electric utility • Distributed generation | <ul style="list-style-type: none"> • High efficiency • Fuel flexibility • Can use a variety of catalysts • Solid electrolyte • Suitable for CHP & CHHP • Hybrid/GT cycle | <ul style="list-style-type: none"> • High temperature corrosion and breakdown of cell components • High temperature operation requires long start up time and limits |

[Source: US DOE's document (<http://www.hydrogenandfuelcells.energy.gov>)]⁷



Figure 1.2 Various applications of fuel cell.

Low temperature fuel cell such as PEMFC, DMFC (direct methanol fuel cell), and PAFC (phosphoric acid fuel cell) is suitable for portable or vehicular applications, and high temperature fuel cell such as SOFC (solid oxide fuel cell) and MCFC (molten carbonate fuel cell) is usable for distributed generation. Fig. 1.2 shows the various application fields for fuel cell.

1.2 Polymer Electrolyte Membrane Fuel Cells

PEMFCs employ a solid electrolyte which is based on a polymer backbone with side-chains possessing acid-based groups.⁸ Illustration of general PEMFC structure and operation is shown in Fig. 1.3.

There are two expressions of PEMFC such as polymer electrolyte membrane fuel cell or proton exchange membrane fuel cell, and some other people say PEFC (polymer electrolyte fuel cell). Because the electrolyte of DMFC is also polymer, some people categorize DMFC as a kind of PEMFC using methanol fuel. However in general PEMFC is regarded hydrogen fuel cell.

Considerable improvements of PEMFC technology were made from the early 1970s related with the adoption of the fully fluorinated Nafion[®] membrane of DuPont. However, research and development in PEMFCs did not receive much attention and funding from the federal government; until a

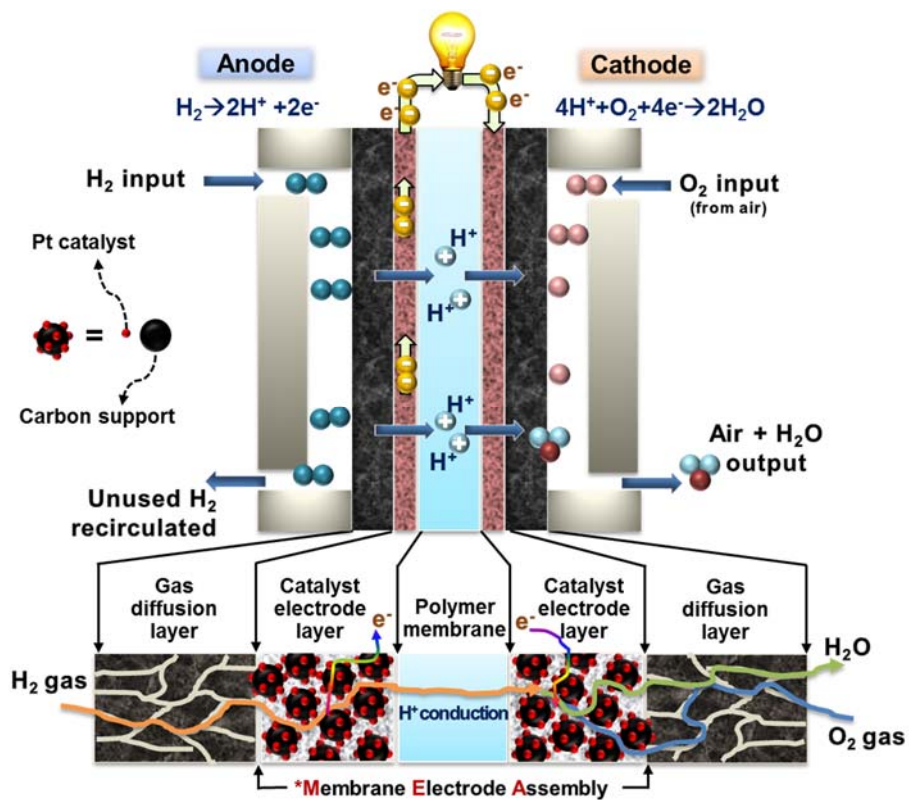


Figure 1.3 Illustration of PEMFC operations.

couple of decades ago when breakthrough methods for reducing the amount of platinum required for PEMFCs were developed by Los Alamos National Laboratory (LANL) and others. Notably, Dr. Raistrick of LANL came up with a catalyst-ink technique for fabricating the electrodes.⁹ This breakthrough method made it possible to increase the utilization of catalyst and at the same time to reduce the amount of precious platinum metal needed. Thereafter many technical and associated fundamental breakthroughs have been achieved during the last couple of decades, but many challenges still remain to be done such as a reducing cost and improving durability for the completely commercialization of PEMFCs.

Recently the PEMFC is vigorously investigated by automobile companies such as GM, Toyota, Nissan, and Hyundai-Kia motor company because PEMFC is the alternative power source of gasoline engine for vehicle.¹⁰⁻¹³ PEMFC has many advantages for use in vehicles; they operate at relatively low temperature, and have short start-up and transient-response times compared to other types of fuel cells.¹⁴ Moreover national research institutes such as Los Alamos, Argon, and Lawrence Berkeley National Laboratory, and chemical companies developing polymer membrane such as Gore and 3M are also trying to improve the PEMFC technology.¹⁵⁻²¹ Also US DOE invests to the PEMFC research groups for realization of fuel cells technology.⁷

1.2.1 Cell Components

A typical PEMFC unit single cell consists of the following components: solid state polymer electrolyte membrane (PEM), electrocatalyst in catalyst layer (electrode), gas diffusion layer (GDL), flow channels (in bipolar plate) and current collector. The components and structure of PEMFC single cell is shown in Fig. 1.3 and 1.4.

The **PEM** is located between anode and cathode catalyst layer. This solid polymer electrolyte transports the protons from anode to cathode, and supports the anode and cathode catalyst layers. It also separates the oxidizing and reducing environments on the cathode and anode reaction zone. Therefore, the PEM is required high proton conductivity, low gas permeability, mechanical, thermal and chemical stability, and so on.^{10,11} The most commonly used PEMs are perfluorosulfonic acid membrane such as Nafion (Dupont), Gore-Select (Gore), and Aciplex and Flemion (Asahi). Each of the anode and cathode **catalyst layer** are deposited to the both sides of the PEM, and this three-layer component is also called as catalyst-coated membrane (CCM).

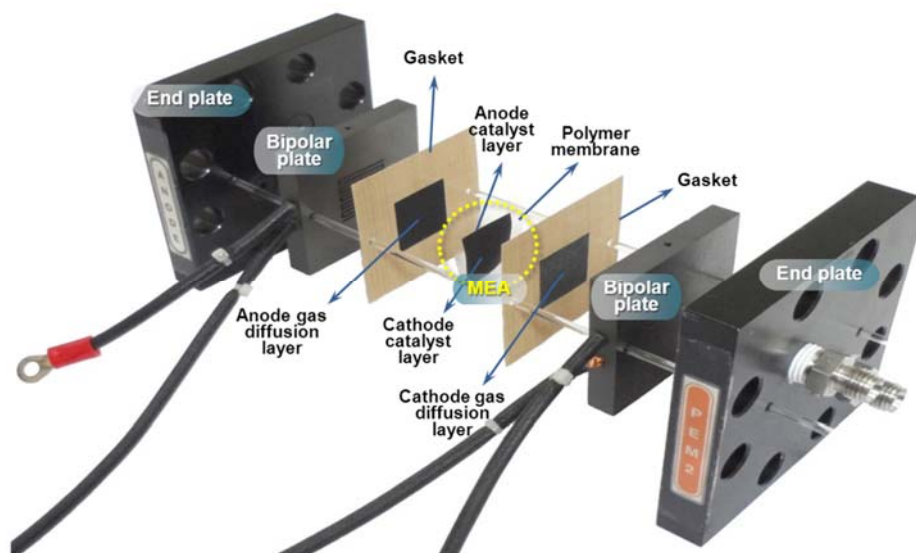


Figure 1.4 The components and structure of PEMFC single cell MEA.

Some people regard electrode in PEMFC as the span from the surface of the membrane to gas channel and current collector. However, as shown in Fig. 1.3 and 1.4, the electrode is considered herein as the components that catalyst layer. The catalyst layers are middle of the membrane and the backing layers. Nano-sized carbon supported Pt particles (~3 nm) are widely used as electrocatalysts in PEMFCs. Also, the carbon support plays an important role in electrocatalyst. It provides the catalyst dispersion and has effect on increasing of catalyst utilization. Since using carbon support, the loading amounts of Pt are greatly reduced in PEMFC. The carbon materials have effect on the properties of supported metal catalysts, such as metal particle size, morphology, size distribution, dispersion and stability. Carbon blacks such as Vulcan XC72 (Cabot), Black Pearls 2000 (Cabot), and Ketjen EC300J (Ketjen Black) are generally used as supports for catalysts.

An effective electrode must keep a balance correctly for required transport processes in operational fuel cell, as shown in Fig. 1.5. The three main transport processes are following as:

- i. Protons from the membrane to the catalyst
- ii. Electrons from the current collector to the catalyst through the gas diffusion layer
- iii. The reactant and product gases to and from the catalyst layer

and the gas channels.¹⁶

Protons, electrons, and gases are often referred to as the three phases found in a catalyst layer. Part of the optimization of an electrode design is the attempt to correctly distribute the amount of volume in the catalyst layer between the transport media for each of the three phases to reduce transport losses. In addition, it is critical point that the catalyst particles take an intimate intersection of these transport processes for effective operation of a PEMFC.

Two *gas diffusion layers* (GDLs) are located outside of anode and cathode catalyst layers. It provides the mechanical support for catalyst layer, an electrical pathway for electrons, and a flow channel for product water and reactant gas. Therefore, the GDL is required mechanical stability, flexibility, and high conductivity. Typically, water proofed carbon paper or carbon cloth is used as the GDL. The GDL is prepared with hydrophobic material such as polytetrafluoroethylene (PTFE) in porous structure to improve the gas diffusion and water management.⁸

PEM and attached two electrode (anode and cathode catalyst layer) is called as *membrane-electrode assembly* (MEA) (Fig. 1.3 and 1.4), these components are fabricated individually and then pressed to together at high temperatures and pressures. MEA is the core component where the

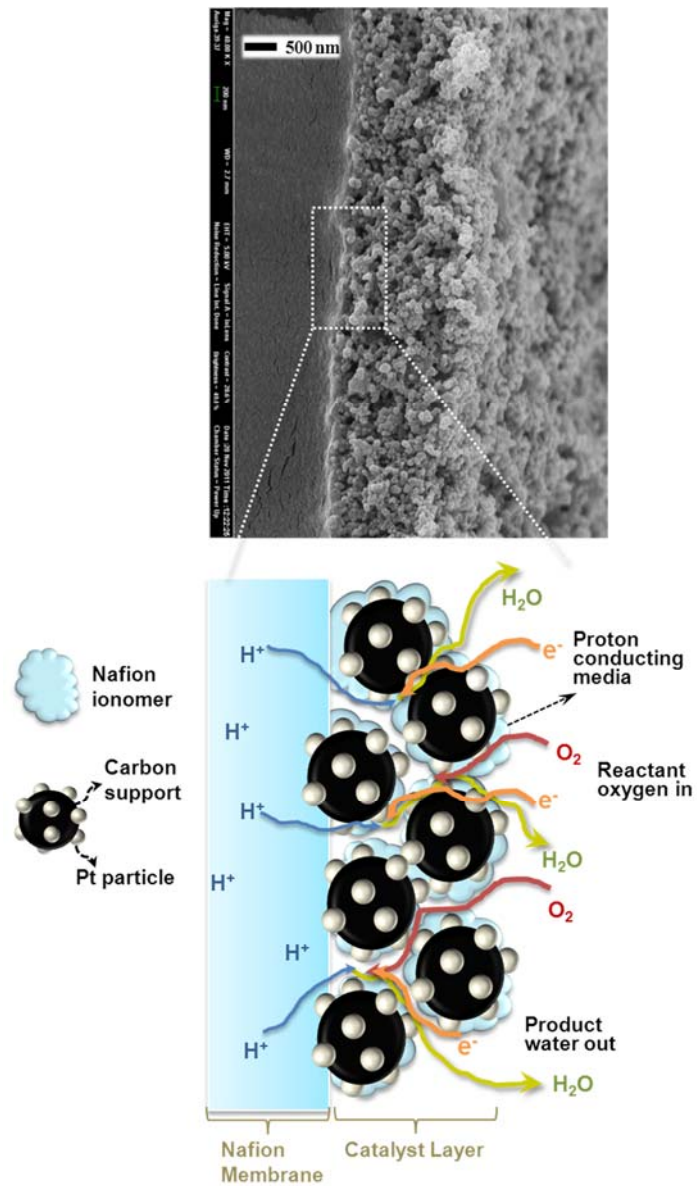


Figure 1.5 Transport of gases, protons, and electrons in a PEMFC MEA.

electrochemical reactions and energy conversion are really occurred. Thus it is called as the heart of the PEMFC.

MEA preparation method usually means catalyst layer deposition method. There are various deposition techniques of catalyst layer such as spraying, painting (brushing), doctor blade (bar coating), electrospraying, screen printing, inkjet printing.²²⁻³³ All of these fabrication methods are possible when the catalysts dispersed in solvent. By those methods, catalyst layer can be deposited on PEM or gas diffusion layers because catalyst layer is located between PEM and gas diffusion layers. Therefore MEA preparation method can be classified as CCM, and catalyst-coated substrate (CCS) method.³³⁻³⁷ Among the various MEA preparation methods, decal transfer method is an exceptional way, because the catalyst layer is not deposited on PEM or GDL but deposited on other substrate such as Teflon blank, Kapton film, and filter paper. Decal transfer method is classified as CCM method because catalyst layer on substrate is transferred to PEM by hot-pressing.³⁸⁻⁴²

1.2.2 Electrode Reactions

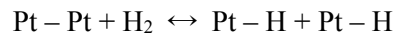
The anode reaction in a PEMFC is hydrogen oxidation reaction (HOR) at the surface of the anode electrocatalyst.⁴³ The mechanism of anode reaction is described by following three steps: Tafel step (recombination reaction),

Volmer step (charge transfer reaction), and Heyrovsky step (ion plus atom reaction). The overall reaction can be expressed as:



The overall process can be consisted of five steps as following:

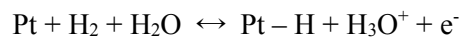
- i. The transport of the H_2 molecules to the Pt electrode through gas diffusion
- ii. The adsorption of hydrogen molecules to the anode electrocatalyst through gas diffusion
- iii. The dissociative adsorption of hydrogen on the surface of electrocatalyst through the Tafel reaction



- iv. The ionization of H atom giving one electron to the electrode and a hydronium ion to the solution, leaving an empty Pt site through the Volmer reaction

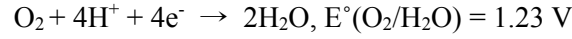


or direct reaction of hydrogen molecules through Heyrovsky reaction



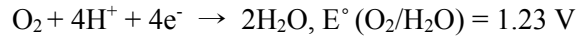
- v. The transport of the hydronium ions from the phase boundary to the electrolyte solution phase

The cathode reaction in a PEMFC is oxygen reduction reaction (ORR) at the surface of cathode electrocatalyst. The overall four electron of oxygen in acid electrolyte expressed as:

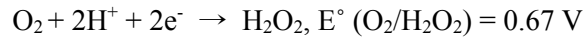


However, the ORR is a multi-step reaction that can be consisted of several elementary steps.⁴⁴ In acidic media, ORR can be described as follows:

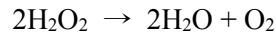
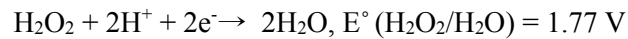
- i. The direct four electron pathway



- ii. The peroxide pathway



followed by further reduction or a chemical decomposition via



Many studies have been developed to describe the ORR with several different models. Bagotskii et al. prospered a general scheme for the reactions of O_2 and H_2O_2 .^{45,46} The pathway of ORR depends on the pH of the electrolyte and the catalyst. Usually, both the direct and peroxide pathway is found on platinum, platinum alloys, palladium, and silver.

1.2.3 Challenges of PEMFC

PEMFCs are attractive power generators for vehicles, electronic devices, and stationary power generators on account of their low operating temperature and high efficiency of energy conversion. On the other hand, the commercialization of PEMFCs requires an increase in the lifespan of the MEA on the PEMFC as well as a decrease in manufacturing cost. The cost of novel metals, especially platinum is one of the most important barriers to the commercialization of PEMFC.⁴⁷

For PEMFC cost reduction, the search for inexpensive, high performance electrocatalysts for PEMFC has taken two different approaches. The first approach is to reduce catalyst usage through increasing Pt utilization in the catalyst layers. This can be achieved by alloying Pt with inexpensive metals (Co, Fe, etc.), and/or by utilizing unique support materials for Pt nanoparticle deposition. In the last two decades, the required Pt loading has been reduced significantly to approximately 0.2 mg cm^{-1} . Unfortunately, the increasing Pt price during this time has totally offset the Pt loading reduction, rendering the efforts made towards Pt loading reduction in the last two decades ineffective. Therefore, it seems that this approach may not be the long-term solution for cost reduction of PEM fuel cells. The other approach is to develop non-precious metal-based electrocatalyst materials. This approach has been stimulated extensively by the recent push for PEMFC

commercialization. Thus, development of high performance, non-precious metal-based catalyst materials seems to be the solution for a long-term and sustainable commercialization of PEMFCs. Unfortunately, until today, the performance of the best non-precious metal catalysts (generally carbon supported Fe- and/or Co-N catalysts) is still inferior when compared to Pt-based catalysts in terms of both activity and stability. However, the incremental improvement in both activity and stability of non-precious metal catalysts towards their practical usage has been seen in recent years, making this approach more active and promising.⁴⁸⁻⁵⁰

In addition, innovation of the preparation procedure for MEAs has come to occupy an important position as well, because the key factor in fuel cell performance (power density) and durability is the structure of the electrode in the MEA. Building electrode architectures with suitable three-phase boundaries composed of ionic and electronic conduction and mass transfer is necessary to produce a high performance MEA. Hence, optimization and modification of electrode structure has proven to be critical for improving the performance and durability of PEMFCs.^{51,52} Accordingly, several attempts have been made to enhance mass transfer and improve water management through careful design of the electrode structure, for example, the use of an additional solvent to control the polarity,⁵³ application of a

pore-forming agent,⁵⁴ and optimization of the ionomer content.⁵¹ Furthermore, three-dimensional (3D) nanostructured materials have been introduced for catalyst supports including carbon nanotubes (CNTs), carbon nanofibers, layer-by-layer assemblies, and inverse opal structures.⁵⁵⁻⁵⁸

1.3 PEMFC as silent power source for underwater platforms

Constant attention has been paid to the stealthy underwater platforms such as swimmer delivery vehicles, unmanned underwater vehicles, submarines, weapons and mobile countermeasures. Therefore, there is a desire to reduce noise levels and decrease detectable emissions of all types. At the same time, the concept of fully electric derived vehicle and weaponry for naval platforms regarded as potential stealthier platforms and pulse-power, lower signature weapons. Storing and generating electric power is therefore of major interest, both for propulsion over long distances and also for pulse-power weapons. This section focus on fuel cells as a means of meeting stealth and performance targets for different underwater platforms.

1.3.1 Fuel cell as air-independent propulsion (AIP) power system

To avoid detection, a submarine should remain submerged, ideally using

stealthy power sources. For a conventional, non-nuclear submarine, AIP improves submerged endurance, removes any requirement for intake and exhaust connections through the surface, and immediately reduces the chances of detection by visual, radar or even thermal methods.

The ideal AIP power source for a submarine must be quiet, have a low thermal signature, doesn't need to discharge any detectable contaminants, and be capable of operating without atmosphere. In principle, there is no reason why hybrid, air-independent power could not be used for all sizes of platform. And the AIP system is likely to be a hybrid combination of power generators and energy storage devices, ideally by replacing the diesel generators in submarines with fuel cells. The energy storage device will supply start-up power of the power generator, peak/pulse power for weapon and continuous power for a minimum specified duration. The power generator should supply base-load power, and be recharged in the energy storage device. Also a hybrid AIP configuration might be feasible for smaller and compact unmanned underwater platforms, and it depends on the required submerged endurance.⁵⁹

The requirements to be fulfilled by an AIP system on board submarines are following:

- i. Operation without surface contact over longer periods
- ii. Low noise level

- iii. Low magnetic signatures
- iv. Low heat transfer to the sea water

Various systems were investigated, such as closed cycle diesel engines, closed cycle steam turbines, stirling cycle engines and fuel cells. In the 1970s based on a tradeoff study the German submarine industry and the German Ministry of Defense (MoD) decided that the fuel cell offered the most effective solution for practical application on submarines to fulfil the mentioned requirements.⁶⁰

Among the various fuel cell types, the PEMFC was chosen, which operate at temperatures of $\sim 80^{\circ}\text{C}$, for practical application of fuel cell technology in submarines. The advantages of this technology are clear: low operating temperature (= low signature), highly efficient energy conversion using hydrogen and oxygen, favorable switch-on/switch-off, dynamic behavior, no exhausts and no limits in power or diving depth. The reasons and benefits for PEMFC are obvious in view of following points:

- i. Favorable low signature: no noise, no exhausts, minimum waste heat transfer to ambient seawater and closed loop fuel cell/metal hydride cylinders
- ii. No power limits, no diving depth restrictions
- iii. Modular design of the entire propulsion system

- iv. High efficiency, especially at partial load
- v. Low maintenance requirements
- vi. No extra complement and ease automation

One of the major advantages of the fuel cell over the conventional battery is the power capability. Power capability of the fuel cell stack can be varied independently with the energy density. When a high energy storage density is required, it is possible that control the fuel and oxidant of sub-systems which dominate the overall size of fuel cell plant. The most energy-dense fuel in gravimetric terms is hydrogen, which has a theoretical energy storage density of 33 kWh kg⁻¹, (*c.f.* diesel 13.2 kWh kg⁻¹, methanol 6.2 kWh kg⁻¹). However, the volumetric energy density of hydrogen is low. Thus one of the greatest challenges is to package hydrogen effectively, particularly for minimum volume for submarine vehicles.⁶¹

1.3.2 Realization of PEMFC technology to submarines

For the first fuel cell powered submarine U1, the propulsion system was based on alkaline fuel cell technology, because of the availability of that technology at the time. However, parallel to this test phase, PEMFC technology was developed well and adapted to the specific requirements in submarines such as signatures, interfacing standards or use with pure oxygen.

The Siemens PEMFCs reflect a metal-based technology combining favorable mechanical properties, e.g. shock resistance, high integration of the processes resulting in low volume and high reliability at high power density. A PEMFC module with a power output in the range of 30–40 kW was developed by Siemens for application in the Class 212A submarines (Figure 1.6) for the German and Italian Navies. These fuel cell modules consist of a stack comprising several single cells, an integrated humidifier for hydrogen and oxygen and all the peripheral process equipment like valves, sensors, connection parts for the media like cooling water, hydrogen, oxygen, which are necessary for the operation of the fuel cell module. The fuel cell module is connected to the module electronics as part of the fuel cell control board, which controls and monitors the processes within the fuel cell module. Additionally for application in the submarine the fuel cell module is encapsulated in a container filled with nitrogen as part of the integral safety philosophy of the system.

After successful finalization of the 30–40 kW fuel cell modules, the development and investigation of Siemens have been continued. The power density increased by a factor of two, and a more compact arrangement of the peripheral process equipment resulted in a 120 kW module – a fuel cell module with the fourfold of power output at nearly the same dimensions as its

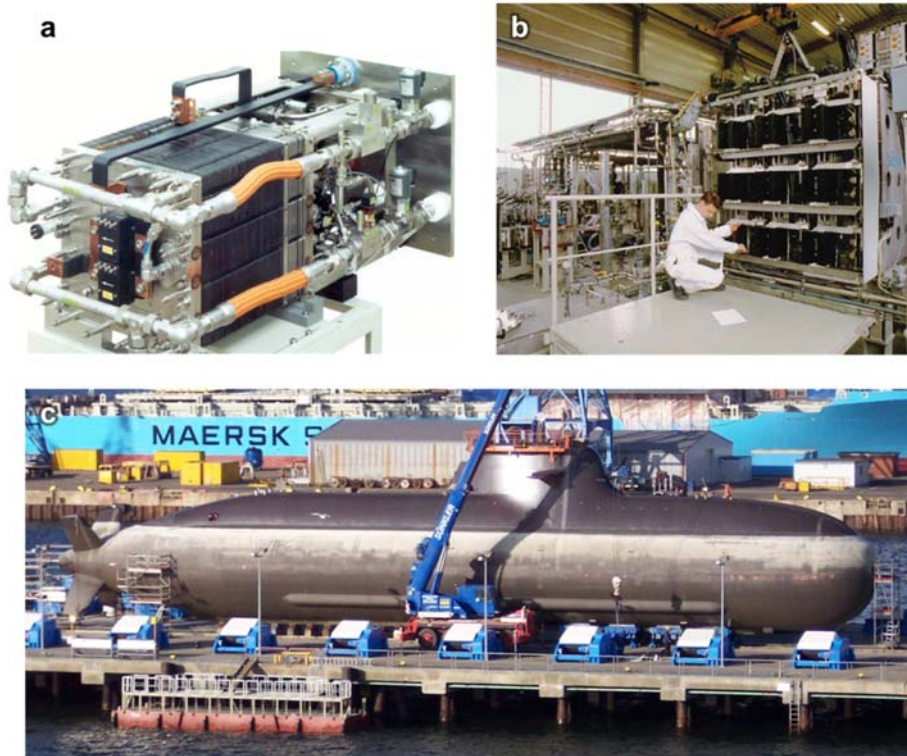


Figure 1.6 Type 212 submarine with fuel cell propulsion. a) A Siemens PEMFC Module as used on the German 212 AIP Submarine [Source: Howaldtswerke Deutsche Werft (HDW)], b) A Siemens 300 kW PEMFC Stack Assembly as used on the German 212 AIP Submarine, c) Type 212 submarine of the German Navy in dry dock. [Copyright Jane's Information Group; Source: HDW]

predecessor. This cost-optimized module is used in the submarines of Class 214. Moreover, a fuel cell power plant in its modular design is agile and it is possible that apply to the established submarines by refitment during a normal main overhaul sequence or a mid-life conversion, as is currently being realized for Class 209 submarines.

The plant's modular concept permits incorporation in the submarine either as an additional section (e.g. in Class 209) or as part of the whole design (as realized in the submarines Class 212A and 214). Class 214 is the first fuel cell-equipped submarine specifically designed for export customers. Class 214 combines the benefits of Class 212A with the proven design principles of Class 209. The Hellenic and the Republic of Korea Navy decided in favor of these boats due to the AIP advantage. The fuel cell system of Class 214 comprises two fuel cell modules of 120 kW each. In contrast to Class 212A, the oxygen tank is arranged inside the pressure hull, which offers greater flexibility in design and lower production cost. The oxygen tank and the hydride cylinders are clearly visible in outline and cut-away diagrams of the submarine.

Specifically, the fuel cell AIP system consists of reactant storage (H_2 and O_2), reactant water storage, interface for the submarine's control system and several auxiliary systems. However, oxygen storage is a mature technology

being accepted by several navies as the favored option for storing the oxygen for AIP systems. In contrast, hydrogen storage technologies are at an early stage of development with new systems being proposed, so the system of choice is not yet identified. For all fuel cell systems up to now, the hydrogen is stored in metal hydride cylinders; the oxygen is stored in liquid form (LOX) in tanks (Fig. 1.7). These storage systems will be described in the following paragraphs.⁶⁰

The hydrogen is stored in metal hydride cylinders, where it is bonded in the metal lattice structure of a special alloy. This method of storing hydrogen gives a higher volumetric density than liquid or especially high pressure gas storage and is conceivably the safest method of hydrogen storage. The metal hydride storage cylinders are completely maintenance-free, so they can be accommodated in the outer hull of the submarine. Due to their location outside the pressure hull, there is no danger of fuel leaking into the boat's atmosphere. Oxygen is stored on board in liquid form. The tanks are double-walled and vacuum-insulated. The first tank was exposed to extreme impact achieved in submarine shock tests to give evidence of sufficient tank strength and insulation. Since the size of the liquid oxygen storage facility is the limiting factor of all AIP options, the fuel cell system with the lowest oxygen consumption of all known systems offers the highest underwater endurance.⁶¹

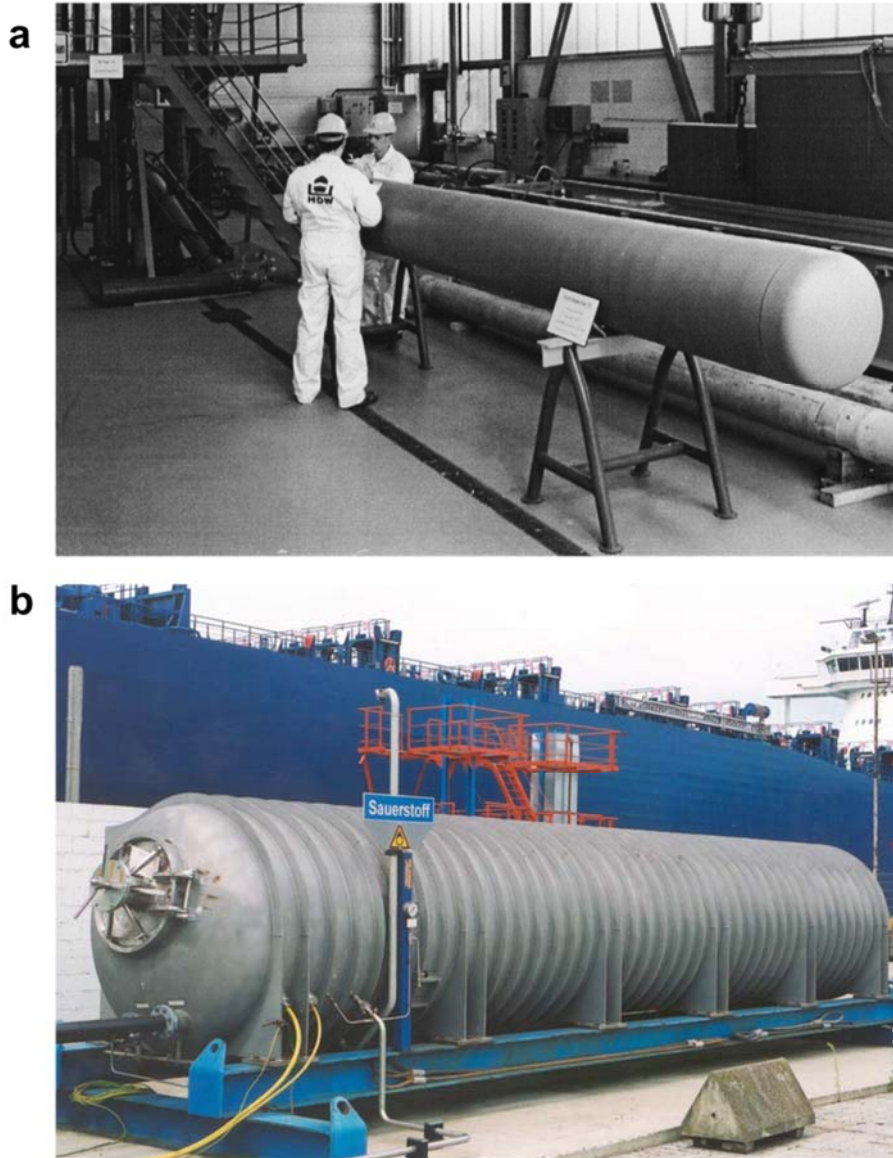


Figure 1.7 Reactant storage for submarines. a) Hydrogen storage in metal hydride cylinders, b) A liquid oxygen (LOX) tank on the German 212 AIP Submarine [Source: HDW].

For the first tests with the submarine U1, the AIP system was based on alkaline fuel cell technology because of the availability of that technology at the time. However, parallel to this test phase, PEMFC technology during recent years several navies have decided in favor of a fuel cell AIP system. The new Class 214 submarine was on order for the Greek and Republic of Korea Navy, and production started in February 2001. This is a clear indication of the general acceptance level of the fuel cell by navies operating submarines throughout the world, due to its advantages of low noise and infrared signatures, high efficiency and low maintenance requirements. Such qualities are essential for submarines that are expected to serve well into the future.

1.4 References

1. Barbir, F. *PEM Fuel Cells: Theory and Practice*, (Elsevier Academic Press, San Diego, 2005).
2. O'Hayre, R., Cha, S.-W. Colella, W. and Prinz, F. B. *Fuel Cell Fundamentals* (Wiley, New York, 2006)
3. Fuel Cell Today, *History*, <http://www.fuelcelltoday.com/about-fuel-cells/history>.
4. Wikipedia, *Fuel Cell*, http://en.wikipedia.org/wiki/Fuel_cell#cite_note-2.
5. 2004 Smithsonian Institute, *Fuel Cell Origins*, <http://americanhistory.si.edu/fuelcells/origins/orig1.htm>.
6. National Aeronautics and Space Administration, *Gemini: Bridge to the Moon*, http://www.nasa.gov/externalflash/gemini_gallery.
7. DOE Hydrogen and Fuel Cells Program, *FY2011 Progress Report for the DOE Hydrogen and Fuel Cells Program*, U.S. Department of Energy, (Washington, D.C. 2011).
8. Raistrick. I. D. *Modified gas diffusion electrode for proton exchange membrane fuel cells. In: Proceedings of the symposium on diaphragms, separation, and ion-exchange membranes.* (Ponnington (NJ): Electrochemical Society, 1986).

9. Zhang. J., *PEM Fuel Cell Electrocatalysts and Catalyst Layers, Fundamentals and Applications Part I*, (Springer-Verlag, London, 2008).
10. Zhang. J., Litteer. B. A., Gu. W., Liu. H. and Gasteiger. H. A. Effect of Hydrogen and Oxygen Partial Pressure on Pt Precipitation within the Membrane of PEMFCs, *J. Electrochem. Soc.* **154**, B1006 (2007).
11. Nonoyama. N., Okazaki. S., Weber. A. Z., Ikogi. Y. and Yoshida. T. Analysis of Oxygen-Transport Diffusion Resistance in Proton-Exchange-Membrane Fuel Cells, *J. Electrochem. Soc.* **158**, B416 (2011).
12. Ohma. A., Suga. S., Yamamoto. S. and Shinohara. K. Membrane Degradation Behavior during Open-Circuit Voltage Hold Test, *J. Electrochem. Soc.* **154**, B757 (2007).
13. Kim. J. H. *et al.*, Effects of Cathode Inlet Relative Humidity on PEMFC Durability during Startup–Shutdown Cycling I. Electrochemical Study *J. Electrochem. Soc.* **157**, B104 (2010).
14. Borup. R. *et al.* Scientific Aspects of Polymer Electrolyte Fuel Cell Durability and Degradation, *Chem. Rev.* **107**, 3904 (2007).
15. Wu. G., More. K. L., Johnston. C. M. and P. Zelenay, High-Performance Electrocatalysts for Oxygen Reduction Derived from

- Polyaniline, Iron, and Cobalt, *Science* **332**, 443 (2011).
16. Subbaraman. R., Strmcnik. D., Paulikas. A. P., Stamenkovic. V. R. and N. M. Markovic, Oxygen Reduction Reaction at Three-Phase Interfaces, *Chem. Phys. Chem.* **11**, 2825 (2010).
 17. Onishi. L. M., Prausnitz. J. M. and J. Newman, Water-Nafion Equilibria. Absence of Schroeder's Paradox, *J. Phys. Chem. B* **111**, 10166 (2007).
 18. Weber. A. Z. and Newman. J. Effects of Membrane- and Catalyst-Layer-Thickness Nonuniformities in Polymer-Electrolyte Fuel Cells, *J. Electrochem. Soc.* **154**, B405 (2007).
 19. Liu. W. and Zuckerbrod. D. In Situ Detection of Hydrogen Peroxide in PEM Fuel Cells, *J. Electrochem. Soc.* **152**, A1165 (2005).
 20. Debe. M. K., Schmoeckel. A. K., Vernstrom. G. D. and Atanasoski. R. High voltage stability of nanostructured thin film catalysts for PEM fuel cells, *J. Power Sources* **161**, 1002 (2006).
 21. Gancs. L., Kobayashi. T., Debe. M. K., Atanasoski. R. and Wieckowski. A. Crystallographic Characteristics of Nanostructured Thin-Film Fuel Cell Electrocatalysts: A HRTEM Study, *Chem. Mater.* **20**, 2444 (2008).
 22. Yoon. Y.-G. *et al.*, Effect of pore structure of catalyst layer in a

- PEMFC on its performance, *Int. J. Hydrogen Energy* **28**, 657 (2003).
- 23.Cho. Y.-H. *et al.* Effect of platinum amount in carbon supported platinum catalyst on performance of polymer electrolyte membrane fuel cell”, *J. Power Sources* **172**, 89 (2007).
- 24.Park. H.-S. *et al.* Performance enhancement of PEMFC through temperature control in catalyst layer fabrication, *Electrochim. Acta* **53**, 763 (2007).
- 25.Bender. G., Zawodzinski. T. A. and Saab. A. P. Fabrication of high precision PEFC membrane electrode assemblies, *J. Power Sources* **124**, 114 (2003).
- 26.Wang. X. *et al.* A bi-functional micro-porous layer with composite carbon black for PEM fuel cells, *J. Power Sources* **162**, 474 (2006).
- 27.Stampino. P. G. *et al.* Effect of different substrates, inks composition and rheology on coating deposition of microporous layer (MPL) for PEM-FCs, *Catal. Today* **147S**, S30 (2009).
- 28.Benitez. R., Soler. J. and Daza. L. Novel method for preparation of PEMFC electrodes by the electrospray technique, *J. Power Sources* **151**, 108 (2005).
- 29.Ihm. J. W., Ryu. H., Bae. J. S., Choo. W. K. and Choi. D. K. High performance of electrode with low Pt loading prepared by simplified

- direct screen printing process in PEM fuel cells, *J. Mater. Sci.* **39**, 4647 (2004).
30. Smirnova. A., Dong. X., Hara. H., Vasiliev. A. and Sammes. N. Novel carbon aerogel-supported catalysts for PEM fuel cell application, *Int. J. Hydrogen Energy* **30**, 149 (2005).
31. Taylor. A. D., Kim. E. Y., Humes. V. P., Kizuka. J. and Thompson. L. T. Inkjet printing of carbon supported platinum 3-D catalyst layers for use in fuel cells, *J. Power Sources* **171**, 101 (2007).
32. Cho. J. H. *et al.* Fabrication and evaluation of membrane electrode assemblies by low-temperature decal methods for direct methanol fuel cells, *J. Power Sources* **187**, 378 (2009).
33. Wilson M. S. and Gottesfeld. S. Thin-film catalyst layers for polymer electrolyte fuel cell electrodes, *J. Appl. Electrochem.* **22**, 1 (1992).
34. Wilson M. S. and Gottesfeld. S. High Performance Catalyzed Membranes of Ultra-low Pt Loadings for Polymer Electrolyte Fuel Cells, *J. Electrochem. Soc.* **139**, L28 (1992).
35. Wilson. M. S., Valerio. J. A. and Gottesfeld. S. Low Platinum Loading Electrodes for Polymer Electrolyte Fuel Cells Fabricated Using Thermoplastic Ionomers, *Electrochim. Acta* **40**, 355 (1995).
36. Tang. H., Wang. S., Pan. M., Jiang. S. P. and Ruan, Performance of

- direct methanol fuel cells prepared by hot-pressed MEA and catalyst-coated membrane (CCM), *Electrochim. Acta* **52**, 3714 (2007).
37. Ren. X., Wilson. M. S. and Gottesfeld. S. High Performance Direct Methanol Polymer Electrolyte Fuel Cells, *J. Electrochem. Soc.* **143**, L12 (1996).
38. Xie. J., More. K. L., Zawodzinski. T. A. and Smith. W. H. Porosity of MEAs made by “Thin Film Decal” Method and Its Effect on Performance of PEFCs, *J. Electrochem. Soc.* **151**, A1841 (2004).
39. Park. H.-S. *et al.* Modified Decal Method and Its Related Study of Microporous Layer in PEM Fuel Cells, *J. Electrochem. Soc.* **155**, B455 (2008).
40. Wieser. C. Novel polymer electrolyte membranes for automotive applications – requirements and benefits, *Fuel cells* **4**, 245-250 (2004)
41. Dunwoody. D. and Leddy. J. Proton exchange membranes: the view forward and back, *Electrochem. Soc. Interf.* **14**, 37-39 (2005)
42. Collier. A., Wang. H., Yuan. X., Zhang. J. and Wilkinson. D. P. Degradation of polymer electrolyte membranes, *Int. J. Hydrogen Energy* **31**, 1838-1854 (2006)
43. Fishtik. I., Callaghan. C. A., Fehribach. J. D. and Datta. R. A reaction route graph analysis of the electrochemical hydrogen oxidation and

- evolution reactions, *J. Electroanal. Chem.* **576**, 57-63 (2005)
44. Yeager. E. B., Electrocatalysts for O₂ reduction, *Electrochim. Acta* **29**, 1527-1537 (1984)
45. Bagotskii. V. S., Tarasevich. M. R. and Filinovskii. V. Y. Calculation of the kinetic parameters of conjugated reactions of oxygen and hydrogen peroxide, *Elektrokhimiya* **5**, 1218-1226 (1969)
46. Bagotskii. V. S., Tarasevich. M. R. and Filinovskii. V. Y. Accounting for the adsorption stage in a calculation of the kinetic parameters of oxygen and hydrogen peroxide reactions, *Elektrokhimiya* **8**, 84-87 (1972)
47. Su. D. S. and Sun. G. Nonprecious-metal catalysts for low-cost fuel cells, *Angew. Chem. Int. Ed.* **50**, 11570–11572 (2011).
48. Jaouen. F. *et al.* Recent advances in non-precious metal catalysis for oxygen-reduction reaction in polymer electrolyte fuel cells, *Energy Environ. Sci.* **4**, 114–130 (2011).
49. Chen. Z., Higgins. D., Yu, A., Zhang. L. and Zhang. J. A review on non-precious metal electrocatalysts for PEM fuel cells, *Energy Environ. Sci.* **4**, 3167–3192 (2011).
50. Yoo. S. J. *et al.* Promotional effect of palladium on the hydrogen oxidation reaction at a PtPd alloy electrode, *Angew. Chem. Int. Ed.* **47**,

- 9307–9310 (2008).
51. Jung. N. *et al.* Preparation process for improving cathode electrode structure in direct methanol fuel cell, *Electrochem. Commun.* **12**, 754–757 (2010).
52. Cho. Y.-H. *et al.* Enhanced performance and improved interfacial properties of polymer electrolyte membrane fuel cells fabricated using sputter-deposited Pt thin layers, *Electrochim. Acta* **53**, 6111–6116 (2008).
53. Therdthianwong. A., Ekdharmasuit. P. and Therdthianwong. S. Fabrication and performance of membrane electrode assembly prepared by a catalyst-coated membrane method: Effect of solvents used in a catalyst ink mixture, *Energy Fuels* **24**, 1191–1196 (2010).
54. Fischer. A., Jindra, J. and Wendt, H. Porosity and catalyst utilization of thin layer cathodes in air operated PEM-fuel cells, *J. Appl. Electrochem.* **28**, 277–282 (1998).
55. Miao. F. and Tao. B. Methanol and ethanol electrooxidation at 3D ordered silicon microchannel plates electrode modified with nickel–palladium nanoparticles in alkaline, *Electrochim. Acta* **56**, 6709–6714 (2011).
56. Wang. C. *et al.* Proton exchange membrane fuel cells with carbon

- nanotube based electrodes, *Nano Lett.* **4**, 345–348 (2004).
57. Yuan. F. L. and Ryu. H. J. The synthesis, characterization, and performance of carbon nanotubes and carbon nanofibres with controlled size and morphology as a catalyst support material for a polymer electrolyte membrane fuel cell, *Nanotechnology* **15**, S596–S602 (2004).
58. Michel. M. *et al.* High-Performance Nanostructured Membrane Electrode Assemblies for Fuel Cells Made by Layer-By-Layer Assembly of Carbon Nanocolloids, *Adv. Mater.* **19**, 3859–3864 (2007).
59. Lakeman. J. B. and Browning. D. J. “*The Role of Fuel Cells in the Supply of Silent Power for Operations in Littoral Waters*” Paper presented at the RTO AVT Symposium on “Novel Vehicle Concepts and Emerging Vehicle Technologies”, held in Brussels, Belgium, published in RTO-MP-104 (7-10 April 2003).
60. Psoma. A. and Sattler. G. Fuel cell systems for submarines: from the first idea to serial production *Journal of Power Sources* **106** 381 (2002).
61. Sattler G and Pommer. H. *Storage of Reactants for PEM FC Systems Aboard Submarines*. WARSHIP ‘96, International Symposium on Naval Submarines (5 June 1996).

Chapter 2

Ordered macroporous Platinum electrode and enhanced mass transfer in fuel cells using inverse opal structure

2.1 Abstract

Three-dimensional, ordered macroporous materials such as inverse opal structures are attractive materials for various applications in electrochemical devices because of the benefits derived from their periodic structure: their relatively large surface areas, large voidage, low tortuosity, and their interconnected macropores. However, the direct application of an inverse opal structure in membrane electrode assemblies (MEA) has been considered impractical because of the limitations in fabrication routes including an unsuitable substrate. Here, we report the demonstration of a single cell that maintains an inverse opal structure entirely within an MEA. Compared with

the conventional catalyst slurry, an ink-based MEA, this modified MEA has a robust and integrated configuration of catalyst layers; therefore, the loss of catalyst particles can be minimized. Furthermore, the inverse-opal-structure electrode maintains an effective porosity and an enhanced performance, as well as improved mass transfer and more effective water management, owing to its morphological advantages.

2.2 Introduction

Hydrogen is the most abundant element on Earth. It can be converted into non-polluting, zero-emission renewable energy, it is unlikely to be subject to geopolitical pressures or scarcity concerns, and it does not contribute to global warming through CO₂ emissions. It shows good performance in fuel cells, which can have 2.5 times the efficiency of internal-combustion engines.¹ Consequently, such fuel cells are considered a promising future technology for energy conversion.^{2,3} Among the various kinds of fuel cells, polymer electrolyte membrane fuel cells (PEMFCs) are the most encouraging for commercial applications. However, the key factor in fuel cell performance is the structure of the electrode in the membrane electrode assembly (MEA). Hence, optimization and modification of electrode structure has proven to be critical for improving the performance and durability of PEMFCs.^{4,5} Accordingly, several attempts have been made to enhance mass transfer and improve water management through careful design of the electrode structure, for example, the use of an additional solvent to control the polarity,⁶⁻⁸ application of a pore-forming agent,⁹ and optimization of the ionomer content.¹⁰ Furthermore, three-dimensional (3D) nanostructured materials have been introduced for catalyst supports including carbon nanotubes (CNTs), carbon nanofibers, layer-by-layer

assemblies, and inverse opal structures.¹¹⁻¹⁵ However, ordered, carbon-based catalyst supports such as CNTs are acquired through a difficult, costly fabrication process. Moreover, the corrosion and oxidation of carbon supports is also a major problem that can restrict the durability of the catalyst.¹⁶⁻¹⁹ The loss of catalytic Pt particles within a catalyst layer can occur in conventional catalyst slurry (ink-based MEA). This has prompted the formation of catalyst layers that consist of carbon-supported Pt particle clusters and ionomer aggregations, via a random bottom-up approach. Accordingly, balancing these conflicting and inter-related requirements remains an intricate problem, and the fabrication of a satisfactory, ordered nanostructured electrode has not yet been achieved. Therefore, finding ways to improve upon these current methods is a major priority.

Mass transport in a fuel cell is affected by convection in flow channels and diffusion across electrodes. Electrochemical reactions on one side of an electrode, and convective mixing on the other side of the electrode, cause concentration gradients, leading to diffusive transport across the electrode. Diffusional flux and limiting current are affected by the effective diffusivity, electrode thickness, and tortuosity.²⁰ Moreover, not all of the catalysts used to construct the fuel cell electrodes are accessible to reactants (*e.g.* protons and oxygen). In disorderly structured electrodes such as conventional MEAs

(Fig. 2.1a), gas molecules tend to be impeded by pore walls and other particles; therefore, the effective diffusivity is lower than that for an inverse-opal-structure Pt electrode (denoted hereafter as an IO electrode, Fig. 2.1b). However, an IO electrode shows enhanced mass diffusivity resulting from its open and interconnected pore architecture, and it is possible to produce a thinner electrode. In addition, this electrode is free from the release of disconnected particles, owing to robust and wholly integrated catalyst layer structures.

Template fabrication using self-assembled closely packed colloidal spheres is a general method of preparing 3D ordered macroporous (3DOM) materials.²¹⁻²⁵ Such ordered materials have previously been investigated for potential use in various applications including photonic crystals, optical sensors, catalysts, capacitors, dye-sensitized solar cells, battery materials, and fuel cells.²⁶⁻³² This is because of the benefits that result from the periodic structure of ordered materials, their relatively large surface areas, and their interconnected macropores. For example, if a 3DOM material is introduced into an electrochemical device, such as an MEA in a PEMFC (Fig. 2.1b), the morphological advantages from the open surface and interconnected pore architecture of electrodes are manifold: 1) The architecture consists of highly open, short diffusion pathways with reduced resistance and low tortuosity,

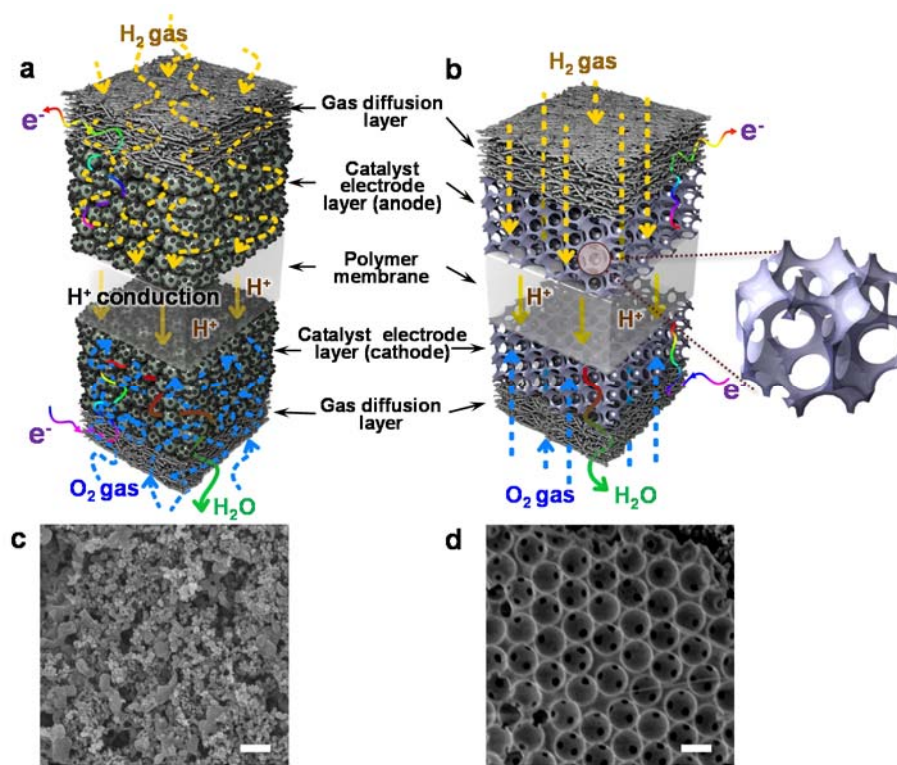


Figure 2.1 Conceptual diagrams of two MEAs. (a) Conventional MEA with catalyst-coated membrane (CCM), (b) Modified MEA with inverse-opal-structure (IO) electrode examined in this study. (c) Field-emission scanning electron microscopy image of a CCM surface prepared by commercial Pt/C ink spraying. (d) Field-emission scanning electron microscopy image of an IO electrode surface prepared by pulse electrodeposition according to colloidal crystal templating methods. Scale bar 500 nm.

which facilitate improved mass transport and increased conductivity compared with a tortuous structure. 2) The architecture also has a larger interfacial area, on which the electrode reaction can occur, and an increased number of active sites per unit MEA area, which leads to an improvement in the apparent reaction rate. 3) The architecture also exhibits reduced thickness leading to increased conductivity of both reactants and ions, so that the ionomer can be unnecessary. 4) The architecture also exhibits interconnected grains that result in a reduced release of disconnected particles into the surrounding environment. Thus, it has been demonstrated that 3DOM materials can enhance the performance of an individual electrode.³³

Nevertheless, the application of inverse opal materials to electrodes in fuel cells has been limited to solid oxide fuel cells,³⁴⁻³⁶ and applications in PEMFCs have been restricted to only a small number of components. This is probably the result of the significant limitations in fabrication routes for inverse opal materials. Most notably, the ideal substrate for self-assembly of colloidal spheres is a planar, non-porous, and chemically homogeneous surface; yet, most active devices such as gas diffusion layers (GDLs) and polymer membranes in PEMFCs have rough surfaces, are chemically heterogeneous, and are often porous.³⁷ Because of these properties, the direct application of an IO electrode in MEAs in PEMFCs has been considered

impractical. Without an additional transfer process, a single cell that maintained an inverse opal structure entirely within an MEA was considered impossible. Previous attempts to introduce an inverse opal structure into PEMFCs have been limited to the electro catalysis of half-cells,³⁸⁻⁴¹ catalyst supports,¹¹⁻¹⁹ or membranes.⁴²⁻⁴⁴ To the best of our knowledge, there have been no reports on their practical use as electrodes, or on their single-cell performance; thus, the benefits arising from their structure have not been properly determined.

Therefore, this paper reports on the direct application of an IO electrode to MEAs in PEMFCs, without any additional transfer process at the electrodes. This is achieved using electrodeposition following colloidal crystal templating methods. Furthermore, the performance of an IO electrode is demonstrated in a practical device. The enhanced mass transfer of an IO electrode and its characteristic performance are also discussed.

2.3 Experimental Section

Materials and Characterization

Commercially available solvents and reagents were used without further purification unless otherwise noted. Carboxylated PS latex particles with a mean diameter of 520 nm in a 10 wt% aqueous suspension were obtained from Thermo Fisher Scientific, Inc. The surface morphology and thickness of the PS colloidal crystal template and the IO Pt electrode were characterized using FE-SEM (Carl Zeiss, SUPRA 55VP). AFM was carried out to identify the surface structure and roughness of the electrodes. XPS were obtained from an Al K α source (ESCALAB 250 XPS spectrometer, VG Scientifics). Binding energies were calibrated with respect to C (1s) at 285 eV. Experimental data were curve-fitted using AVANTAGE4.19 software. The Pt in the IO electrodes was examined using XRD (Rigaku Corp., D-MAX2500 152-PC) with CuK α radiation (40 kV, 200 mA) at room temperature. The loading mass of Pt on the GDLs was estimated using ICP-optical emission spectroscopy (Varian, Varian 820-MS). Prior to analysis, the catalysts were dissolved in aqua regia for 24 h and then diluted to a certain concentration. Assembled single cells (CNL-PEM005-01, CNL Energy) were tested using the current sweep-hold method with a fuel cell test system

(CNL Energy). Cyclic voltammetry (CV) with a potentiostat/galvanostat (IM-6, Zahner) was used to determine the ECSA. Electrochemical measurements were carried out using an Autolab potentiostat (PGSTAT128N) in a standard three-compartment electrochemical cell with an IO electrode, Pt plate, and saturated calomel electrode as the working, counter, and reference electrodes, respectively. All potentials are quoted with respect to that of a normal hydrogen electrode, and all measurements were conducted at room temperature.

Preparation of opal-structure PS template

The substrate (GDLs) were soaked in a 1,2-ethanedithiol solution in ethanol (10 mM) for at least 12 h prior to PS bead deposition to enhance adhesion between the substrate and colloid; 0.36 g of the 0.5 wt% non-ionic surfactant (IGEPAL[®] Co-30) and 80 mL of Milli-Q water were mixed together, and 0.5 g of PS suspension were added. The mixtures were then ultrasonicated for 30 min, placed in an oven, and dried at 65°C for more than 2 d, under a constant relative humidity.

Fabrication of inverse-opal-structure Pt electrode

Galvanostatic, pulsed electrodeposition of Pt onto the template was

performed in a three-electrode cell with a Pt plate counter electrode and an Ag/AgCl reference electrode using an Autolab potentiostat (PGSTAT128N). The substrate, GDL (SGL 35BC carbon paper), was purchased from the SGL Group. The GDL substrate under the template served as the working electrode. Electrodeposition was carried out in a plating bath containing a solution of 10 mM H_2PtCl_4 dissolved in 10 mM KCl. The duty cycle (%) of the pulsed electrodeposition is defined as $[\theta_1/(\theta_1 + \theta_2)] \times 100$, where θ_1 = on-time, and θ_2 = off-time. The morphology of the IO electrode changed with variations in the duty cycle and current density. The parameters chosen in this work were a peak current density of $50 \text{ mA}\cdot\text{cm}^{-2}$, an on/off time of 50/100 ms, and a total charge of $4 \text{ C}\cdot\text{cm}^{-2}$. The actual amount of Pt deposited onto the GDL was about $0.12 \text{ mg}\cdot\text{cm}^{-2}$, as confirmed using ICP mass spectrometry. After deposition, PS particles were removed by soaking in toluene for 12 h. The GDL was removed from the solution and was washed with water. The electrode was heated in a furnace at 130°C in air for 4 h to remove the water and the contaminants contained in the interstitial spaces of the inverse opal. During the second step, the electrode was heat-treated at 180°C for 2 h under H_2 to remove any remaining organic solvent, and to minimize Pt oxidation. The second step is optional.

MEA fabrication

The typical MEA fabrication procedure has been described elsewhere.^{6,7} A Nafion[®] 212 membrane (DuPont) was used for the ion-conducting membrane, which was immersed in a 2.5% H₂O₂ solution at 80°C for 1 h and then rinsed in boiling deionized water for 1 h for purification. The membrane was then boiled in a 0.5 M H₂SO₄ solution for 1 h and rinsed in deionized water for protonation. An IO electrode was used as the cathode and 40 wt% Pt/C (Johnson Matthey Co.) was used as the anode catalyst. The Pt/C catalyst was dispersed in a mixture of isopropyl alcohol, deionized water, and perfluorosulfonic acid ionomer (Aldrich, 5 wt% Nafion[®] ionomer) to prepare the catalyst ink. The latter was ultrasonicated for 15 min and sprayed onto the anode side of a Nafion[®] 212 membrane. The volume of catalyst ink was controlled to deposit 0.12–0.20 mg Pt·cm⁻² in order to prepare the catalyst-coated membranes (CCMs). SGL 35BC carbon paper was used as a GDL, and it was placed on the anode side of the CCMs. The MEAs were inserted into a single-cell unit that had a graphite plate with a serpentine gas flow channel (5 cm² area). A single-cell unit was assembled with eight screws and a tightening torque of 8 N·m. Activation and polarization tests of the assembled single cells were performed using the current sweep-hold method with a fuel cell test system. The current was

maintained for 10 min when the current density reached each of the following values, 0.5, 1.0, 1.5, 2.0, 2.5, 3, and 4 A·cm⁻², during a 10 mA·cm⁻² s⁻¹ current sweep rate. During activation, the current was reset to zero when the cell voltage reached 0.35 V. Polarization curves were measured using the current-sweep method and the PEMFC test system. The test was conducted using fully humidified H₂/O₂ (or air), which was supplied to the anode and cathode, respectively, during activation and the polarization tests. The total outlet pressure was 150 kPa with an anode stoichiometry of 2, a cathode stoichiometry of 9.5 for O₂, and an air stoichiometry of 2. The cell temperature was maintained at 80 °C during activation and at room temperature during the polarization test. The catalyst loading was 0.12 mg·cm⁻². For the cathodic dead-end mode, the flow rate of O₂ was minimized and the outlet of the cell was closed.

Electrochemical characterization

The ECSA of the cathode catalyst layer was estimated using CV. After the polarization test, the single cell was purged with humidified N₂ gas on both cell sides for 12 h to remove reactant gases. Humidified H₂ and N₂ gases (99.999%) were supplied to the anode and cathode sides, respectively, and the cell temperature was maintained at 30°C to measure the CV after N₂

purging. The voltage sweep range of the CV was 0.05–1.20 V, and the scan rate was 100 mV·s⁻².

2.4 Result and Discussion

Self-assembly of polystyrene beads

A schematic diagram illustrating the fabrication of an IO electrode and the corresponding field-emission scanning electron microscopy (FE-SEM) images of the latter are shown in Fig. 2.2. Most substrates that have been used for template fabrication of IO structures have had flat and even surfaces, *e.g.* glass slides, Si wafers, indium tin oxide, and fluorine-doped tin oxide. However, in the present study, GDLs containing microporous layers (MPLs; 35BC, SGL), which are generally utilized as GDLs in PEMFCs, were used as substrates to directly apply an IO structure into MEAs, without an additional electrode transfer process. The MPLs consist of carbon black and 5 wt% of polytetrafluoroethylene; thus, the surfaces of MPLs are rough and uneven compared with those of the substrates used in previous studies. Consequently, a simple substrate pretreatment must be performed before polystyrene (PS) bead deposition. Atomic force microscopy (AFM) images and corresponding FE-SEM images for the surface morphology of pristine GDL are shown in Fig. 2.3. The surface is jagged and rough because of carbon black particles agglomerating together to form larger clusters. However, the number of void spaces on the GDL surface is

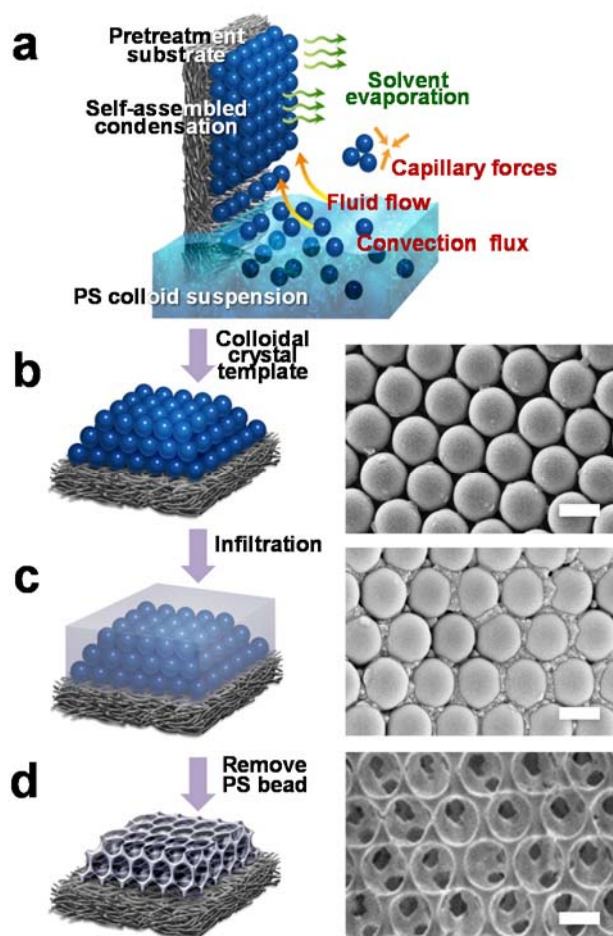


Figure 2.2 Schematic diagram of the fabrication process. (a) Vertical deposition of PS beads on a pretreated substrate (GDL). (b) Self-assembly of a colloidal crystal template on GDL. (c) Infiltration and pulse electrodeposition. (d) Removal of colloidal crystal template by soaking in toluene. Scale bar 500 nm.

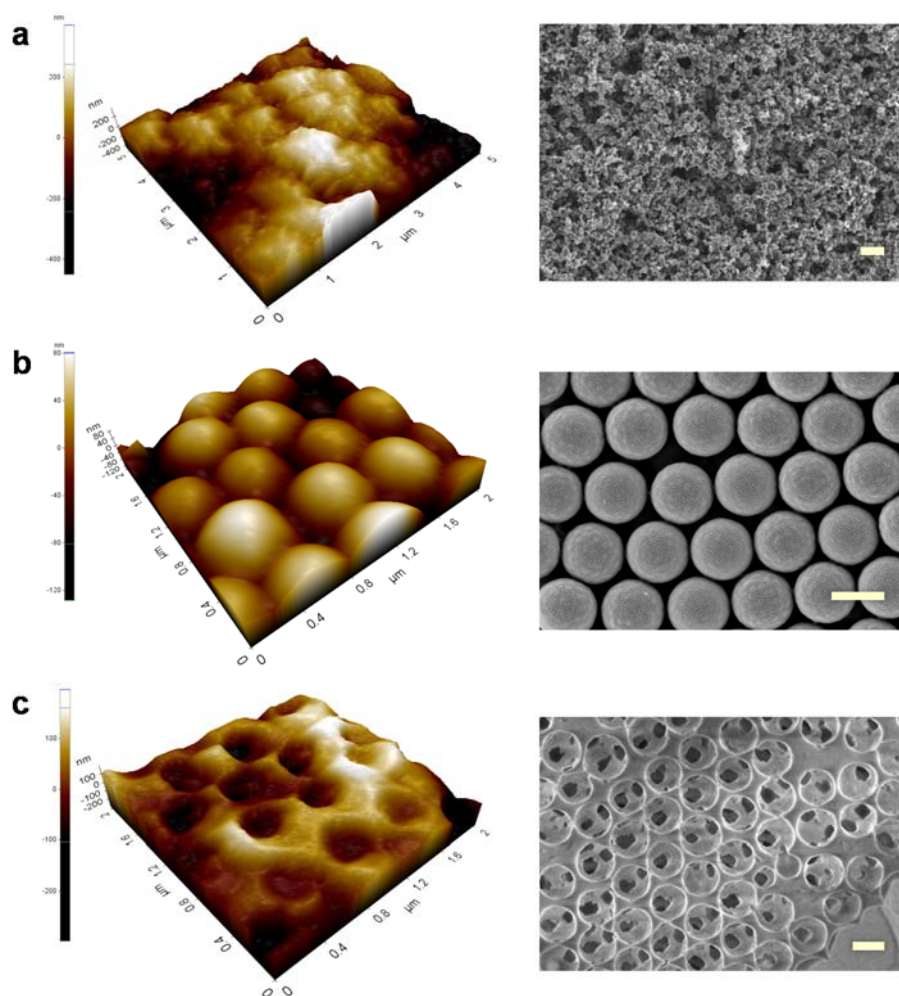


Figure 2.3 AFM and corresponding FE-SEM images of a PS crystal template on GDLs. (a) Pristine GDL substrate before PS deposition. (b) After PS deposition. (c) After Pt electrodeposition and removal of colloidal crystal template. Scale bar 500 nm.

negligible compared to the size of colloids used for templating. The GDLs were soaked in a solution of 1,2-ethanedithiol in ethanol to enhance adhesion between the substrate and the colloid. It was not possible to deposit PS beads onto the GDLs without the presence of MPLs (*e.g.* GDLs of Toray, Japan), since there was a lack of carbon and alkanethiols on the substrate surface, although they were prepared using the same pretreatment. The formation of self-assembled monolayers of thiols on gold surfaces is well known but there have only been a few studies reported on the adsorption of organic thiols on carbon. However, carbon black has a surface with energetic heterogeneity, and the most active sites are graphite edges.^{45,46} As a consequence, alkanethiols will be adsorbed spontaneously along the edges of a crystal by oxidative addition and reductive elimination of head-thiol groups. These adsorbed alkanethiols can act as a type of binder or coupling agent by interacting with the carboxyl groups on the PS surface and the terminal-thiol groups on the carbon black surface. In the present study, 0.5 wt% of non-ionic surfactant was added to a PS colloid suspension to facilitate self-assembly and crystallization of the PS beads. When added in water, surfactant molecules strongly positively adsorb at the PS bead surfaces, changing the properties of the suspension, including its hydrophilicity and surface tension. PS particles were self-assembled, and a structured crystal

template was produced by water evaporation and sequential convective flux during vertical deposition.⁴⁷⁻⁴⁹ When the water was evaporated from the meniscus, particles were continuously transported to the vicinity of the triple-phase contact line by convective fluid flow of the surrounding suspension. Simultaneously, capillary forces in the drying film pulled the spheres together to form an ordered, closely packed structure (Fig. 2.3b). A more uniform surface with fewer defects was obtained by diluting the PS suspension with ethanol, while faster evaporation resulted in a thicker template. The thickness of the template was controlled by modifying the solvent evaporation rate or the solution concentration; a related equation with other parameters has previously been reported to explain this phenomenon.⁴⁹

Fabrication of IO Pt electrode and MEA

For Pt infiltration into a PS template, galvanostatic pulsed electrodeposition onto the template was performed. The corresponding results and SEM images of the GDL surface are shown in Fig. 2.4. Also, large-area SEM images of the IO electrode are shown in Fig. 2.4. The GDL substrate under the template served as a working electrode. Pulsed electrodeposition was used because this method has the distinct advantage of improving the

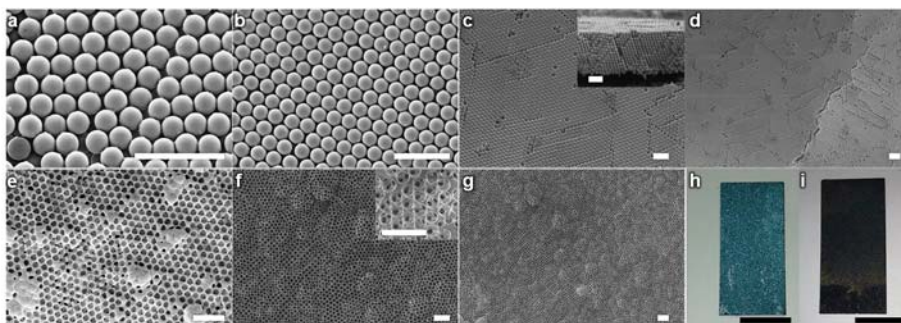


Figure 2.4 Field-emission scanning electron microscopy images of various electrodes. (a, b, c, d) Polystyrene crystal template on GDLs (inset of (c): cross-sectional image), scale bar 2 μm . **(e, f, g)** IO electrodes on GDLs (inset of (f): closer look), scale bar 2 μm . **(h, i)** Photograph of actual electrode on gas diffusion layer after PS deposition **(h)** and PS removal **(i)** following electrodeposition, scale bar 2 cm.

physical properties of the deposit and its adherence to the substrate. In addition, nucleation and growth can be controlled separately by adjusting the potential pulse amplitudes and the duration of deposition.⁵⁰ The current density, duty cycle, and charge density were changed to produce an electrode surface with better morphology.

Theoretically, when a larger current density is applied to an electrode, the overpotential increases; this means that the nucleation rate increases, resulting in a finer crystal grain. However, in the present case in this study, for a current density higher than $100 \text{ mA}\cdot\text{cm}^{-2}$, the nucleation and crystal growth rates were fast enough to penetrate and fill the void spaces of the PS template. Under those conditions, Pt grains formed on the surface of the PS bead and created a larger cluster. Also, at this high current density, the hydrogen evolution reaction occurred rapidly and destroyed the existing morphology of the IO electrode. A duty cycle of 16.7% and a charge density of $50 \text{ mA}\cdot\text{cm}^{-2}$ resulted in the most uniform morphology (red dot line in Fig. 2.5). The total charge density was fixed at $4 \text{ C}\cdot\text{cm}^{-2}$, which implies that the theoretical Pt loading was $0.2 \text{ mg}\cdot\text{cm}^{-2}$. However, the actual amount of Pt deposited onto the GDL was about $0.12 \text{ mg}\cdot\text{cm}^{-2}$, as determined using inductively coupled plasma (ICP) mass spectrometry. The thickness of each IO electrode was approximately 1–2 μm ; therefore, a total charge

| On/off time | | 100/300 | 50/300 | 5.2/70 |
|-----------------|-----------------------------|---------|--------|--------|
| Duty cycle | | 25.0% | 14.3% | 6.9% |
| Current density | 25 mA/cm^2 | | | |
| | 50 mA/cm^2 | | | |
| | 75 mA/cm^2 | | | |
| | 100 mA/cm^2 | | | |

Figure 2.5 FE-SEM images of IO electrode. The electrodeposition conditions such as potential pulse amplitudes, the duration of deposition and the current densities were varied for the optimum morphology. The scale bar of each picture was omitted.

of $1 \text{ C}\cdot\text{cm}^{-2}$ was deposited, corresponding to a Pt deposit of $0.03 \text{ mg}\cdot\text{cm}^{-2}$ and a thickness of about $0.5 \text{ }\mu\text{m}$. PS spheres were deposited with 5–20 layers on GDL and the corresponding thickness was around $3\text{--}12 \text{ }\mu\text{m}$. In the case of the inverse-opal-structure Pt spheres, the thickness was around 3–4 layers ($1.5\text{--}2 \text{ }\mu\text{m}$). The thickness was determined by considering the restricted Pt amounts, the preserved IO structure, and the smooth proton transfer. Considering that typical thickness values of conventional electrodes in PEMFCs are about $5\text{--}10 \text{ }\mu\text{m}$, the IO electrode is superior to conventional electrodes having a shorter diffusion path and increased conductivity of the reactants and ions, which means that the use of an ionomer for proton transfer is unnecessary.

An inverse duplicate of the hexagonal close-packed structure, which has a packing factor of 0.74, consists of closely packed planes of PS beads. For the opal-structure template, the skeletal walls enclose macropores that are interconnected through holes at the points where the original PS beads touch. Indeed, the structure of inversed opal materials, which are obtained from electrodeposition based on colloidal crystal templating methods, is usually formed by filling the interstitial spaces of the template with the desired materials. However, this phenomenon was not observed in this study. Instead, Pt surrounds the PS spheres, creating a shell (Figs. 2.1b, 2.2d SEM images).

The thickness of the Pt walls was determined to be approximately 10–15 nm, and this was calculated using SEM images and approximate calculations of the surface ratio (see Supplementary Information for details).

X-ray diffraction (XRD) analysis was performed to verify the presence of the Pt component on the IO electrode (Fig. 2.6). Three major peaks at 40.06, 46.54, and 67.86° in the spectrum correspond to Pt(111), (200), and (220) planes, respectively. Characteristic peaks at around 27° arise from the carbon in the MPL of the GDL. The size of the Pt grains that formed on the IO-electrode-based MEA was calculated to be around 8–11 nm using the Scherrer equation and XRD data. In addition, to further characterize the surface Pt of the IO electrode, X-ray photoelectron spectra (XPS) (Fig. 2.7) were obtained. The oxidation states of Pt in the IO electrode are quite different from those in conventional Pt/C electrodes. The XPS spectra in Fig. 2.8 show that the Pt 4f core-level peaks of Pt/C of the conventional electrode are mainly derived from Pt(0), but in the case of the IO Pt electrode, the main peak comes from Pt(II). In addition, the distribution of Pt oxidation states in the IO electrode is different from that of Pt/C in the conventional electrode (Table 2.1). However, these observations are not of major relevance to the performance of the cell, since the oxidation state of

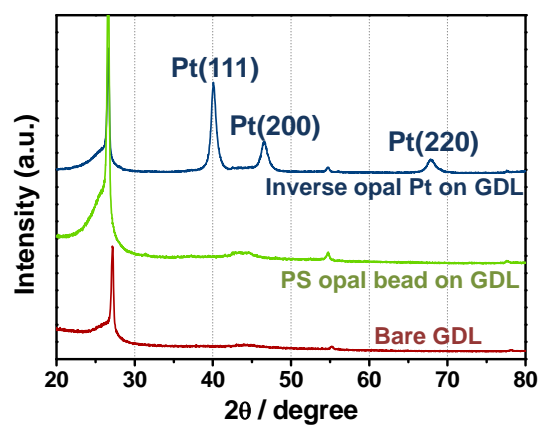


Figure 2.6 XRD patterns of electrodes. IO electrode (blue), PS crystal template (khaki) and bare GDL (red).

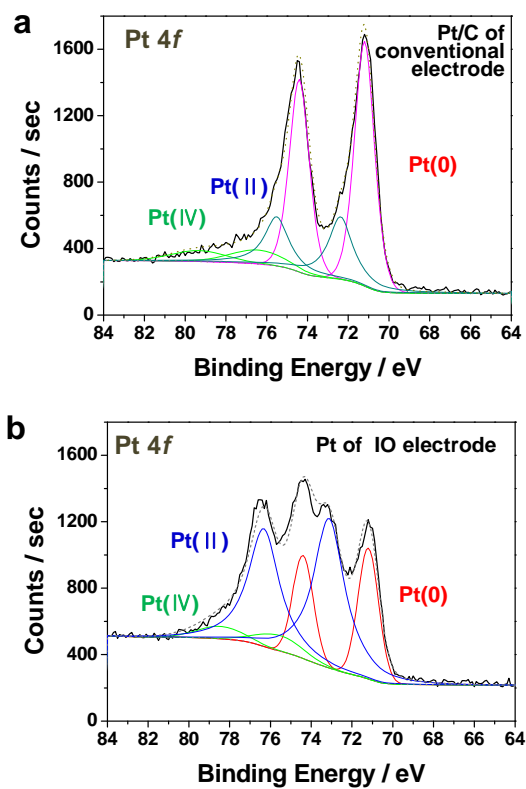


Figure 2.7 XPS spectra of Pt 4f. (a) Pt/C of conventional electrode and (b) Pt of IO electrode.

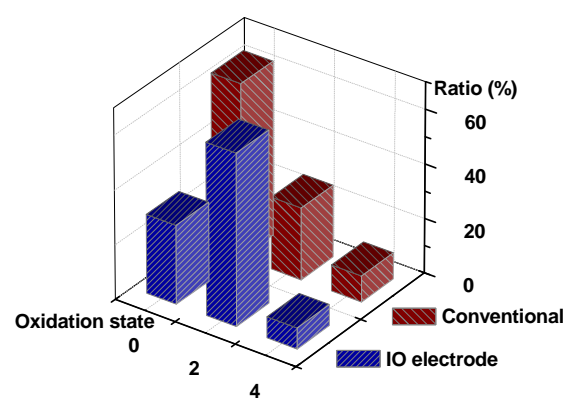


Figure 2.8 The ratio of Pt Pt oxidation properties of electrodes.

Table 2.1 Pt oxidation states from electrode surface XPS peak analysis.

| Material | Element | Oxidation states | Binding energy (eV) | Ratio (%) |
|--------------------------------|---------|------------------|---------------------|-----------|
| Pt/C of conventional electrode | Pt 4f | Pt (0) | 71.20 | 63.91 |
| | | Pt (II) | 72.38 | 26.49 |
| | | Pt (IV) | 75.09 | 9.60 |
| Pt of IO electrode | Pt 4f | Pt (0) | 71.20 | 28.95 |
| | | Pt (II) | 73.13 | 63.31 |
| | | Pt (IV) | 75.56 | 7.72 |

the Pt surface is susceptible to heat treatment conditions and easily changes during the cell operation.⁴

A modified MEA was fabricated using the electrodeposited IO electrode as a cathode to test the performance of the IO electrode in a practical device (Fig. 2.9). The ionomer in the catalyst layer serves as a binder, proton conductor, and hydrophilic agent, and it improved the catalyst utilization.⁵¹ Nevertheless, the ionomer was unnecessary for the IO electrode in this study. In addition, although there were no ionomers in the cathode catalyst, the performance did not decrease because the geometrical advantages of the IO structure and the short diffusion pathway of the thinner electrode. Moreover, the active area of the electrode was 5 cm², which was a relatively large area in the case of IO-structure applied materials.²³ In the fuel cell system, the dead-end mode requires neither fuel nor an oxidant supplying device, such as a blower, fan, or recirculation unit; therefore, improved efficiency and a simplified system are expected.⁵² Thus, in addition to standard fuel cell test condition from US Department of Energy's reference, the cathodic dead-end mode was also used with the IO electrode to widen its potential use in applications such as micro fuel cells.

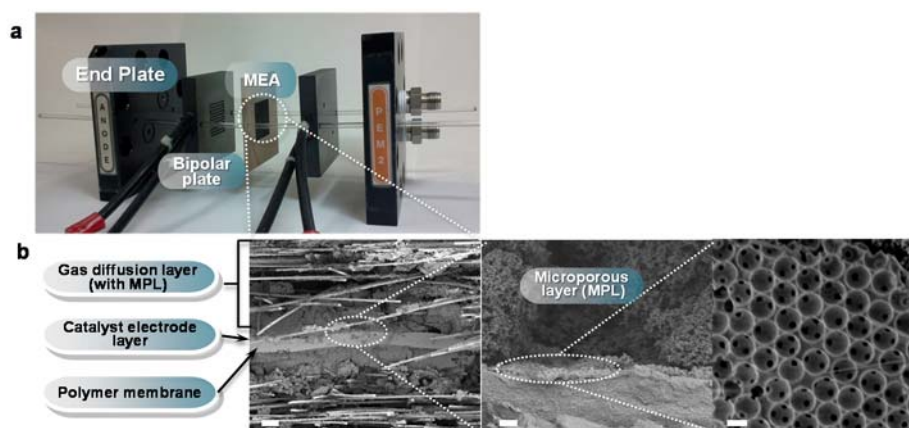


Figure 2.9 Photograph of practical PEMFC single cell. (a) Membrane electrode assembly (MEA) in single cell used for this study. **(b)** Cross-sectional field-emission scanning electron microscopy images of MEA with inverse-opal-structure electrode on gas diffusion layer (scale bar 50 μm , 2 μm and 500 nm).

Performance of IO-electrode-based MEA

The polarization and power density curves for two MEAs are shown in Fig. 2.10. They were measured in cathode dead-end mode with a fully humidified gas at 70°C (Fig. 2.10a), and under ambient humidity at room temperature (Fig. 2.10b). Fig. 2.10c ($0.12 \text{ mg}_{\text{Pt}}\cdot\text{cm}^{-2}$) and 2.10d ($0.20 \text{ mg}_{\text{Pt}}\cdot\text{cm}^{-2}$) were obtained from the US Department of Energy's reference conditions with air. The polarization curves in the presence of oxygen, which show remarkably high power densities, are shown in Fig. 2.11. The performances of IO-electrode-based MEAs in PEMFCs are higher than those of conventional MEAs with a similar Pt loading because of morphological advantages, enhanced effective diffusivity from the open electrode surface, and interconnected pore architecture. All of these characteristics result in uncomplicated access of the reactant to the catalyst. The current density for the conventional MEA was $235 \text{ mA}\cdot\text{cm}^{-2}$; this was measured for a catalyst loading of $0.12 \text{ mg}\cdot\text{cm}^{-2}$ at 0.6 V under fully humidified operating conditions (Fig. 2.10a). The equivalent current measured under the same conditions for an IO-electrode-based MEA with a similar Pt loading was $440 \text{ mA}\cdot\text{cm}^{-2}$ (185% higher). In the case where the measurements were carried out under standard conditions with H_2/air (Figs. 2.10c, d), the performances of the IO-electrode-based MEAs were also better. The IO electrode fuel cell shows a

slightly

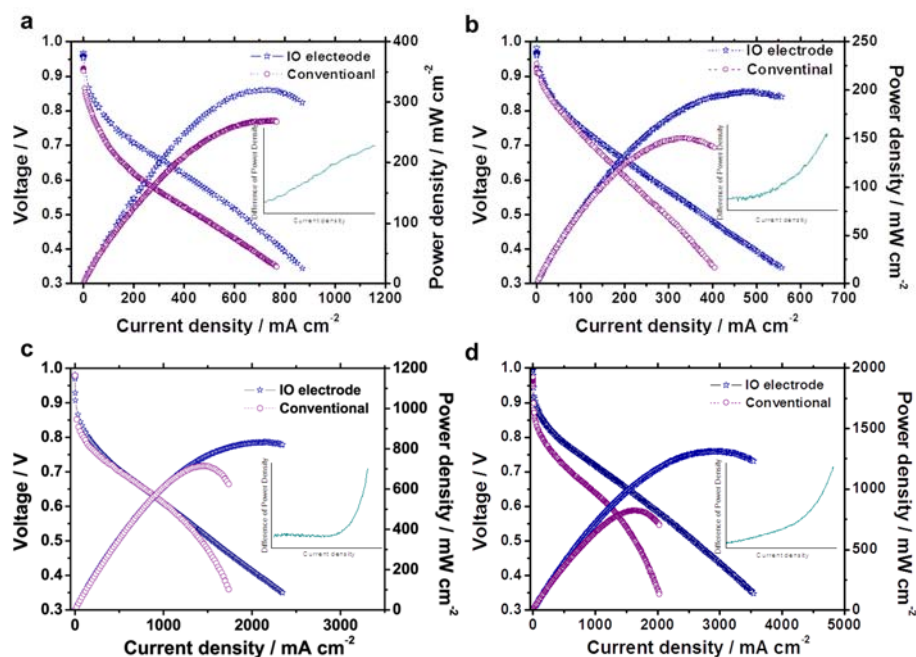


Figure 2.10 Polarization curves of IO electrode-based MEAs. (a) Using a fully humidified H_2/O_2 supplement and maintained at 80 °C. (b) Under ambient humidity and room temperature condition. For both MEAs, the cathode catalyst loading was about $0.12 \text{ mg}\cdot\text{cm}^{-2}$. (c) Polarization curves from US Department of Energy's reference conditions with $0.12 \text{ mg}\cdot\text{cm}^{-2}$ and (d) $0.20 \text{ mg}\cdot\text{cm}^{-2}$ of cathode catalyst loading. Test at 80°C H_2/air in MEA; fully humidified with total outlet pressure of 150 kPa; an anode stoichiometry of 2; a cathode stoichiometry of 2 for air. The inset of each figure indicates the difference between the power densities of MEAs with a conventional electrode and an IO electrode.

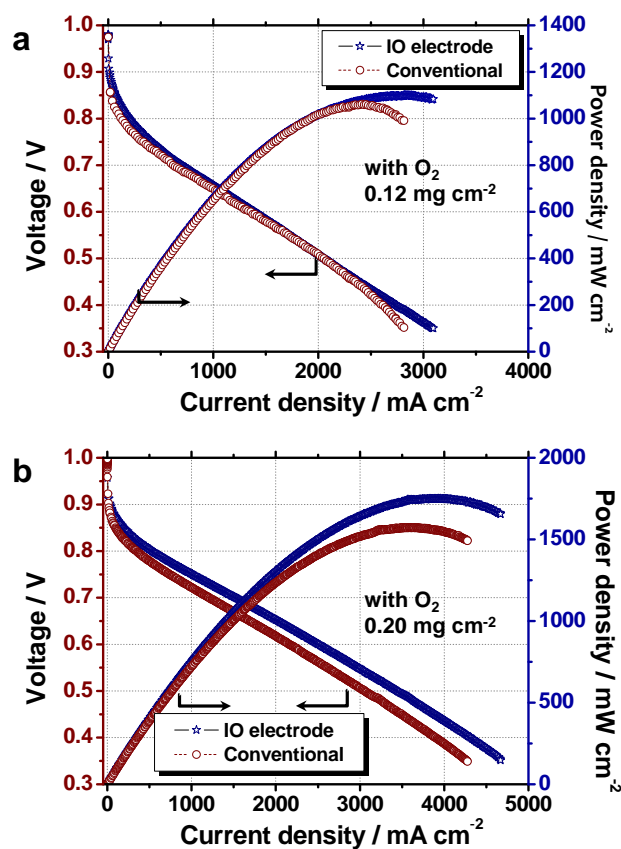


Figure 2.11 Polarization curves under oxygen. The cathode catalyst loading with (a) 0.12 mg cm⁻², and (b) 0.20 mg cm⁻². Test at US department of energy (DOE)'s reference conditions with 80°C H₂/O₂ in MEA; fully humidified with total outlet pressure of 150 KPa; an anode stoichiometry of 2; a cathode stoichiometry of 9.5.

higher maximum power density and has a common configuration with a lower catalyst loading (Fig. 2.10c). In contrast, when a thicker electrode is used, the differences become more pronounced (Fig. 2.10d). This is because concentration losses due to mass transport of reactants and products increase in a thicker electrode. Specifically, a thicker electrode imposes a greater distance that reactants must diffuse through in order to reach the catalyst layer where the reactions occur. Likewise, a thicker electrode requires that products must diffuse over a greater distance to be removed from the fuel cell. The inset of each figure in Fig. 2.10 undoubtedly shows that the difference between the power densities of the two MEAs is significant for voltages under 0.7 V, but once the latter value is reached, the unit cells experience deficient oxygen transfer in the MEAs. On the contrary, by inspection of the open-circuit voltage (OCV) to 0.7 V, the difference is not notable because those potentials are in the charge transfer-controlled region. Therefore, the PEMFC performances in the low-current region are nearly the same in both unit cells. However, the depletion of the reactant was reduced by their morphological advantages (*e.g.* easy access to relatively large surface areas, highly open, low-tortuosity structures, and interconnected macropores of the IO electrode), which resulted in a higher power density of the MEA containing the IO electrode in the high-current region.

The electrochemical surface area (ECSA) of the Pt catalyst was determined using hydrogen desorption areas from the cyclic voltammograms (Fig. 2.12), and then calculating the effects of factors such as Pt loading in the electrode, the amount of charge required for hydrogen desorption, and the charge required to oxidize a monolayer of H.⁵³ Our calculations determined that the ECSA of the IO-electrode-based MEA was $24.13 \text{ m}^2\cdot\text{g}^{-1}$. The geometric surface area (GSA) of the IO-electrode-based MEA was estimated to be $40.04 \text{ m}^2\cdot\text{g}^{-1}$, by taking into account the total number of 500 nm spheres in the inverse opal electrode, both inside and outside areas of the sphere, and the roughness factor of the sphere's surface. The ECSA of the conventional MEA, on the other hand, was $57.01 \text{ m}^2\cdot\text{g}^{-1}$. Furthermore, the particle sizes of the commercial Pt/C catalysts used in this work were in the range 2–4 nm, and the GSA of the commercial Pt/C catalyst was $93 \text{ m}^2\cdot\text{g}^{-1}$. The detail evaluation process is as follow⁵⁴:

1) Evaluation of surface ratio and Pt wall thickness:

To evaluate the width of Pt shell, we calculate the ratio between empty and full spaces inside inverse opal structure. It was assumed that the Pt atoms remain as hexagonal close packed structures (*hcp*) structure or face centered cubic (*fcc*) structure, APF (Atomic Packing Factor) 0.74, and $2.5 \text{ cm} \times 2.5 \text{ cm} \times 1.5 \text{ }\mu\text{m}$ sized IO electrode. The theoretical Pt mass in IO electrode

can be calculated as:

$$\text{Mass}_{\text{IO electrode}} = \text{Volume}_{\text{total}} \times (1 - \text{APF}) \times \rho_{\text{Pt}} \quad (1)$$

$$= \{2.5 \text{ cm} \cdot 2.5 \text{ cm} \cdot 1.5 \text{ } \mu\text{m} \times (1 - 0.74)\} \times 21.4 \text{ g cm}^{-3} \quad (2)$$

$$= 5.22 \text{ mg} \quad (3)$$

where, ρ is the density of Pt metal. Therefore if all the empty space between PS spheres filled with Pt, the amount of Pt deposited onto the GDL was about 0.83 mg cm^{-2} , but the actual amount of Pt was about 0.12 mg cm^{-2} , as determined using inductively coupled plasma (ICP) mass spectrometry. Thus the ratio between empty and full spaces inside inverse opal structure is about 14.36%. However, the calculated value of surface ratio, which based on grain volume, surface area, grain mass, mass in a bulk and total number of grain particles, was about 9.30% for 8 nm sized Pt grain particle in a 500 nm sized sphere. This supports the assumption that the Pt walls are at least monolayer or thicker; about 10~15 nm.

2) Determination of mass-specific, geometric and electrochemically active surface areas:

The mass-specific, geometric and electrochemically active surface areas for conventional Pt/C are calculated based on Pt nanoparticles size. The crystallite sizes of the Pt nanoparticles were estimated by Gaussian fitting of

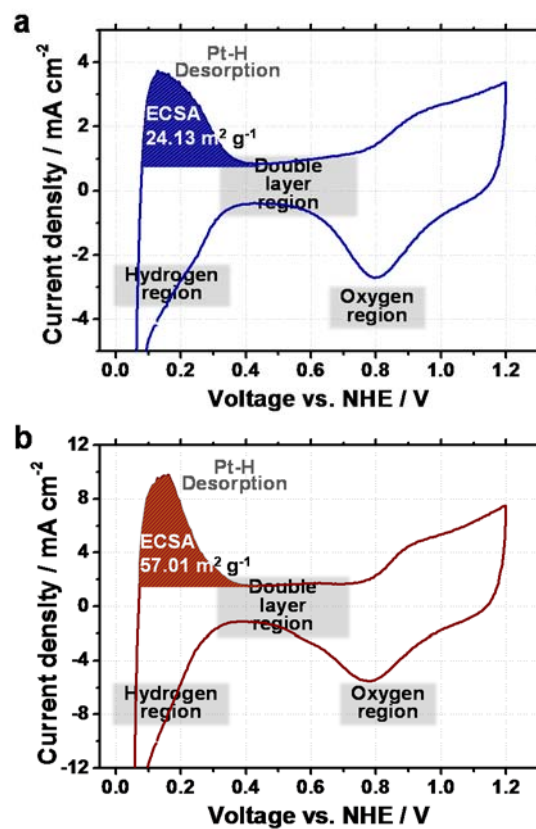


Figure 2.12 Cyclic voltammograms of electrodes. (a) IO electrode cathode, (b) conventional electrode cathode in the potential range of 0.05 –1.20 V, and the scan rate was 100 mV s⁻²

the Pt (220) peak using Scherrer's equation:

$$t = \frac{K \times \lambda}{B \times \cos \theta_B} \quad (4)$$

where, t is thickness of the crystallite, K is a constant that depends on shape (0.89), λ is wavelength of X-rays, B is fwhm of the peak, and θ_B is the Bragg angle. Therefore, the Pt crystallite sizes of 40 wt% Pt/C (Johnson Matthey Co.) was about 3.0 nm,⁵⁴ and 8.0 nm for the grain particles in IO electrode. Based on these parameters, the mass-specific, geometric surface area (GSA) and electrochemically active surface areas (ECSA) was calculated.

2.1) Conventional Pt/C electrode:

Mass-specific, geometric surface area (GSA) for the conventional Pt/C electrode was calculated based on the assumption of a spherical morphology and Pt crystallite sizes was about 3.0 nm.

- Mass-specific, geometric surface areas (geometric surface area; GSA):

$$A_{\text{JM Pt/C}} = \frac{6 \times 10^3}{\rho \cdot d} = \frac{6 \times 10^3}{(21.4 \text{ g cm}^{-3}) \cdot (3.00 \times 10^{-9} \text{ m})} = 93.46 \text{ m}^2 \text{ g}^{-1} \quad (5)$$

where, ρ is the density of Pt metal, and d is the diameter of the particle.

- Electrochemically active surface areas (electrochemical surface area; ECSA):

$$S_{\text{JM Pt/C}} = \frac{Q_H}{[\text{Pt}] \times 0.21} = \frac{0.00304 \text{ AV} / 100 \text{ mV s}^{-1}}{(0.12 \text{ mg cm}^{-2}) \cdot (5 \text{ cm}^2) \times 2.1 \text{ C m}^{-2}} = 57.01 \text{ m}^2 \text{ g}^{-1} \quad (6)$$

where [Pt] represents the platinum loading in the electrode, Q_H represents the amount of charge required for hydrogen desorption, and 0.21 represents the amount of charge required to oxidize a monolayer of H. To evaluate the value of Q_H , cyclic voltammetry (CV) with a potentiostat/galvanostat (IM-6, Zahner) was used.

2.2) Inverse opal structured electrode:

The GSA of the IO electrode was determined using a simple arithmetical calculation: to estimate the total number of PS beads in the electrode, the electrode area was divided by the diameter of a PS sphere (500 nm) and multiply about $\sqrt{3}/2$ times (15%), because of each sphere occupies hexagonal close packing, not square.

Then, the number of layers calculated based on the 1.5 μm thickness of the electrode was multiplied.

Additionally, we concluded that considering the effects of both inside and outside surfaces is reasonable, perhaps because the reactants could access both sides through the windows available in the sphere. Finally, we also took into account the roughness effect of the electrode surface. The GSA was calculated on the basis of the root-mean-square (RMS) surface roughness, which was determined using height data from at least three representative 100 nm \times 100 nm scan areas obtained by a roughness analysis program

included in the AFM analysis software. The average roughness (r_f , nm) of the electrode was estimated to be 6.65.

- The total number of PS beads in the electrode:

$$N_{\text{PS sphere}} = \text{Number of spheres per electrode area} \times \text{Layered number}$$

$$= \frac{5 \text{ cm}^2}{(500 \text{ nm})^2 \times \frac{\sqrt{3}}{2}} \times \frac{1.5 \text{ } \mu\text{m}}{500 \text{ nm}} = 6.90 \times 10^9 \text{ PS spheres} \quad (7)$$

- Therefore, the mass-specific, geometric surface area (GSA):

$$A_{\text{IO electrode}} = \frac{\text{The sum of the total surface area of PS spheres} \times 2 \text{ (both sides)} \times r_f}{\text{the total Pt mass}}$$

$$= \frac{\{(6.90 \times 10^9 \text{ PS spheres}) \times 4 \cdot \pi \cdot \left(\frac{500 \times 10^{-9} \text{ m}}{2}\right)^2\} \times 2 \times 6.65}{0.12 \text{ mg cm}^{-2} \times 5 \text{ cm}^2} = 40.04 \text{ m}^2 \text{ g}^{-1} \quad (8)$$

- Electrochemically active surface areas (electrochemical surface area; ECSA):

$$S_{\text{JM Pt/C}} = \frac{Q_H}{[\text{Pt}] \times 0.21} = \frac{0.007183 \text{ AV} / 100 \text{ mVs}^{-1}}{(0.12 \text{ mg cm}^{-2}) \cdot (5 \text{ cm}^2) \times 2.1 \text{ C m}^{-2}} = 24.13 \text{ m}^2 \text{ g}^{-1} \quad (9)$$

The different ratios of the ECSA to GSA; *i.e.* Pt utilization, for the catalysts are listed in Table 1. In general, the GSA increases with decreasing grain particle size, thus the GSA and ECSA for a conventional MEA were higher than those for the IO-electrode-based MEA. However, a higher ECSA does not always represent a better performance under actual fuel cell operating conditions. More importantly, the concept of GSA, ECSA, and Pt utilization in this study only accounts for hydrogen adsorption/desorption reactions related to catalytic capacity, but excludes overall process parameters such as

gas diffusion, ionic conduction path, proton conductivity, water and mass transfer in the MEAs; furthermore, any kinetic parameter was not included in the concept of Pt utilization as shown in Table 1. This suggests that the IO-electrode-based MEA could exhibit further improved performance even though its Pt utilization is nearly the same as that of conventional MEA. Additionally, the active sites that participated in oxygen reduction at the Pt surface were well distributed over the electrode than those in the conventional MEA; the relationship between morphology and performance of the MEA is thus confirmed by these experimental data.

Fuel cell losses are divided into three categories: activation, ohmic, and concentration losses (or mass transfer losses).²³ Although mass transfer loss occurs over the entire range of current density, it becomes prominent in the high limiting current region (lower-potential region). Accordingly, polarization in the high current density region represents mass transfer loss. The IO-electrode-based MEA exhibited better performance than the conventional MEA, especially in the high-current region, at ambient humidity, owing to the enhanced mass transfer in the IO-MEA, and better water management, as explained below.

In fuel cells, the effective porosity is more important than the total porosity. The effective porosity includes only the pore space that is interconnected and

Table 2.2 Structures and electrochemical properties of IO electrodes.

| Material | Pt grain particle size (nm) | GSA (m ² g ⁻¹) | Pt loading (mg cm ⁻²) | ECSA (m ² g ⁻¹) | Pt utilization (%) | Current density (mA cm ⁻²) | Maximum power density (mW cm ⁻²) |
|---------------------------|-----------------------------------|--|--------------------------------------|---|-----------------------|--|--|
| IO electrode | 8 ^a | 40 | 0.12 | 24 | 60 | 440 ^c | 320 ^c |
| | | | | | | 1056 ^d | 836 ^d |
| Conventional electrode | 3 ^b | 93 | 0.12 | 57 | 61 | 235 ^c | 269 ^c |
| | | | | | | 1035 ^d | 715 ^d |

^a Calculated using Scherrer equation from X-ray diffraction data (Fig. 2.6).

^b From reference 54.

^c From Fig. 2.10a; under cathode dead-end mode.

^d From Fig. 2.10c; under US Department of Energy's reference conditions.

opens to the surface, such as that in an inverse opal structure. Theoretically, $i = nFJ_{\text{diff}}$, where i is the fuel cell operating current and J_{diff} is the diffusional flux. The J_{diff} of the IO electrode is larger than that of the conventional MEA because of the IO electrode's increased effective porosity and decreased diffusion layer thickness (δ). Therefore, it is possible to simultaneously achieve improved fuel cell operating current density (i) and limited current density (i_L). In addition, enhanced mass transport may lead to superior water management. The effect of better water balance ability is clearly demonstrated under low-humidity conditions such as those shown in Fig. 2.10b, which are similar to conditions in a micro fuel cell. Hence, enhanced mass transfer and water management can be demonstrated by comparing the performances of the MEAs under conditions with and without further humidification. The water produced, which diffuses from cathode to anode, is driven by the water concentration gradient through the membrane (back diffusion). The water keeps the electrolyte sufficiently moist so that it retains its ionic conductivity. When water is deficient, better water management of the IO electrode more easily facilitates back diffusion, and prevents a reduced cell performance. In particular, under ambient humidity at room temperature, the current density measured at 0.6 V for a conventional MEA (in the high current density region) decreases rapidly from 666 to 367

$\text{mA}\cdot\text{cm}^{-2}$ (45% loss), whereas that for the IO-electrode-based MEA decreases from 790 to 495 $\text{mA}\cdot\text{cm}^{-2}$ (37% loss, Fig. 2.11b). These results demonstrate that the IO-electrode-based MEA has a superior water transport capability that results from its highly open and low-tortuous structure and short diffusion pathway.

Ordered meso-structured materials such as Pt or MoS_2 can improve both the activity and stability of the catalyst, but the enhancement of mass transfer has not yet been clearly demonstrated.^{56, 57} Since reactants and products are mainly transferred through macro-sized secondary pores, the mass transfer of MEA in a single cell is dominated by these secondary pores.⁵⁸ For that reason, IO electrodes with ordered macropore structures show better performance and more effective water management in practical fuel cell devices.

Further, the OCV of the IO electrode was 0.982 V, whereas that of the conventional MEA was 0.935 V under ambient humidity and room temperature conditions. This difference suggests that the mixed cathode potential for either the reactions between the Pt surface and O_2 , or from impurity oxidation⁵⁵ at the IO electrode, is lower than that for a conventional MEA. Thus, it is feasible to directly apply an inverse opal structure as an MEA electrode in PEMFCs. More importantly, the IO electrode has a much

lower Pt loading and its performance is significantly better than that of general direct methanol fuel cells under similar operating conditions, *e.g.* ambient humidity and heating. Thus, the IO electrode offers a promising MEA structure for use in micro fuel cell applications because the IO electrode fuel cell requires neither a complicated subsystem nor a balance of plant, unlike other fuel cell systems.

2.5 Conclusions

We have demonstrated an approach for the facile and direct application of a large-area (5 cm^2 of active area) IO Pt electrode in a practical MEA device, without any additional transfer process required at the electrodes. An unsophisticated pretreatment process was required to adjust the substrate to enable PS bead deposition onto the rough substrate surface. Owing to their open and interconnected pore architecture, the IO electrodes maintained a good effective porosity, effective catalyst utilization and mass transfer, and satisfactory water management, while the concentration loss was minimized. Further, we have reported the unique performance of a single cell that features an inverse opal structure entirely within an MEA. Furthermore, the inverse-opal structure Pt catalyst layer was free from carbon corrosion problems since the electrode was neither based on carbon materials nor on carbon-based supports. It is expected that improved performance can be achieved by decreasing the Pt particle size, and by optimizing the pore size. Moreover, with our approach, it is possible to vary both the colloidal size and species, and to use a non-precious metal alloy precursor. However, achieving high-performance PEMFCs with an IO electrode is not the only purpose of this study; discovering alternative, equally promising applications in electrochemical devices is another important purpose.

2.6 References

1. Hoffmann, P. *Tomorrow's Energy: Hydrogen, Fuel Cells, and the Prospects for a Cleaner Planet* (The MIT Press, 2012).
2. Steele, B. C. H. and Heinzel, A. Materials for fuel-cell technologies, *Nature* **414**, 345–352 (2001).
3. Perry, M. L. and Fuller, T. F.A. Historical perspective of fuel cell technology in the 20th century, *J. Electrochem. Soc.* **149**, S59–S67 (2002).
4. Borup, R. *et al.* Scientific aspects of polymer electrolyte fuel cell durability and degradation, *Chem. Rev.* **107**, 3904–3951 (2007).
5. Yoo, S. J. *et al.* Promotional effect of palladium on the hydrogen oxidation reaction at a PtPd alloy electrode, *Angew. Chem. Int. Ed.* **47**, 9307–9310 (2008).
6. Jung, N. *et al.* Preparation process for improving cathode electrode structure in direct methanol fuel cell, *Electrochem. Commun.* **12**, 754–757 (2010).
7. Cho, Y.-H. *et al.* Enhanced performance and improved interfacial properties of polymer electrolyte membrane fuel cells fabricated using sputter-deposited Pt thin layers, *Electrochim. Acta* **53**, 6111–6116

- (2008).
8. Therdthianwong, A., Ekdharmasuit, P. and Therdthianwong, S. Fabrication and performance of membrane electrode assembly prepared by a catalyst-coated membrane method: Effect of solvents used in a catalyst ink mixture, *Energy Fuels* **24**, 1191–1196 (2010).
 9. Fischer, A., Jindra, J. and Wendt, H. Porosity and catalyst utilization of thin layer cathodes in air operated PEM-fuel cells, *J. Appl. Electrochem.* **28**, 277–282 (1998).
 10. Suzuki, A. *et al.* Ionomer content in the catalyst layer of polymer electrolyte membrane fuel cell (PEMFC): Effects on diffusion and performance, *Int. J. Hydrogen Energy* **36**, 2221–2229 (2011).
 11. Chai, G. S., Shin, I. S. and Yu, J.-S. Synthesis of ordered, uniform, macroporous carbons with mesoporous walls templated by aggregates of polystyrene spheres and silica particles for use as catalyst supports in direct methanol fuel cells, *Adv. Mater.* **16**, 2057–2061 (2004).
 12. Miao, F. and Tao, B. Methanol and ethanol electrooxidation at 3D ordered silicon microchannel plates electrode modified with nickel–palladium nanoparticles in alkaline, *Electrochim. Acta* **56**, 6709–6714 (2011).
 13. Wang, C. *et al.* Proton exchange membrane fuel cells with carbon

- nanotube based electrodes, *Nano Lett.* **4**, 345–348 (2004).
14. Yuan, F.L. and Ryu, H. J. The synthesis, characterization, and performance of carbon nanotubes and carbon nanofibres with controlled size and morphology as a catalyst support material for a polymer electrolyte membrane fuel cell, *Nanotechnology* **15**, S596–S602 (2004).
 15. Michel, M. *et al.* High-Performance Nanostructured Membrane Electrode Assemblies for Fuel Cells Made by Layer-By-Layer Assembly of Carbon Nanocolloids, *Adv. Mater.* **19**, 3859–3864 (2007).
 16. Baughman, R. H., Zakhidov, A. A. and de Heer, W. A. Carbon nanotubes-the route toward applications, *Science* **297**, 787–792 (2002).
 17. Fang, B., Kim, J. H., Kim M. and Yu, J.-S. Fabrication of hollow core carbon spheres with hierarchical nanoarchitecture for ultrahigh electrical charge storage, *Chem. Mater.* **21**, 789–796 (2009)
 18. Jang, S.-E. and Kim, H. Effect of Water Electrolysis Catalysts on Carbon Corrosion in Polymer Electrolyte Membrane Fuel Cells, *J. Am. Chem. Soc.* **132**, 14700–14701 (2010).
 19. Litster, S. and McLean, G. PEM fuel cell electrodes, *J. Power Sources* **130**, 61–76 (2004).
 20. O’Hayre. R., Cha. S.-W., Colella, W. and Prinz, F. B. *Fuel Cell Fundamentals* (Wiley, New York, 2006)

21. Velev, O. D., Jede, T. A., Lobo, R. F. and Lenhoff, A. M. Porous silica via colloidal crystallization, *Nature* **389**, 447–448 (1997).
22. Jiang, P., Bertone, J. F. and Colvin, V. L. A lost-wax approach to monodisperse colloids and their crystals, *Science* **291**, 453–457 (2001).
23. Hatton, B., Mishchenko, L., Davis, S., Sandhage, K. H. and Aizenberg, J. Assembly of large-area, highly ordered, crack-free inverse opal films, *PANS*. **107**, 10354–10359 (2010).
24. Stein, A., Li, F. and Denny, N. R. Morphological control in colloidal crystal templating of inverse opals, hierarchical structures, and shaped particles, *Chem. Mater.* **20**, 649–666 (2008).
25. Kulinowski, K. M., Jiang, P., Vaswani, H. and Colvin, V. L. Porous metals from colloidal templates, *Adv. Mater.* **12**, 833–838 (2000).
26. Arpin, K. A. *et al.* Multidimensional Architectures for Functional Optical Devices, *Adv. Mater.* **22**, 1084–1101 (2010).
27. Kim, J.-H. *et al.* Ni–NiO core–shell inverse opal electrodes for supercapacitors, *Chem. Commun.* **47**, 5214–5216 (2011).
28. Sakamoto, J. S. and Dunn, B. Hierarchical battery electrodes based on inverted opal structures, *J. Mater. Chem.* **12**, 2859–2861 (2002).
29. Yan, H. *et al.* Colloidal-Crystal-Templated Synthesis of Ordered Macroporous Electrode Materials for Lithium Secondary Batteries, *J.*

- Electrochem. Soc.* **150**, A1102–A1107 (2003).
30. Su, F. *et al.* Synthesis of graphitic ordered macroporous carbon with a three-dimensional interconnected pore structure for electrochemical applications, *J. Phys. Chem. B* **109**, 20200–20206 (2005).
 31. Reculosa, S. *et al.* Carbon membranes of controlled thickness from colloidal crystals, *Adv. Mater.* **18**, 1705–1708 (2006).
 32. 32 Ergang, N. S. *et al.* Photonic crystal structures as a basis for a three-dimensionally interpenetrating electrochemical-cell system, *Adv. Mater.* **18**, 1750–1753 (2006).
 33. Lytle, J. C. and Stein, A. *Annual Reviews of Nano Research* (World Scientific Publishing Co., River Edge, NJ, 2006)
 34. Ruiz-Morales, J. C. *et al.* Microstructural optimisation of materials for SOFC applications using PMMA microspheres, *J. Mater. Chem.* **16**, 540–542 (2006).
 35. An, Y., Skinner, S. J. and McComb, D. W. Template-assisted fabrication of macroporous thin films for solid oxide fuel cells, *J. Mater. Chem.* **20**, 248–254 (2010).
 36. Umeda, G. A., Chueh, W. C., Noailles, L. Haile, S. M. and Dunn, B. S. Inverse opal ceria–zirconia: architectural engineering for heterogeneous catalysis, *Energy Environ. Sci.* **1**, 484–446 (2008).

37. Mihi, A., Zhang, C. and Braun, P. V. Transfer of preformed three-dimensional photonic crystals onto dye-sensitized solar cells, *Angew. Chem. Int. Ed.* **50**, 5712–5715 (2011).
38. Liu, Y., Chen, J., Misoska, V., Swiegers, G. F. and Wallace, G. G. Preparation of platinum inverse opals using self-assembled templates and their application in methanol oxidation, *Mater. Lett.* **61**, 2887–2890 (2007).
39. Du, Y., Lv, K., Su, B., Zhang, N. and Wang, C. Electro-reduction of oxygen and electro-oxidation of methanol at Pd monolayer-modified macroporous Pt electrode, *J. Appl. Electrochem.* **39**, 2409–2414 (2009).
40. Dimos, M. M. and Blanchard, G. J. Examining the electrocatalytic oxidation of selected diols at nanoporous and planar Pt electrodes, *J. Phys. Chem. C* **115**, 11247–11256 (2011).
41. Du, Y., Su, B., Zhang, N. and Wang, C. A novel preparation method of Sn-modified Pt nanoparticles and application for methanol oxidation, *Appl. Surf. Sci.* **255**, 2641–2645 (2008).
42. Munakata, H., Chiba, H. and Kanamura, K. Enhancement on proton conductivity of inorganic–organic composite electrolyte membrane by addition of sulfonic acid group, *Solid State Ionics* **176**, 2445–2450 (2005).

43. Yamamoto, D., Munakata, H. and Kanamura, K. Synthesis and characterization of composite membrane with three-dimensionally ordered macroporous polyimide matrix for DMFC, *J. electrochem. Soc.* **155**, B303–B308 (2008).
44. Lu, J., Lu, S. and Jiang, S. P. Highly ordered mesoporous Nafion membranes for fuel cells, *Chem. Commun.* **47**, 3216–3218 (2011).
45. Wu, G., Asai, S. and Sumita, M. Entropy penalty-induced self-assembly in carbon black or carbon fiber filled polymer blends, *Macromolecules* **35**, 945–951 (2002).
46. McCreery, R. L. Advanced carbon electrode materials for molecular electrochemistry, *Chem. Rev.* **108**, 2646–2687 (2008).
47. Jiang, P., Bertone, J. F., Hwang, K. S. and Colvin, V. L. Single-crystal colloidal multilayers of controlled thickness, *Chem. Mater.* **11**, 2132–2140 (1999).
48. Wijnhoven, J. and Vos, W. L. Preparation of photonic crystals made of air spheres in titania, *Science* **281**, 802–804 (1998).
49. Ko, Y. G. and Shin, D. H. Effects of liquid bridge between colloidal spheres and evaporation temperature on fabrication of colloidal multilayers, *J. Phys. Chem. B* **111**, 1545–1551 (2007).
50. Kim, H., Subramanian, N. P. and Popov, B. N. Preparation of PEM fuel

- cell electrodes using pulse electrodeposition, *J. Power Sources* **138**, 14–24 (2004).
51. Kim, K.-H. *et al.* The effects of Nafion[®] ionomer content in PEMFC MEAs prepared by a catalyst-coated membrane (CCM) spraying method, *Int. J. Hydrogen Energy* **35**, 2119–2126 (2010).
 52. Choi, J. W. *et al.* An experimental study on the purge characteristics of the cathodic dead-end mode PEMFC for the submarine or aerospace applications and performance improvement with the pulsation effects, *Int. J. Hydrogen Energy* **35**, 3698–378-11 (2010).
 53. You, D. J. *et al.* Carbon-supported ultra-high loading Pt nanoparticle catalyst by controlled overgrowth of Pt: Improvement of Pt utilization leads to enhanced direct methanol fuel cell performance, *Int. J. Hydrogen Energy* **37**, 6880–6885 (2012).
 54. Lim, J. W. *et al.* Ionic resistance of a cathode catalyst layer with various thicknesses by electrochemical impedance spectroscopy for PEMFC, *J. Electrochem. Soc.* **159**, B378–B384 (2012).
 55. Zhang, J., Tang, Y., Song, C., Zhang, J. and Wang, H. PEM fuel cell open circuit voltage (OCV) in the temperature range of 23 °C to 120 °C, *J. Power Sources* **163**, 532–537 (2006).
 56. Kibsgaard, J., Gorlin, Y., Chen, Z. and Jaramillo, T. F. Meso-Structured

- Platinum Thin Films: Active and Stable, *J. Am. Chem. Soc.* **134**, 7758–7765 (2012).
57. Kibsgaard, J., Chen, Z., Reinecke, B. N. and Jaramillo, T. F. Engineering the surface structure of MoS₂ to preferentially expose active edge sites for electrocatalysis, *Nature Mater.* **6**, 963–969 (2012).
58. Cho, Y.-H. *et al.* Improved mass transfer using a pore former in cathode catalyst layer in the direct methanol fuel cell, *Int. J. Hydrogen Energy* **37**, 11969–11974 (2012).

Chapter 3

Realistic Applications of Metal-Free Hybrid

Materials as Fuel Cells Electrodes: both Acidic and Alkaline Polymer Electrolytes

3.1 Abstract

Although numerous reports on nonprecious metal catalysts for replacing expensive Pt-based catalysts have been published, few of these studies have demonstrated their practical application in fuel cells. In this work, we report graphitic carbon nitride and carbon nanofiber hybrid materials synthesized by a facile and gram-scale method via liquid-based reactions, without the use of toxic materials or a high pressure-high temperature reactor, for use as fuel cell cathodes. The resulting materials exhibited remarkable methanol

tolerance, selectivity, and stability even without a metal dopant. Furthermore, these completely metal-free catalysts exhibited outstanding performance as cathode materials in an actual fuel cell device: a membrane electrode assembly with both acidic and alkaline polymer electrolytes. The fabrication method and remarkable performance of the single cell produced in this study represent progressive steps toward the realistic application of metal-free cathode electrocatalysts in fuel cells.

3.2 Introduction

Although the first fuel cells were fabricated in 1839 by William Grove, fuel cell-based technology has still not become fully commercialized. One of the main impediments to the commercialization of fuel cells is the use of expensive Pt catalysts. Significant effort has been devoted to replacing the expensive Pt-group metal (PGM)-based catalysts used in the oxygen reduction reaction (ORR) with inexpensive, more abundant nonprecious metal catalysts.¹ The progressive steps that have been taken in the development of ORR electrochemical catalysts can be summarized as follows: (1) Reduction of the size of Pt catalysts to nm scale, with a concomitant increase in their surface area and efficiency; (2) fabrication of Pt-based alloys or core-shell structures for enhanced activity and stability; (3) replacement of Pt-based catalysts with cheaper and non-PGM compounds such as those based on Fe or Co; and (4) implementation of metal-free materials such as N-doped carbon.^{2,3}

Currently, the most promising candidates are transition metal–nitrogen materials, despite the drawbacks associated with their cost, activity, and stability. Moreover, controversy has surrounded the role of metals in ORR catalysts.⁴⁻⁷ Alternatively, the intrinsic catalytic properties of nonmetallic N-doped carbon materials, such as N-carbon nanotubes (N-CNTs), N-graphene,

and graphitic carbon nitride (g-C₃N₄), have also attracted interest. However, the ORR mechanisms and associated active sites of such materials (e.g., pyridinic N, pyrrolic N, and graphitic N) are still under debate.⁸⁻¹⁰

Recently, g-C₃N₄ has proven to be effective as a multifunctional catalyst in various applications.¹¹⁻¹⁴ In particular, its ORR catalytic activity is considered to be significant for clean energy conversion and storage applications. g-C₃N₄ has numerous advantages compared with traditional Pt catalysts, including (1) relatively lower costs and greater abundance, (2) increased stability toward CO poisoning, (3) greater methanol tolerance, and (4) the possibility of obtaining a variety of nanostructures via a templating method. In addition, g-C₃N₄ has a higher nitrogen content and more active reaction sites compared to other N-carbon materials, resulting in better performance as a practical metal-free ORR electrocatalyst.^{8,11-14} Various methods have been developed for the synthesis of g-C₃N₄. A solid-state reaction at high pressure and temperature and a poly-condensation reaction of liquid precursors such as cyanamide are the traditional methods used to synthesize bulk g-C₃N₄. However, the bulk-phase reaction has been demonstrated to be prone to incomplete condensation of the precursors,¹¹ and cyanamide is not only expensive but also highly explosive and toxic.¹⁴ Consequently, although some of g-C₃N₄-type catalysts are still being

proposed, their use is not practical.

Herein, we report the facile and gram-scale production of a g-C₃N₄ hybrid material (denoted hereafter as g-CN) via a liquid-based reaction without the use of cyanamide or a high-pressure/high-temperature reactor. The resulting composite material prepared using a metal-free procedure exhibited a fuel cell cathode catalytic activity competitive with that of a commercial Pt/C catalyst. Furthermore, as illustrated in Fig. 3.1, g-CN exhibited outstanding performance in membrane electrode assemblies (MEAs) of polymer electrolyte membrane fuel cells (PEMFCs, in which protons are the conducting species) and anion exchange membrane fuel cells (AEMFCs, in which hydroxide ions are the conducting species).

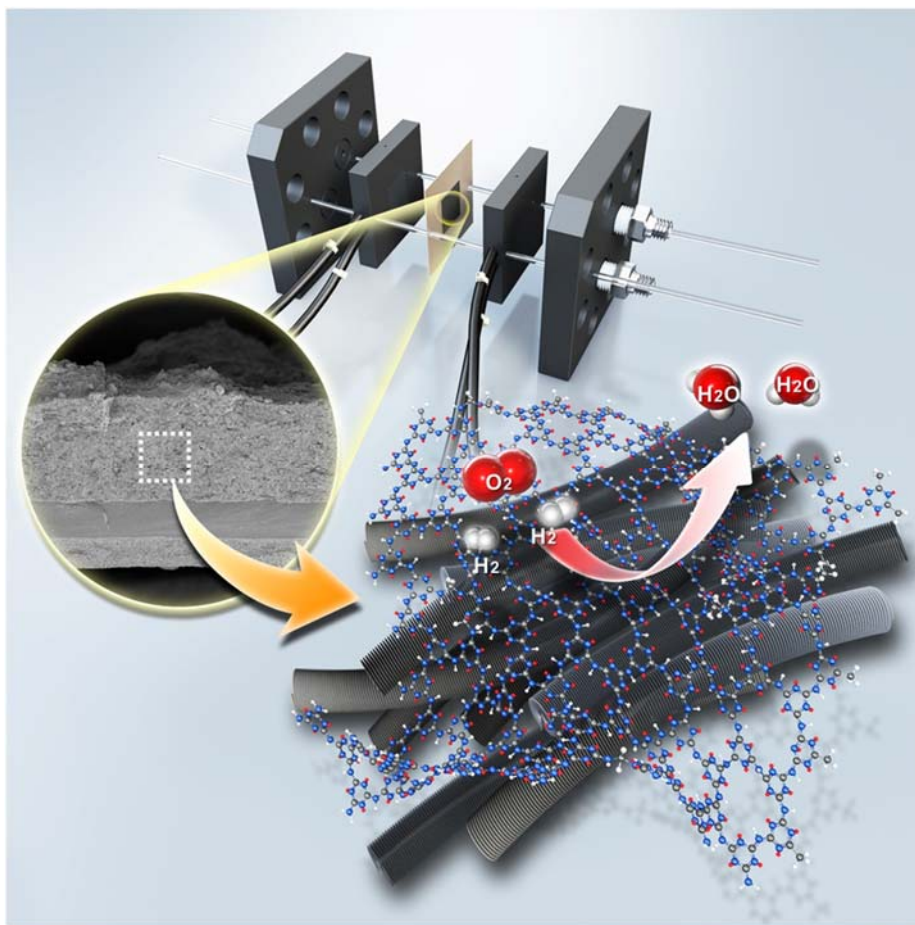


Figure 3.1 Conceptual diagrams of the g-CN-CNF-based MEA and the single cell. The inset shows a cross-section Fe-SEM image of the g-CN-based MEA.

3.3 Experimental Section

Materials and Characterization

Commercially available solvents and reagents were used without further purification unless otherwise noted. The carbon nanofiber (CNF) was purchased from (Carbon Nanomaterial Technology Co., Gyongju, Republic of Korea). Both the ^{13}C and the ^{15}N solid-state NMR spectra were recorded on Bruker Avance II instruments using a cross-polarization (CP) magic-angle-spinning (MAS) sequence mode. The samples were loaded into 4 mm ZrO_2 rotors and spun at 11 kHz (5 kHz for ^{15}N) with a pulse delay of 5 s and a contact time of 5 ms (3 ms for ^{15}N). The data were referenced to trimethylsilane and ammonium chloride. In the spectra, resonances from the amino groups were barely observed because the NH signals were attenuated by the long polarization inversion time.^[8a] The morphology of the synthesized catalysts was characterized by high-resolution transmission electron microscopy (HR-TEM; JEOL 2010) and field-emission scanning electron microscopy (FE-SEM; Carl Zeiss, SUPRA 55 VP). The UV-visible and PL spectra were measured on a Scinco 2100 spectrophotometer and a Jasco FP-750 spectrofluorometer, respectively. X-ray diffraction (XRD) analyses of the prepared catalysts were carried out on an X-ray

diffractometer (Rigaku D/MAX 2500) equipped with a Cu-K α radiation source operated at 40 kV and 100 mA. The samples were scanned from 20° to 80° with a scanning rate of 2° min⁻¹. X-ray photoelectron spectra (XPS) were obtained using an Al-K α source (ESCALAB 250 XPS spectrometer, VG Scientifics). The binding energies were calibrated with respect to the C (1s) peak at 285 eV, and the experimental data were curve-fitted using the AVANTAGE 4.19 software package. The nitrogen content was determined using a CHN elemental analyzer (LECO Corp., US/CHNS-932). A thermogravimetric analyzer (TAC 7/DX) was used to analyze the thermal stability and evolved gases.

Preparation of g-CN and g-CN-CNF

Melamine (1 eq.) was suspended in DMF and subsequently added to *N,N*-diisopropylethylamine. A solution of cyanuric chloride (1 eq.) in DMF was then added dropwise with stirring at 0°C in an ice-bath. After 1 h, the reaction temperature was increased to room temperature and the solution was stirred for an additional 5 h. The temperature was then decreased back to 0°C, and the solution of cyanuric chloride (1 eq.) in DMF was again added dropwise. After 1 h, the reaction temperature was increased to room temperature and the solution was stirred for an additional 5 h. Finally, the

system was refluxed for 12 h under nitrogen, after which the flask was cooled to room temperature and the yellow-colored precipitate was collected by filtration. The product was washed with water and ethanol twice, and then dried under vacuum at 100 °C. For g-CN-CNF, conducting materials such as CNF in DMF were added dropwise to the mixture prior to the reflux step. The mass ratio of the support carbon material CNF and g-CN was adjusted by approximately 70 wt%. For pyrolysis, g-CN-CNF was heated to the target temperature under Ar at a ramp rate of 100 °C h⁻¹ and was maintained at the target temperature for 30 min. For g-CN-CNF-Fe-700, iron (III) chloride (Sigma Aldrich, reagent grade, 97%) was added with stirring to a solution of g-CN intermediate solution before the last condensation step. The amount of the Fe precursor was adjusted by 1.8 and 3.6 wt% of g-CN and CNF. The mixture was stirred at room temperature for 2 h and CNF in DMF were added dropwise to the mixture prior to reflux. Finally the system was refluxed for 12 h under nitrogen. The flask was then cooled to room temperature, and the black-colored precipitate was filtered. The product was washed with excess water and ethanol three times and dried under vacuum at 100 °C. For pyrolysis, g-CN-CNF-Fe was heated to the target temperature under Ar at a ramp rate of 100 °C h⁻¹ and kept at the 700°C for 30 min (Fig. 3.2).

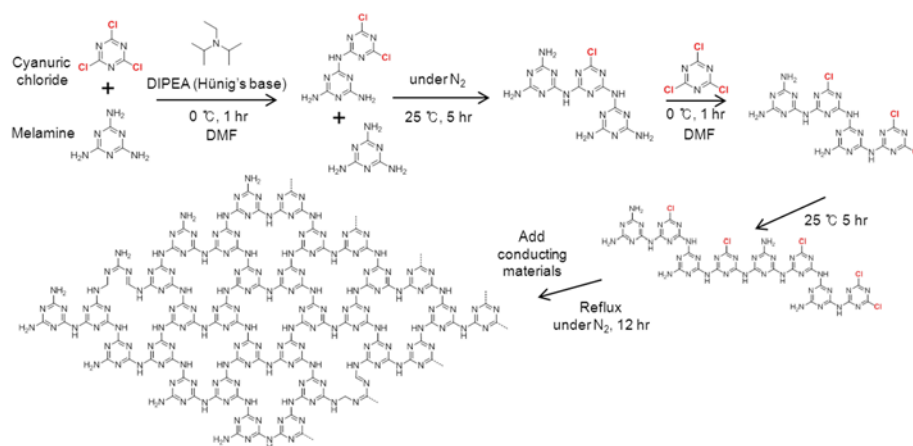


Figure 3.2 Condensation reactions of melamine and cyanuric chloride to produce extended networks of g-CN.

Electrochemical characterization

The electrochemical measurements were carried out using an Autolab general-purpose electrochemical system (Eco Chemie). Glassy carbon electrodes (0.196 cm²) were coated with catalyst inks for use as the working electrode, and Pt wire and Ag/AgCl electrodes were used as the counter and reference electrodes, respectively. All of the potentials are quoted with respect to a reversible hydrogen electrode (RHE) through the hydrogen oxidation reaction. The ORR activities and methanol tolerances of the catalysts were measured using an RDE in 0.1 M KOH and 0.5 M CH₃OH saturated with oxygen gas at 293 K. LSV was performed from 1.0 V to 0.1 V vs. a reference hydrogen electrode at a scan rate of 5 mV s⁻¹ and a rotation rate from 400 rpm to 1600 rpm. The ORR activities under acidic media were measured in a 0.1 M HClO₄ solution using the same method. The non-noble electrocatalyst was loaded at 98.4 µg (Pt loading was 28 µg, commercial E-TEK 20 wt%). The Koutecky-Levich plots were obtained by a linear fitting of the reciprocal rotating speed plotted as a function of the reciprocal current density collected at -0.6 V. The electron transfer numbers involved in the typical ORR process were calculated from the slope of the Koutecky-Levich equation:

$$B=0.2 \text{ nFA}\nu^{-1/6}C_{O_2}D_{O_2}^{2/3},$$

where n is the number of electrons transferred per oxygen molecule, F is the Faraday constant (96485 C mol^{-1}), D_{O_2} is the diffusion coefficient of O_2 in 0.1 M KOH ($1.9 \times 10^{-5} \text{ cm}^2 \text{ s}^{-1}$), ν is the kinetic viscosity, and C_{O_2} is the concentration of O_2 ($1.2 \times 10^{-3} \text{ mol L}^{-1}$). The constant 0.2 is used when the rotating speed is expressed in units of rpm. The calculated electron transfer numbers are listed in the inset of Fig. S7b. The ADT was conducted according to the DOE protocol in the potential window from 0.6 V to 1.0 V (RHE) under Ar using a scan rate of 20 mV s^{-1} .

MEA fabrication and single-cell test

1) PEMFCs: The typical MEA fabrication procedure has been described in detail elsewhere.²⁹ Briefly, a Nafion[®] 212 membrane (DuPont) was used as the ion-conducting membrane, which was immersed in a 2.5% H_2O_2 solution at 80°C for 1 h and then rinsed in boiling deionized water for another 1 h for purification. The membrane was then boiled in a 0.5 M H_2SO_4 solution for 1 h and rinsed again in deionized water for protonation. The g-CN-CNF-700 and a 40 wt% Pt/C commercial catalyst (Johnson Matthey Co.) were used as the cathode and anode catalysts, respectively. The Pt/C catalyst was dispersed in a mixture of isopropyl alcohol, deionized water, and perfluorosulfonic acid ionomer (Aldrich, 5 wt% Nafion[®] ionomer) to prepare

the catalyst ink. The ink was ultrasonicated for 10 min and sprayed onto both sides of a Nafion[®] 212 membrane. The volumes of the catalyst inks were carefully controlled so that they could be deposited with loadings of 0.2 mg cm⁻² and 5.0 mg cm⁻² for the anode and cathode, respectively. For comparison, a reference electrode composed of 40 wt% Pt/C (Johnson Matthey Co.) was used as the anode catalyst with a loading of 0.2 mg cm⁻² and as the cathode catalyst with a loading of 0.1 mg cm⁻². Carbon paper containing microporous layers (MPLs; 35BC, SGL) was used as a gas diffusion layer (GDL); it was placed on both the cathode and anode sides of the membrane. The MEAs were inserted into a single-cell unit containing a graphite plate with a serpentine gas flow channel (5 cm² area). A single-cell unit was assembled with eight screws tightened with a torque of 7.5 N·m. Activation and polarization tests of the assembled single cells (CNL-PEM005-01, CNL Energy) were carried out using the current sweep-hold method with a fuel cell test system (CNL Energy). The current density was swept at rate of 10 mA cm⁻² s⁻¹ and was maintained for 10 min after each of the following values was obtained: 0.5, 1.0, 1.5, 2.0, 2.5, 3.0, and 4.0 A cm⁻². During activation, the current was reset to zero when the cell voltage reached 0.30 V. Polarization curves were measured by the current-sweep method using the PEMFC test system. The test was conducted using fully humidified

H₂/O₂, which were supplied to the anode and cathode, respectively, during the activation and polarization tests. The total outlet pressure was 150 kPa with an anode stoichiometry of 2 and a cathode stoichiometry of 9.5. The cell temperature was maintained at 80 °C during activation and at room temperature during the polarization test. *In situ* electrochemical impedance spectra of single cells were obtained under faradaic conditions after the polarization tests. The cell voltages used in the EIS measurements were 0.4, 0.6, and 0.8 V with a 10 mV amplitude; measurements were performed over the frequency range of 100 kHz–100 MHz using a potentiostat/galvanostat (IM-6, Zahner)

2) AEMFCs: An anion exchange membrane was purchased from an anonymous company (details are withheld because of the company's material transfer agreement). The g-CN-CNF-700 and 40 wt% Pt/C (Johnson Matthey Co.) were used as the cathode and anode catalysts, respectively. The catalyst was dispersed in a mixture of isopropyl alcohol, deionized water, and anion exchange polymer (AS-4 ionomer, Tokuyama Co., Japan) to prepare the catalyst ink. The latter was stirred and ultrasonicated for 30 min and then sprayed onto the anion exchange membrane. The volume of anode catalyst ink was controlled such that it was deposited at 0.5 mg cm⁻², and the loadings of the cathode g-CN-CNF-700 and Pt/C catalysts were 2 mg cm⁻²

and 0.1 mg cm^{-2} , respectively. Carbon paper containing MPLs (35BC, SGL) was used as GDL, which was placed on both the cathode and anode sides of the membrane. The MEAs were inserted into the single-cell unit with a graphite plate containing a serpentine gas flow channel (5 cm^2 area). A single-cell unit was assembled with eight screws, using a tightening torque of $8 \text{ N}\cdot\text{m}$. The polarization curves were measured by the current-sweep method with the fuel cell test system (CNL Energy). The test was conducted using fully humidified H_2/O_2 , which were supplied to the anode and cathode, respectively. The total outlet pressure was 150 kPa with an anode stoichiometry of 2 and cathode stoichiometry of 9.5 for O_2 . The cell temperature was maintained at $50 \text{ }^\circ\text{C}$ during the polarization tests..

3.4 Results and Discussion

Fabrication of g-CN and g-CN-CNFs

A schematic illustration of the g-CN and photographs of the bulk g-CN and g-CN with carbon nanofibers (CNFs) are presented in Figs. 3.3a and 3.3b, respectively. The g-CN was synthesized from melamine and cyanuric chloride, which are nitrogen-rich materials. Melamine is commonly used in industrial applications such as fireproofing materials and melamine resin. Additionally, melamine was recently used as a nitrogen precursor for the preparation of N-doped carbon materials.¹⁵⁻¹⁷ Cyanuric chloride is an important starting material for the synthesis of dendrimers,^{18,19} in which an iterative substitution reaction of cyanuric chloride and an amine group is induced via the sequential addition of amines and under controlled temperature. Tetrahydrofuran is commonly used as a solvent for the substitution reaction of cyanuric chloride. However, *N,N*-dimethylmethanamide was used as a solvent in this study because of its high boiling point.

During the stepwise synthesis, melamine and cyanuric chloride produced the g-CN structure. Such a condensation reaction is possible because of the

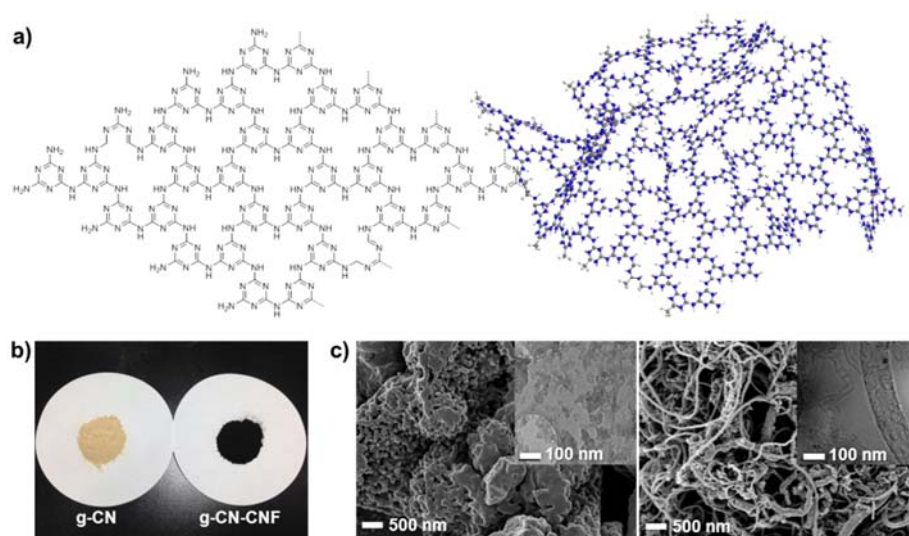


Figure 3.3 Structure and image of g-CN and g-CN-CNF. a) Chemical structure and schematic diagram of g-CN; b) photograph of g-CN and g-CN-CNF; and c) FE-SEM images of g-CN (left) and g-CN-CNF (right) (insets: TEM images).

different reactivities of trichlorotriazines and cyanuric chloride. At low temperature (i.e., 0°C), only one site of triazine can be substituted, whereas two sites can participate in substitution reactions that occur at room temperature (25°C), and all three sites can react under elevated temperatures (greater than 70°C). *N,N*-Diisopropylethylamine (Hünig's base) was used as a non-nucleophilic base for the substitution reaction because its molecular structure makes it ideal for this application. Specifically, the proton attached to the nitrogen atom is shielded by steric hindrance, which makes Hünig's base a good base but a poor nucleophile. In the last condensation step, CNF was added as a conducting carbon material to increase the electrical conductivity. CNF as a support material can easily form secondary, interconnected pores between the catalyst agglomerates in an MEA, where the pores range in size from approximately 200 nm to 1 µm (Figs. 3.4, 3.5). Therefore, CNF can facilitate mass transfer within the thick catalyst layer. The chemical reaction in the electrode of a PEMFC has been reported to occur primarily in the secondary pores rather than in the primary pores.²⁰ Prior to use, CNF was treated with acid (H₂SO₄:HNO₃ = 3:1 vol. %) for 7 h at 90°C to remove trace metal residues; the resulting sample is denoted as g-CN-CNF. A g-CN sample containing the intermediates was characterized by ¹³C and ¹⁵N solid-state cross polarization-magic angle spinning (CP-MAS)

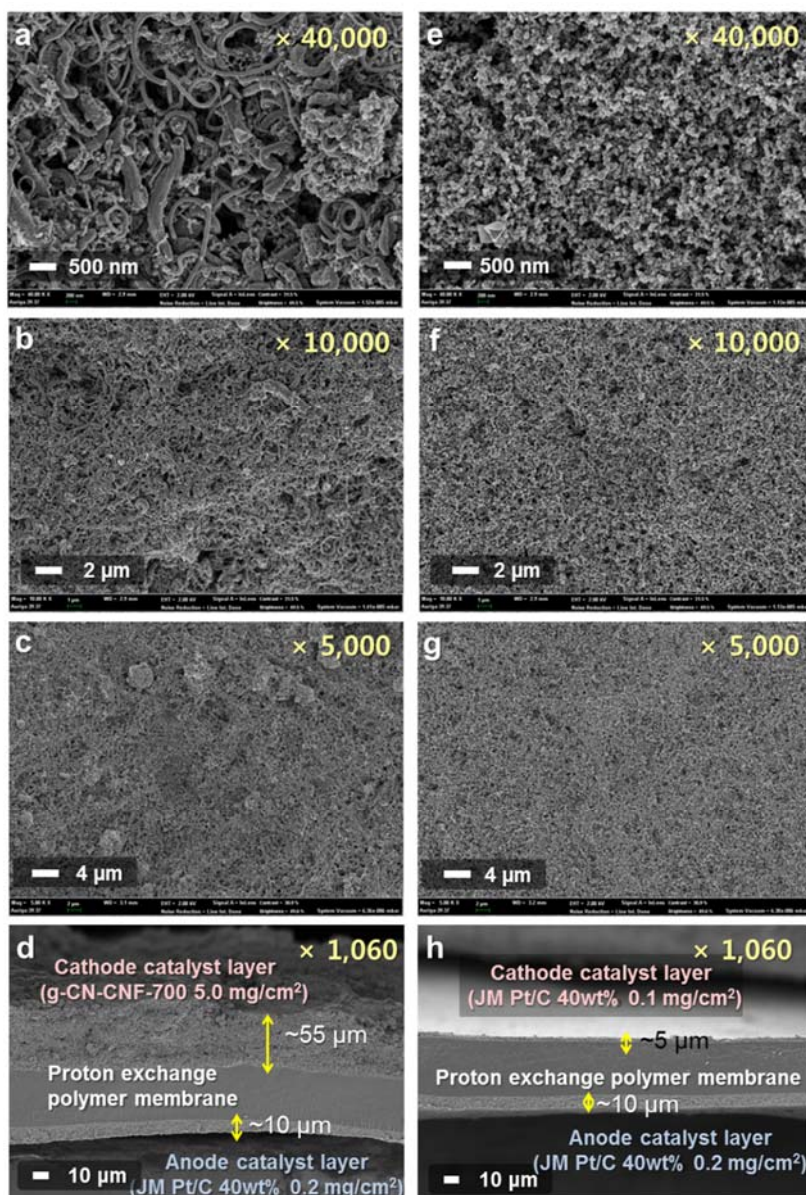


Figure 3.4 FE-SEM images of g-CN-CNF and commercial Pt/C-based MEA in PEMFCs. a-c) Surfaces and d) cross sectional images of g-CN-CNF-700-based MEA; e-g) surfaces and h) cross-sectional images of commercial Pt/C catalyst layers in PEMFCs.

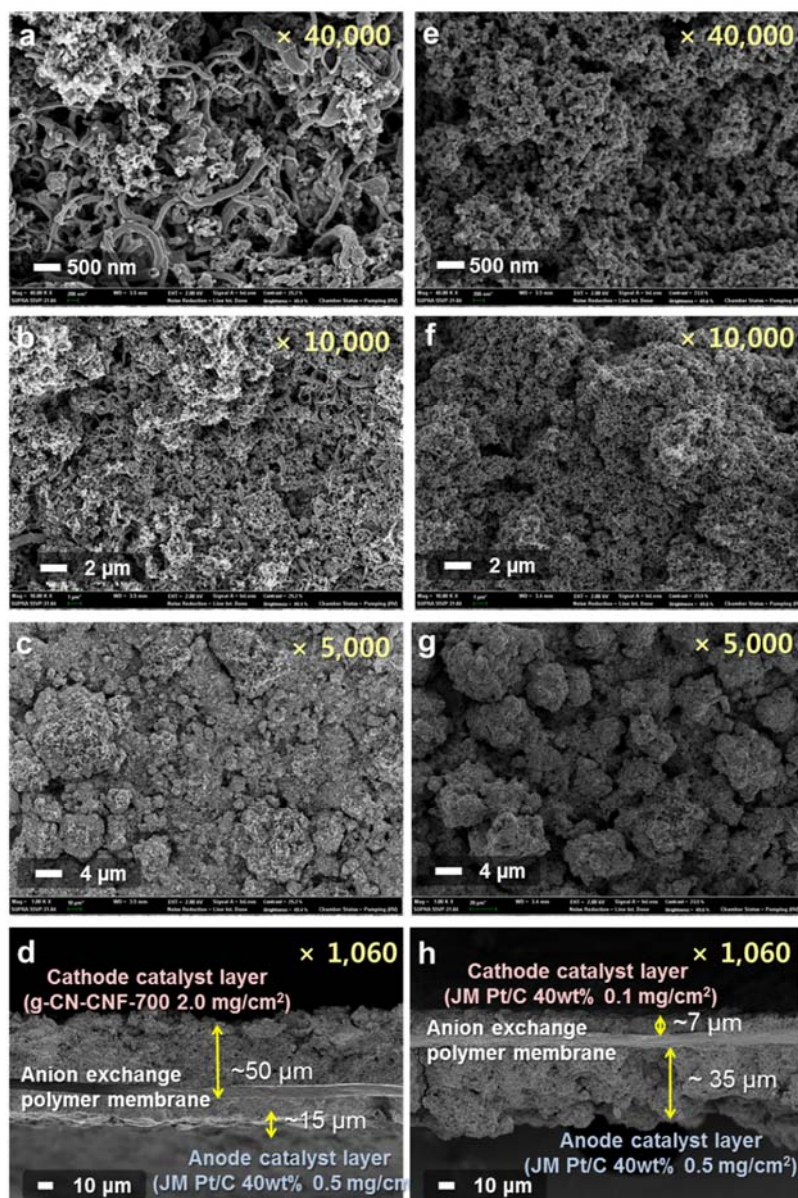


Figure 3.5 FE-SEM images of g-CN-CNF and commercial Pt/C-based MEA in AEMFCs. a-c) Surfaces and d) cross-sectional images of g-CN-CNF-based MEA in PEMFCs; e-g) surfaces and d) cross-sectional images of commercial Pt/C-based MEA in AEMFCs.

NMR, X-ray diffraction (XRD), FT-IR spectroscopy, photoluminescence (PL) spectroscopy, and X-ray photoelectron spectroscopy (XPS); the details of these characterizations are provided in the Supporting Information.

The ^{13}C and ^{15}N solid-state CP-MAS NMR spectra of g-CN are shown in Figs. 3a and 3b, respectively. Despite the fact that the g-CN in this study was not synthesized by a traditional method such as the condensation of precursors in the bulk phase under high pressure and high temperature used in the synthesis of poly(triazine), the NMR spectra were similar for the products synthesized using the two methods.¹⁸⁻¹⁹ The ^{13}C NMR spectrum of g-CN (Fig. 3.6a) shows two peaks at 161.0 ppm and 168.6 ppm. These chemical shifts are in agreement with those for sp^2 -hybridized carbon environments. In addition, the ^{15}N NMR data show a broad resonance signal between -185 ppm and -205 ppm, corresponding to the ring N atoms of g-CN. These values are typical for tertiary nitrogen atoms of triazine rings (Fig. 3.6b).

Furthermore, for the absorption and PL spectra (Fig. 3.6c and 3.6d), the conventional carbon nitride shows the typical absorption pattern of an organic semiconductor with a strongly expressed band gap adsorption at about 420 nm, and this is in good accord with the g-CN materials in absorption spectrum (Fig. 3.6c). And peaks centered around 420–430 nm

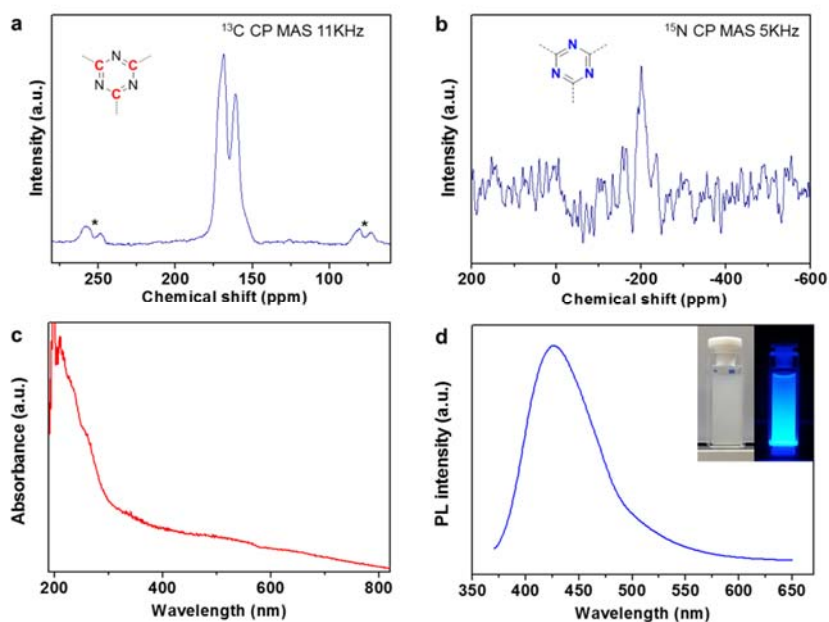


Figure 3.6 Physical characterization of g-CN. a) ^{13}C CP-MAS NMR spectrum of g-CN (spinning side-bands are denoted with asterisks); b) ^{15}N CP-MAS NMR spectrum of g-CN; c) absorption spectrum and d) photoluminescence spectrum (inset) of G-CN under 350 nm excitation at 298 K. The insets are photographs g-CN in ethanol under natural light (left) and under UV irradiation at 365 nm (right).

were found in PL spectrum (Fig. 3.6d). The origin of this blue emission of g-CN under 350 nm excitation at 298 K attributed to the band-edge transition or the exciton combination. This is consistent with its pale yellow color, as previously reported.¹²

Additionally, in the FT-IR spectrum (Fig. 3.7a), the linkage of the triazine ring systems was confirmed by the appearance of major peaks in the 1200–1600 cm^{-1} region, which correspond to $\text{sp}^2\text{C-N}$ and $\text{sp}^2\text{C=N}$. The absorption band at approximately 3100 cm^{-1} is attributed to the N-H stretching modes. In addition, the XRD pattern (Fig. 3.7b) and TGA trace (Fig. 3.8) of g-CN closely agree with those of other carbon nitride materials obtained by traditional synthesis methods.²¹⁻²³ XRD patterns of g-CN (Fig. 3.7b) representing the graphitic structure with an inter-planar stacking distance of 0.327 nm. The XRD pattern of the CNF and g-CN-CNF peak is added for comparison. The strongest peak of g-CN at 27.26° is a characteristic inter-planar stacking peak of aromatic systems, indexed for graphitic-like layer structure materials as the (002) peak. A slight broadening peak of the g-CN-CNF were detected at around 11.25° , corresponding to a distance of 0.795 nm and indexed as (100), assigned to an interplanar distance between nitride pores. TGA weight loss curve of g-CN and g-CN-CNF measured in N_2 with rate of 5°C/min (Fig. 3.8). During the pyrolysis step, almost all of g-CN

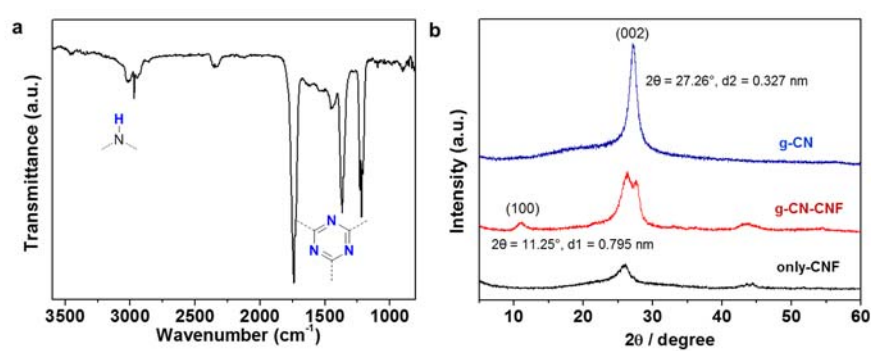


Figure 3.7 FT-IR spectrum and XRD pattern of g-CN materials. a) FT-IR spectrum of g-CN, b) XRD pattern of g-CN materials.

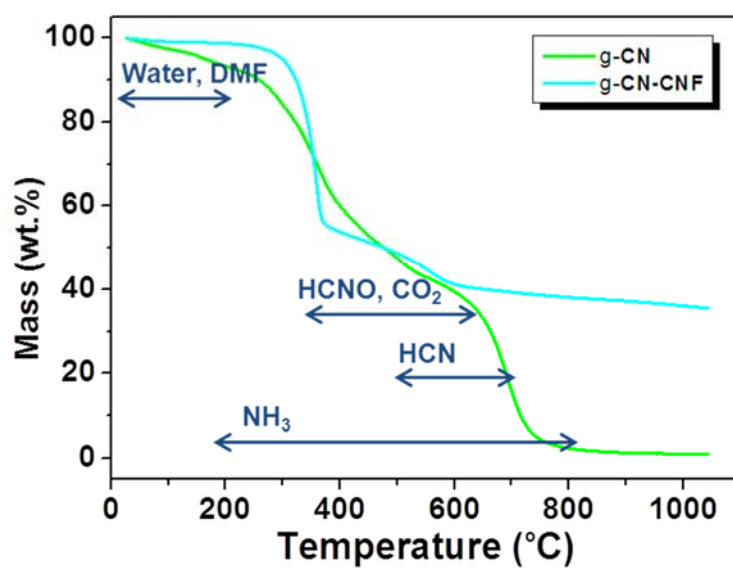


Figure 3.8 TGA weight loss curve of g-CN and g-CN-CNF: measured in N_2 with rate of $5\text{ }^\circ\text{C}/\text{min}$.

thermally decomposed above 750 °C. Pristine g-CN showed a 100% weight loss after 750 °C while carbon showed no obvious weight loss, indicating no carbon contamination in carbon nitride. The TGA curves are still similar to that of a polymeric carbon nitride like g-C₃N₄.

Electrochemical activity of g-CN and g-CN-CNFs

The electrocatalytic activity of g-CN toward the ORR was evaluated by cyclic voltammetry (CV) (Fig. 3.9) and linear sweep voltammetry (LSV) (Fig. 3.10a). Compared with g-CN, g-CN-CNF, and the other samples with heat-treatment, the g-CN-CNF-700 catalyst revealed the most obvious ORR peak with a larger cathodic current, indicating a better electrocatalytic performance for ORR. Notably, the inherent ORR activity on pure g-CN is negligible. Therefore, a heat treatment was performed to increase this material's ORR activity. Although the literature generally agrees that pyrolysis beneficially affects both the activity and stability of non-Pt-based electrocatalysts, controversy remains over what aspect of the heat treatment is responsible for the positive effects.²⁴ Specifically, the enhanced ORR activity and stability is attributed to follow reasons: 1) catalyzing the formation of a special type of carbon, which is actually the active phase such as graphitic nitrogen and/or pyridinic nitrogen functional groups, 2)

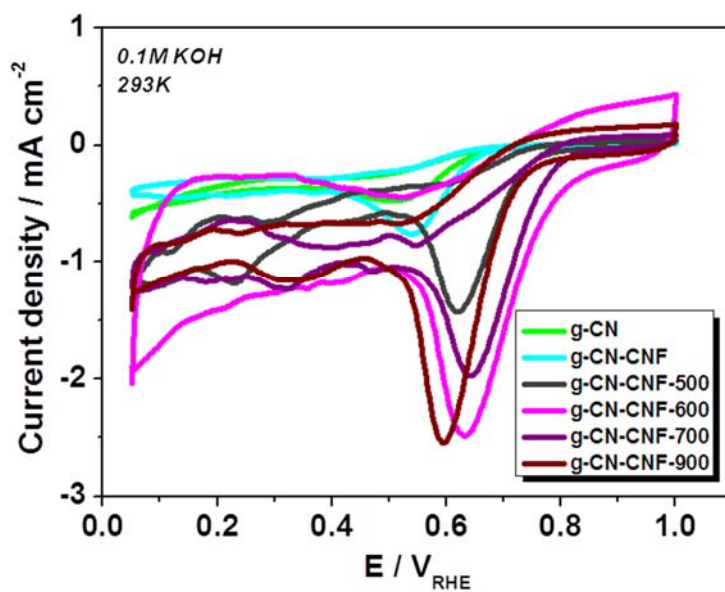


Figure 3.9 Cyclic voltammetry of g-CN materials: performed for g-CN and g-CN-CNF-500/600/700/900 in O_2 and N_2 in a 0.1 M KOH aqueous solution at room temperature.

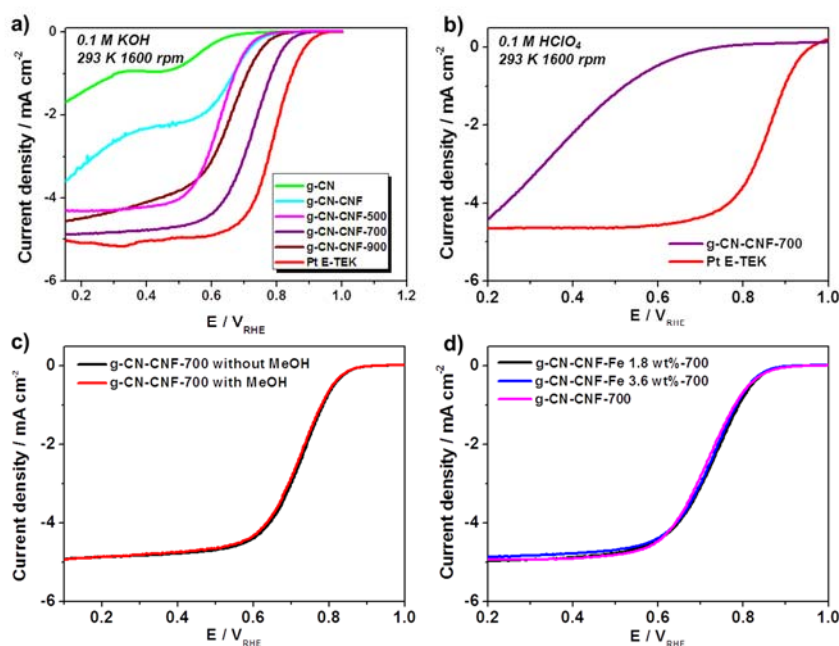


Figure 3.10 Electrochemical characterization of g-CN-CNF. a) Linear sweep voltammograms (LSVs) on RDE at 1600 rpm under 293 K of a) g-CN-CNF pyrolyzed at various temperature in O_2 saturated 0.1 M KOH solution, b) g-CN-CNF-700 in O_2 saturated 0.1 M $HClO_4$ solution. c) g-CN-CNF-700 with/without methanol, d) g-CN-CNF-700 with/without metal.

increasing the degree of edge plane exposure the latter represents, 3) improving the dispersion of the supported material, 4) final carbon structure and moiety change such as increasing hydrophilicity and generation of micropores on the surface. The objective of this study, however, was not to investigate the precise mechanism of pyrolysis, but rather to develop high-performance catalyst materials using a facile synthesis method. Therefore, the ORR activity was measured without further probes into the role of pyrolysis.

The onset potential, which typically reflects the activity of the electrocatalyst, increased steadily as the temperature was increased to 700°C. However, the onset potential decreased at temperatures greater than 700 °C because of a lack of active sites on g-CN, as indicated by the low nitrogen content of g-CN-CNF-900 (approximately 0.81 wt%) measured using an elemental analyzer (Table S1). Compared to g-CN, g-CN-CNF, and other samples treated by pyrolysis (denoted as g-CN-CNF-yyy, where yyy is the heat treatment temperature), the g-CN-CNF-700 catalyst exhibited the best electrocatalytic performance in 0.1 M KOH. The electron transfer number n of g-CN-CNF-700 was 3.46 according to the measured Koutecky–Levich plots (Fig. 3.11). Based on these plots, the electrocatalytic ORR mechanisms and dominated processes were further investigated. All plots show good

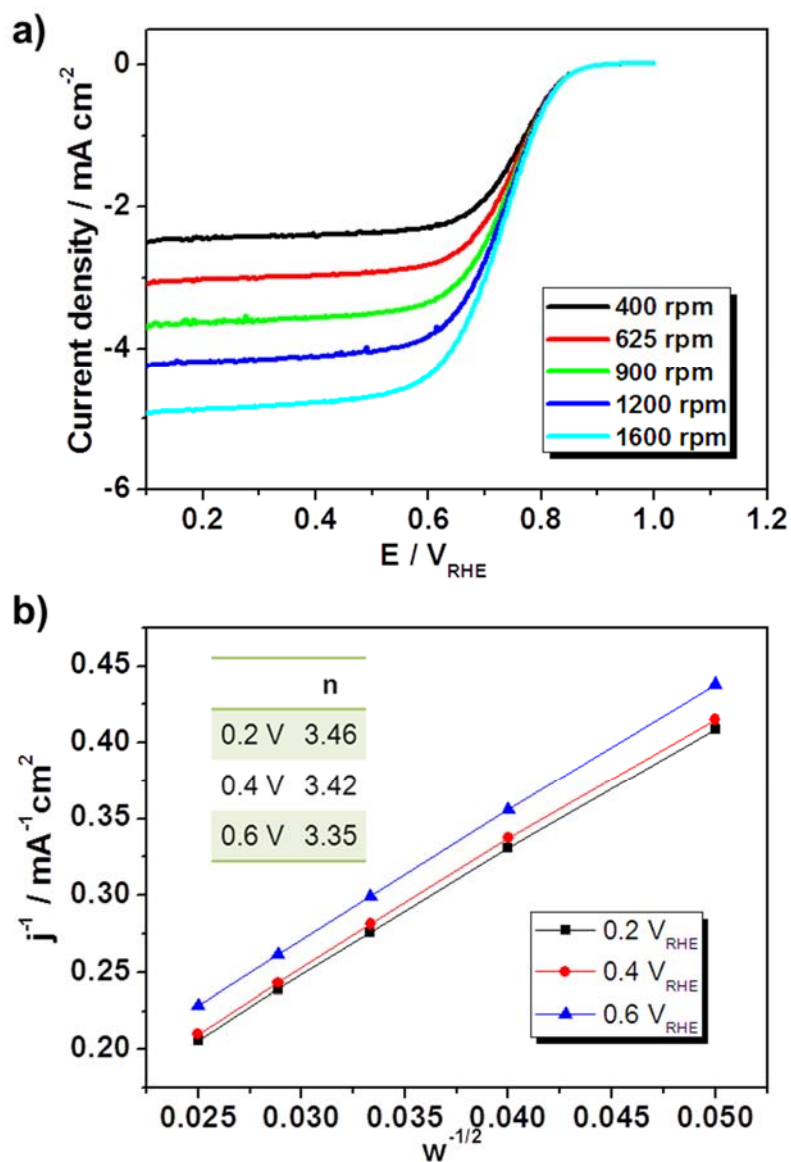


Figure 3.11 Koutecky–Levich plots of g-CN-CNF-700. a) LSVs obtained at various speeds of g-CN-CNF-700 from 400 rpm to 1600 rpm. b) The Koutecky-Levich plots of g-CN-CNF-700 were acquired at a current of 0.2, 0.4, and 0.6 V.

linearity with various rotation speeds. Usually, the number of electrons transferred per O₂ molecule (n) for ORR and kinetic current density can be obtained from the slope and intercept of Koutecky-Levich plots. The electron transfer numbers (n) of g-CN-CNF-700 were 3.46, 3.42, and 3.35 at 0.2, 0.3, and 0.4V, respectively. This means that the ORR catalyzed by g-CN-CNF-700 was nearly dominated by the 4e⁻ pathway.

The electrocatalytic activity of g-CN-CNF-700 was also evaluated using a rotating disk electrode (RDE) under half-cell conditions in acidic solution (Fig. 3.10b), which indicated that its activity was very weak. However, the results obtained in an H₂/O₂ acid PEMFC test were fairly good, despite the poor behavior of the catalyst in acidic solution. This point will be discussed later.

Notably, in a single cell (the practical unit of fuel cells), the pH value is not constantly fixed at 1 or 14 as it is under half-cell conditions. Indeed, the neutral water supplied continuously from the fully humidified inlet gas forms/disappears at the catalyst interface during cell operation, especially during flooding. The pH at the catalyst interface, where the ORR reaction actually occurs, is less than 12 for alkaline fuel cells and greater than 1 for acidic fuel cells. Therefore, we assume that the activity of electrocatalysts in the half-cell is not always necessarily proportional to the performance of the

single cell. The single-cell performance is discussed further in the next section.

An accelerated durability test (ADT) was conducted on the basis of the US Department of Energy (DOE) protocol (Fig. 3.12), and no activity loss was observed. Such excellent stability is an interesting feature of N-doped carbon-based catalysts.¹¹⁻¹⁴ Another important concern for cathode materials in PEMFCs is their tolerance toward methanol. A high catalytic selectivity for the studied cathode reactions against methanol oxidation is shown Fig. 5c. The ORR currents of g-CN-CNF-700 remained constant, irrespective of the presence of methanol. These data indicate that g-CN-CNF materials can serve as alternative electrocatalysts for cathodes in direct methanol fuel cells (DMFCs). The transition metal Fe was added into g-CN-CNFs before the last condensation step to evaluate the effect of metal dopants on the ORR activity. The amount of Fe precursor (FeCl_3) was adjusted to 1.8 wt% and 3.6 wt% relative to g-CN. The metal content in non-PGM catalysts is well known to play an important role in catalyst activity and stability.^{2,24} Contrary to this expectation, the results obtained for g-CN-CNF-700 with and without Fe indicate similar activities toward the ORR, regardless of the amount of Fe added (Fig. 3.10d). Several groups have reported that the transition metal itself does not function as an active site for ORR, but rather facilitates the

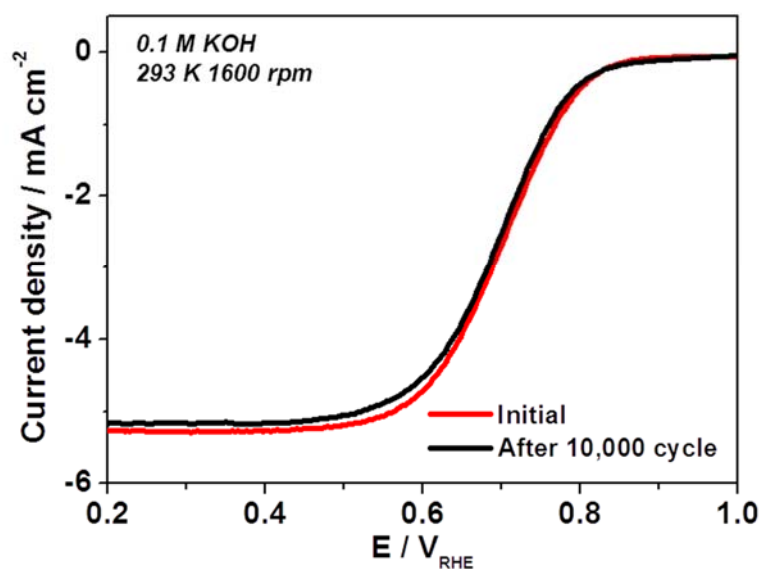


Figure 3.12 Long-term stability test of g-CN-CNF-700. The accelerated durability test (ADT) was conducted based on the DOE protocol from 0.6V to 1.0 V (RHE) under Ar with a scan rate of 20 mVs⁻¹. After completion of initial LSV measurement and continuous potential cycling ~10,000 times; then the final LSV was measured again.

incorporation of N-containing functionalities into graphitic carbon at high temperatures.¹¹ In contrast, in a g-CN structure, where the N-containing graphitic carbons already exist inside a carbon matrix prior to pyrolysis, the metal is not required. Therefore, we concluded that the addition of Fe dopants does not affect the electrocatalytic activity of g-CN-CNF. These results are comparable to those reported by other groups. For example, Silva *et al.* reported that the strongest activity was obtained when the catalyst contained no metal dopants.²⁵ However, a direct comparison of these results is not possible because of differences between the main objectives and experimental conditions of the two studies.

The proposed basic explanation of the ORR mechanism is that the interaction of oxygen with the surface of the catalyst involves the d-band orbital energy of the metal atoms at the surface.¹² Because of the absence of d-bands in the atomic valence orbitals of metal-free catalysts, the tailoring of the electrode surface is thought to be critical. Toward this end, XPS was carried out (Fig. 3.13) to investigate the surface of the N-doped structure in greater detail. The N 1s peak positions are similar to those reported in previous studies.¹¹⁻¹⁴ The total N content and N composition ratio determined from the XPS spectra are summarized in Table 3.1. When combined with the data from the ORR activity (Fig. 10a) and XPS measurements, the results

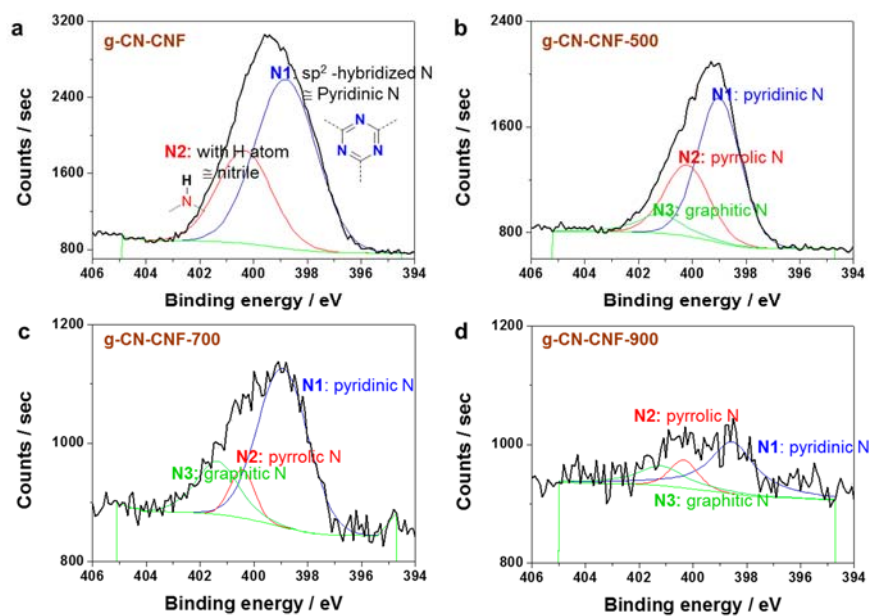


Figure 3.13 XPS spectra of N1s of g-CN-CNF materials. a) g-CN-CNF, b) g-CN-CNF-500, c) g-CN-CNF-700, and d) g-CN-CNF-900.

Table 3.1 Nitrogen properties, binding energy, atomic ratio and N content of g-CN materials

| Material | | Property | | | N content ^b (wt%) |
|--------------|------------------------|----------|--------|--------|---------------------------------|
| | | N1 | N2 | N3 | |
| g-CN-CNF | Binding energy (eV) | 398.80 | 400.34 | - | 26.34 |
| | Ratio (%) ^a | 66.7 | 33.2 | - | |
| g-CN-CNF-500 | Binding energy (eV) | 399.00 | 400.20 | 401.19 | 10.31 |
| | Ratio (%) | 59.8 | 30.9 | 9.4 | |
| g-CN-CNF-700 | Binding energy (eV) | 398.93 | 400.44 | 401.36 | 1.91 |
| | Ratio (%) | 69.3 | 10.3 | 20.4 | |
| g-CN-CNF-900 | Binding energy (eV) | 398.54 | 400.34 | 401.17 | 0.81 |
| | Ratio (%) | 61.6 | 15.2 | 23.3 | |

^aCalculated using Avantage software.

^bFrom EA (Elemental Analyzer) result.

can be summarized as follows. First, the N content and ORR activity do not exhibit a linear relationship. The g-CN-CNF and g-CN-CNF-500 samples exhibited higher N contents compared to the other samples, although the best performance was exhibited by g-CN-CNF-700. Both Lai *et al.* and Biddinger *et al.* have also reported that the total nitrogen content does not play a critical role in determining the ORR activity.⁸ Second, on the basis of the primary difference between the ORR polarization curves of the g-CN-CNF and g-CN-CNF-500/700/900 samples, graphitic N was inferred to facilitate a $4e^-$ pathway. The only g-CN-CNF with pure pyridinic N did not undergo pyrolysis and did not possess a graphitic N moiety. Therefore, the most reasonable interpretation is that pyridinic N only follows a $2e^-$ reduction mechanism for the ORR, consistent with the results of Luo's investigation on pure pyridinic N-doped graphene.¹⁰

Our findings are also similar to those reported by Silva *et al.*, who reported that greater proportions of quaternary (graphitic) N centers favor a $4e^-$ process in the ORR.²⁵ Third; the g-CN-CNF-700 appeared to exhibit excellent electrocatalytic activity because it contained the highest proportion of pyridinic N. However, given the N proportion and pyridinic N content, g-CN-CNF-700 does not contain the largest amount of pyridinic N species. As a consequence, the question of whether the most efficient active sites are

those of pyridinic N or graphitic N remains unanswered.

Single-cell performance of a g-CN-CNF-based MEA

The performance of the single cell using an MEA with g-CN-CNF-700 as the cathode catalyst is shown in Fig. 3.14. Both PEMFCs and AEMFCs were tested. In the case of the PEMFC, all of the polarization curves were obtained under DOE standard conditions (Fig. 3.14a). The current density at 0.6 V was 649 mA cm^{-2} , which was 69% of that of an MEA fabricated using commercial Pt/C. More importantly, the maximum power density was 464 mW cm^{-2} , which is the highest performance reported to date for a metal-free cathode catalyst in a practical device such as an MEA in a PEMFC. For example, Ding *et al.* reported a planar, N-rich, metal-free catalyst with a maximum power density of 320 mW cm^{-2} .⁶ The g-CN-CNF-700-based MEA employed in this study exhibited better single-cell performance. To the best of our knowledge, such a high power density has not been previously reported for a metal-free catalyst. Given the rapid voltage drop in the high-current-density region, the g-CN-CNF-700-based MEAs appeared to suffer from gas transport loss because of the much thicker electrode (50–60 μm) used compared to that containing commercial Pt/C (5–10 μm) (Figs. 3.4 and 3.5). Therefore, further study was necessary to optimize the electrode

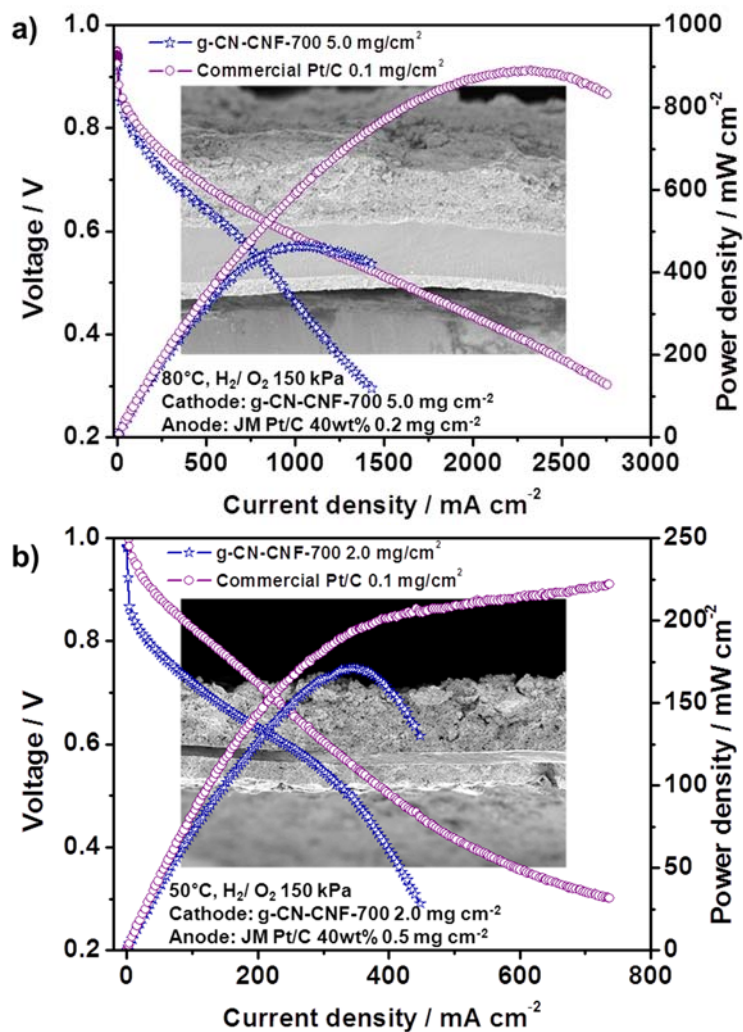


Figure 3.14 Polarization curves of g-CN-CNF-700-based MEAs. a) Acidic fuel cell (PEMFC) with a cathode g-CN-CNF-700 catalyst loading of 5.0 mg cm⁻² operated at 80 °C; b) alkaline fuel cell (AFC) with a g-CN-CNF-700 catalyst loading of 2.0 mg cm⁻² operated at 50 °C. The H₂/O₂ in the MEAs were fully humidified and supplied at a total outlet pressure of 150 kPa. Figures in the background are cross-sectional FE-SEM images of the g-CN-CNF-based MEAs.

structure to facilitate O₂ transfer in the catalyst layer.^{28,29} Additional analyses such as *in situ* electrochemical impedance spectroscopy (EIS) were conducted to evaluate the characteristics of the cell performance (Fig. 3.15). In general, the charge transfer resistance is primarily determined by the interfacial reaction kinetics, ionic conductivity, and diffusion limitations within the catalyst layer. The charge transfer resistance of g-CN-CNF-700 was larger than that of commercial Pt/C, and the former appeared to undergo severe mass transfer loss, probably because of its much thicker electrode. Additionally, the performance of an AEMFC fabricated using the synthesized catalysts was also studied (Fig. 14b). The current density at 0.6 V was 248 mA cm⁻², and the maximum power density was 171 mW cm⁻². The performance characteristics of the g-CN-CNF-700-based PEMFC and AEMFC are summarized in Table 3.2. Whereas the performance of the AEMFC appeared to be inferior to that of the PEMFC, the current density of the AEMFC at 0.6 V was 80.5% of that of commercial Pt/C—greater than that of the PEMFC (69%). Some challenges remain for the AEMFC, all of which are related to the relatively low ionic conductivities, insufficient stabilities, fuel crossover, carbonation, and water management of the PEMs.³⁰ In addition, numerous problems regarding the optimization of the MEA fabrication process and fuel cell operating conditions still need to be

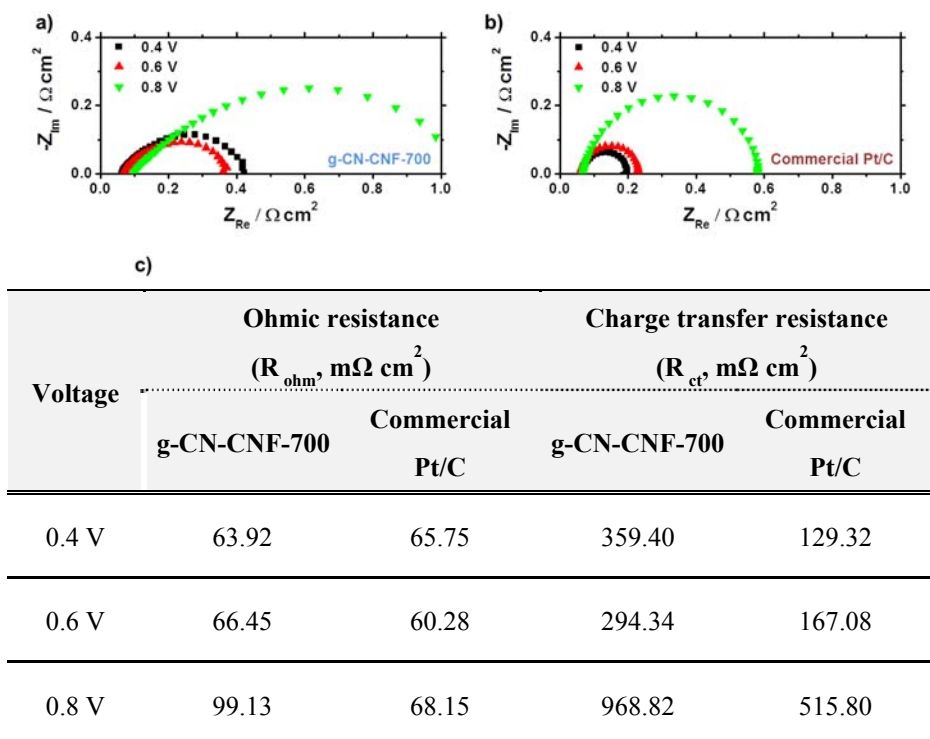


Figure 3.15 *In-situ* EIS of g-CN-CNF-700 and commercial Pt/C. (a) the g-CN-CNF-700-based MEA and b) commercial Pt/C-based MEA at 0.4 V (black square ■), 0.6 V (red triangle ▲), and 0.8 V (green triangle ▼) under operating conditions of 100% relative humidity at 80 °C in PEMFCs, c) the ohmic and charge transfer resistances of the cell using a g-CN-CNF-700 electrode and commercial Pt/C MEA from EIS.

Table 3.2 Performance characteristics of g-CN-CNF-700-based PEMFCs and AEMFCs.

| | | Current density at 0.6 V (mA cm ⁻²) | Max. power density (mW cm ⁻²) |
|--------------|------------|--|--|
| PEMFC | Commercial | 941 | 890 |
| | Pt/C | (100 %) | (100 %) |
| | g-CN-CNF- | 649 | 464 |
| | 700 | (69.0 %) | (52.1 %) |
| AEMFC | Commercial | 308 | 222 |
| | Pt/C | (100 %) | (100 %) |
| | g-CN-CNF- | 248 | 171 |
| | 700 | (80.5 %) | (77.0 %) |

resolved. If these challenges are overcome, a comparable result may be anticipated for PEMFCs.

3.5 Conclusion

We have demonstrated an approach for the facile and gram-scale production of g-CN materials and demonstrated the excellent performance of the g-CN-CNF-700-based MEA in a single cell of both a PEMFC and an AEMFC. The g-CN was synthesized by a liquid-based poly-condensation reaction, and a completely metal-free cathode material was obtained by pyrolysis. This newly synthesized material exhibited remarkable methanol tolerance, selectivity, and stability without the inclusion of a metal dopant. The graphitic N moiety appears to be responsible for the $4e^-$ process in the ORR. More importantly, the results of this study demonstrate for the first time that a completely metal-free fuel cell cathode can be used in a practical device, both in a PEMFC and an AEMFC, making it a potential candidate for the replacement of Pt-metal-based catalysts. Even better performance is expected to be achieved through optimization of the electrode structure to expedite mass transfer. The fabrication method and remarkable performance of the single cell in this study represent progressive steps toward realistic applications of metal-free materials in commercialized fuel cells.

3.6 References

1. Su, D. S. and Sun, G. Nonprecious-metal catalysts for low-cost fuel cells, *Angew. Chem. Int. Ed.* **50**, 11570–11572 (2011).
2. Jaouen, F. *et al.* Recent advances in non-precious metal catalysis for oxygen-reduction reaction in polymer electrolyte fuel cells, *Energy Environ. Sci.* **4**, 114–130 (2011).
3. Chen, Z., Higgins, D., Yu, A., Zhang, L. and Zhang, J. A review on non-precious metal electrocatalysts for PEM fuel cells, *Energy Environ. Sci.* **4**, 3167–3192 (2011).
4. Lai, L. Exploration of the active center structure of nitrogen-doped graphene-based catalysts for oxygen reduction reaction, *Energy Environ. Sci.* **5**, 7936–7942 (2012).
5. Sharifi, T., Hu, G., Jia, X. and Wågberg, T. Formation of active sites for oxygen reduction reactions by transformation of nitrogen functionalities in nitrogen-doped carbon nanotubes, *ACS nano* **6**, 8904–8912 (2012).
6. Ding, W. *et al.* Space-confinement-induced synthesis of pyridinic- and pyrrolic-nitrogen-doped graphene for the catalysis of oxygen reduction, *Angew. Chem. Int. Ed.* **52**, 11755–11759 (2013); *Angew.*

- Chem.* **125**, 11971–11975 (2013).
7. Biddinger, E. J. and Ozkan, U. S. Role of graphitic edge plane exposure in carbon nanostructure for oxygen reduction reaction, *J. Phys. Chem. C* **114**, 15306–15314 (2010).
 8. Zheng, Y., Jiao, Y., Jaroniec, M., Jin, Y. and Qiao, S. Z. Nanostructured metal-free electrochemical catalysis for highly efficient oxygen reduction, *Small* **8**, 3550–3566 (2012).
 9. Wong, W. Y. *et al.* Pyridinic N doped graphene: synthesis, electronic structure, and electrocatalytic property, *Int. J. Hydrogen Energy* **38**, 9370–9386 (2013).
 10. Luo, Z., *et al.* Recent progress in nitrogen-doped carbon and its composites as electrocatalysts for fuel cell applications, *J. Mater. Chem.* **21**, 8038 (2011).
 11. Zheng, Y., Liu, J., Liang, J., Jaroniec, M. and Qiao, S. Z. Graphitic carbon nitride materials: controllable synthesis and applications in fuel cells and photocatalysis, *Energy Environ. Sci.* **5**, 6717–6731 (2012).
 12. Wang, Y., Wang, X. and Antonietti, M. Polymeric graphitic carbon nitride as a heterogeneous organocatalyst: from photochemistry to multipurpose catalysis to sustainable chemistry, *Angew. Chem. Int.*

- Ed.* **51**, 68–89 (2012); *Angew. Chem.* **124**, 70–92 (2012).
13. Liang, J. *et al.* Facile oxygen reduction on a three-dimensionally ordered macroporous graphitic C₃N₄/carbon composite electrocatalyst, *Angew. Chem. Int. Ed.* **51**, 3892–3896 (2012); *Angew. Chem.* **124**, 3958–3962 (2012).
 14. Xu, J. *et al.* A new and environmentally benign precursor for the synthesis of mesoporous g-C₃N₄ with tunable surface area, *Phys.Chem. Chem. Phys.* **15**, 4510–4517 (2013).
 15. Sheng, Z.-H. *et al.* Catalyst-free synthesis of nitrogen-doped graphene via thermal annealing graphite oxide with melamine and its excellent electrocatalysis, *ACS nano* **5**, 4350–4358 (2011).
 16. Lee, J.-S., Park, G. S., Kim, S. T., Liu, M. and Cho, J. A highly efficient electrocatalyst for the oxygen reduction reaction: N-doped Ketjenblack incorporated into Fe/Fe₃C-functionalized melamine foam, *Angew. Chem. Int. Ed.* **125**, 1060–1064 (2013); *Angew. Chem.* **125**, 1060–1064 (2013).
 17. Yang, S. J., Cho, J. H., Oh, G. H., Nahm, K. S. and Park, C. R., Easy synthesis of highly nitrogen-enriched graphitic carbon with a high hydrogen storage capacity at room temperature, *Carbon* **47**, 1585–1591 (2009).

18. Steffensen, M. B. and Simanek, E. E. Chemoselective building blocks for dendrimers from relative reactivity data, *Org. Lett.* **13**, 2359–2361 (2003).
19. Zhang, W., Nowlan, D. T., Thomson, L. M., Lackowski, W. M. and Simanek, E. E. Orthogonal, convergent syntheses of dendrimers based on melamine with one or two unique surface sites for manipulation, *J. Am. Chem. Soc.* **123**, 8914–8922 (2001).
20. Park, H.-S. *et al.* Performance enhancement of PEMFC through temperature control in catalyst layer fabrication, *Electrochimica Acta* **53**, 763–767 (2007).
21. Wirnhier, E. *et al.* Poly(triazine imide) with intercalation of lithium and chloride ions $[(C_3N_3)_2(NH_xLi_{1-x})_3.LiCl]$: A crystalline 2D carbon nitride network, *Chem. Eur. J.* **17**, 3213–3222 (2011).
22. Jürgens, B. *et al.* Melem (2,5,8-triamino-tri-s-triazine), an important intermediate during condensation of melamine rings to graphitic carbon nitride: synthesis, structure determination by x-ray powder diffractometry, solid-state NMR, and theoretical studies, *J. Am. Chem. Soc.* 2003, 125, 10288–10300 (2003).
23. Holst, J. R. and Gillan, E. G. From triazines to heptazines: deciphering the local structure of amorphous nitrogen-rich carbon

- nitride materials, *J. Am. Chem. Soc.* **130**, 7373–7379 (2008).
24. Bezerra, C.W.B. *et al.* A review of Fe–N/C and Co–N/C catalysts for the oxygen reduction reaction, *Electrochimica Acta* **53**, 4937–4951 (2008).
25. Silva, R., Voiry, D., Chhowalla, M. and Asefa, T. Efficient metal-free electrocatalysts for oxygen reduction: polyaniline-derived N- and O-doped mesoporous carbons, *J. Am. Chem. Soc.* **135**, 7823–7826 (2013).
26. Nallathambi, V., Lee, J. W., Kumaraguru, S. P., Wu, G. and Popov, B. N. Development of high performance carbon composite catalyst for oxygen reduction reaction in PEM Proton Exchange Membrane fuel cells, *J. Power Sources* **183**, 34–42 (2008).
27. Yoo, S. J. *et al.* Promotional effect of palladium on the hydrogen oxidation reaction at a PtPd alloy electrode, *Angew. Chem. Int. Ed.* **47**, 9307–9310 (2008); *Angew. Chem.* **120**, 9447–9450 (2008).
28. Proietti, E. *et al.* Iron-based cathode catalyst with enhanced power density in polymer electrolyte membrane fuel cells, *Nat. Commun.* **2**, 416 (2011).
29. Kim, O.-H. *et al.* Ordered macroporous platinum electrode and enhanced mass transfer in fuel cells using inverse opal structure,

- Nat. Commun.* **4**, 2473. (2013).
30. Wang, Y.-J., Qiao, J., Baker, R. and Zhang, J. Alkaline polymer electrolyte membranes for fuel cell applications, *Chem. Soc. Rev.* **42**, 5768–5787 (2013).

국문초록

연료전지는 효율이 높고 오염이 없거나 적으므로 현재의 화석연료 의존성을 줄일 차세대 대체 에너지원으로서 중요한 위치에 있다. 이러한 연료전지 중에서 고분자 전해질 연료전지(PEMFC)는 높은 효율과 낮은 작동온도, 빠른 시동과 신속한 응답특성 등의 특징으로 인해 집중적으로 연구되어 왔으며, 가장 상용화에 근접한 것으로 알려져 있다. 또한 고분자 전해질 연료전지는 잠수함과 같이 은밀함이 요구되는 수중 추진체의 동력원으로 가장 효과적인 해결책으로 여겨지고 있다. 그러나 고분자 전해질 연료전지는 구성품의 가격이 비싸며 안정성이 부족하여 아직까지 완전히 상용화되지는 못하였다. 특히, 매장량이 적고 가격이 비싼 귀금속인 백금(Pt)을 촉매로 사용하는 것은 중요한 한계점으로 지적되고 있다. 따라서 고분자 전해질 연료전지의 핵심 요소인 막-전극 접합체(MEA)의 구조를 바꾸고 새롭게 디자인하여서 보다 효과적인 전극 구조를 제작하고, 이러한 전극을 기반으로 기존보다 뛰어난 성능을 구현하는 연구가 많은 관심을 끌고 있다. 그리고 기존의 백금 기반 촉매를 더욱 저렴하고 매장량이 풍부한 원소를 이용한 물질로 대체하는 연구 또한 다양하게 시도되고 있다.

본 연구에서는 1) 3차원으로 규칙적으로 정렬된 마이크로 기공을

갖는 촉매 구조를 도입하고, 2) 새로운 비금속 촉매를 합성하여 산성 및 알칼라인 고분자 전해질 모두에 적용하여 고분자 전해질 연료전지의 막-전극 접합체와 촉매 구조를 변화하여 실제 연료전지 장치에서 더욱 뛰어난 성능을 구현하였다. 앞서 언급한 것처럼 막-전극 접합체의 새로운 디자인에 대한 연구는 시급한 상황이나, 충분히 시도되지 않았으며 보다 구체적인 접근이 필요하다. 지금까지 촉매 층의 새로운 디자인 연구는 실제 연료전지의 최하 단위인 단전지(single-cell)에 기반하지 않고 주로 반전지(half-cell) 적용에 국한되었으며, 실제 디바이스 적용에의 잠재적 가능성만을 제시하는데 그쳤다. 그러나 본 연구에서는 막-전극 접합체의 전극 구조를 새롭게 하는 시도를 하면서 실제적인 장치인 단전지의 MEA에 적용하여 성능을 구현하였다.

1장에서는 연료전지의 기본 원리와 종류, 역사 및 주요 현안에 대해 언급하였다. 또한 잠수함과 같은 수중 추진체의 정숙한 에너지원으로 고분자 전해질 연료전지를 적용하기 위한 시도에 대해서도 간략히 알아보았다.

2장에서는 대면적의 규칙적인 마이크로 기공 구조를 갖는 백금 전극에 대해 소개하고, 이를 고분자 전해질 연료전지의 막-전극 접합체에 실제로 적용하였다. 이러한 인버스 오팔구조의 전극은 같은 양의 백금이 사용된 기존의 촉매잉크 슬러리 기반 전극에

비해 85% 뛰어난 성능을 보였다. 이처럼 3차원으로 정렬된 마이크로 기공 구조 전극물질은 그 규칙적인 구조에 기인한 다양한 장점들이 있다. 즉, 물질전달이 용이하며, 표면적 증대 및 개방된 구조를 가지면서 서로 연결된 기공으로 인해 반응물/생성물의 유입 및 배출이 전달이 빠르며, 반응이 실제로 일어나는 3상 계면의 증가가 가능하다. 뿐만 아니라 이 연구는 연료전지 전극에 국한되지 않고 다양한 전기 디바이스에 적용이 가능한 잠재성을 가지고 있으므로 다양한 연구에 기초 정보를 제공할 것이다.

3장에서는 간단하고 대량생산이 가능한 방법을 사용하여 흑연질 탄소 질화물을 합성하여 산성 고분자 전해질 (H^+ 전도) 및 알칼라인 고분자 전해질 (OH^- 전도) 연료전지에 적용하였다. 합성된 비금속 촉매를 사용하여 연료전지 공기극(cathode)의 막-전극 접합체를 제작하였으며 이를 산성 및 알칼라인 연료전지에 사용하여 실제 구동한 결과, 기존의 백금 기반 상용촉매와 비교하여 각각 69% 와 80% 성능을 달성하였다. 연료전지 공기극의 산소 환원반응을 위한 비귀금속 촉매에 대해서는 비록 이미 많은 연구가 진행되었지만, 소수의 그룹에서만 실제 연료전지에 적용한 결과를 보고하였으며, 그 성능은 본 연구 결과에 비해 낮다. 따라서 본 장에서 제시된 단전지 제작 방법과 주목할 만한 성능은 현재 연구단계에 머물러 있는 비금속 촉매를 실질적인 상용 연료전지에 적용할 수 있다는

가능성을 보여준다.

핵심어: 고분자 전해질 연료전지 · 막-전극 접합체 · 계층 구조 ·

비금속 촉매

학 번: 2011-30793

List of Publications (SCI)

1st or co-1st author

1. Ok-Hee Kim, Shin-Woo Ha, Jae Il Kim and Jin-Kyu Lee, Excellent photostability of phosphorescent nanoparticles and their application as a color converter in light emitting diodes, *ACS Nano* **4**, 3397 (2010).
2. Ok-Hee Kim, Yong-Hun Cho, Soon Hyung Kang, Hee-Young Park, Minhyoung Kim, Ju Wan Lim, Dong Young Chung, Myeong Jae Lee, Heeman Choe and Yung-Eun Sung, Ordered macroporous platinum electrode and enhanced mass transfer in fuel cells using inverse opal structure, *Nat. Commun.* **4**, 2473 (2013).
3. Hyelim Choi, Ok-Hee Kim, Minhyoung Kim, Heeman Choe, Yong-Hun Cho and Yung-Eun Sung, Next-generation polymer-electrolyte-membrane fuel cells using titanium foam as gas diffusion layer, *ACS Appl. Mater. Interfaces* **6**, 7665 (2014).
4. Yoon-Hwan Cho, Ok-Hee Kim, Dong Young Chung, Heeman Choe, Yong-Hun Cho and Yung-Eun Sung, PtPdCo ternary electrocatalyst

for methanol tolerant oxygen reduction reaction in direct methanol fuel cell, *Appl. Catal. B. Environ.* **154**, 309 (2014).

5. Sun Ha Park, Ok-Hee Kim, Jin Soo Kang, Kyung Jae Lee, Jung-Woo Choi, Yong-Hun Cho and Yung-Eun Sung, Poly(3,4-ethylenedioxy thiophene) inverse opal electrode fabricated from poly(3,4-ethylenedioxythiophene): poly(styrenesulfonate)-filled polystyrene template for dye-sensitized solar cells, *Electrochim. Acta* **137**, 661 (2014).
6. Ok-Hee Kim, Yong-Hun Cho, Dong Young Chung, Minjeong Kim, Ji Mun Yoo, Ji Eun Park, Heeman Choe and Yung-Eun Sung, Realistic applications of metal-free materials as fuel cells electrodes: both acidic and alkaline polymer electrolytes, *Sci. Rep.*, in revision.

Co-author

1. Yong-Hun Cho, Ju Wan Lim, Yun Sik Kang, Yoon-Hwan Cho, Ok-Hee Kim, Nak-Hyun Kwon, Oh Joong Kwon, Won-Sub Yoon, Heeman Cho and Yung-Eun Sung, The dependence of performance degradation of electrode assembly on platinum loading in polymer electrolyte membrane fuel cell, *Int. J. Hydrog. Energy* **37**, 2490–

2497 (2012)

2. Ju Wan Lim, Yong-Hun Cho, Minjeh Ahn, Dong Young Chung, Yoon-Hwan Cho, Namgee Jung, Yun Sik Kang, Ok-Hee Kim, Myeong Jae Lee, Minhyoung Kim and Yung-Eun Sung, Ionic resistance of a cathode catalyst layer with various thicknesses by electrochemical impedance spectroscopy for PEMFC, *J. Electrochem. Soc.* **159**, B378–B384 (2012)
3. Yong-Hun Cho, Tae-Yeol Jeon, Sung Jong Yoo, Kug-Seung Lee, Minjeh Ahn, Ok-Hee Kim, Yoon-Hwan Cho, Ju Wan Lim, Namgee Jung, Won-Sub Yoon, Heeman Choe and Yung-Eun Sung, Stability characteristics of Pt₁Ni₁/C as cathode catalysts in membrane electrode assembly of polymer electrolyte membrane fuel cell, *Electrochim. Acta* **59**, 264–269 (2012)
4. Yoon-Hwan Cho, Jin Woo Bae, Ok-Hee Kim, Jae Young Jho, Namgee Jung, Kyu soon Shin, Hyelim Choi, Heeman Choe, Yong-Hun Cho and Yung-Eun Sung, High performance direct methanol fuel cells with micro/nano-patterned polymer electrolyte membrane, *J. Memb. Sci.* **467**, 36–40 (2014).